SLAC-R-793

Measurement of Lambda(C) Branching Fractions of Cabibbo-Suppressed Decay Modes in the BABAR Experiment

Mohammad Saleem

Stanford Linear Accelerator Center
Stanford University
Stanford, CA 94309

SLAC-Report-793

Prepared for the Department of Energy
under contract number DE-AC02-76SF00515

Printed in the United States of America. Available from the National Technical Information Service, U.S. Department of Commerce, 5285 Port Royal Road, Springfield, VA 22161.

Measurement of Λ_c Branching Fractions of Cabibbo-Suppressed Decay Modes in the *BABAR* Experiment

by

M. Saleem

A Dissertation

Submitted to the University at Albany, State University of New York

in Partial Fulfillment of

the Requirements for the Degree of

Doctor of Philosophy

College of Arts & Sciences

Department of Physics

2005

Measurement of Λ_c Branching Fractions of Cabibbo-Suppressed Decay Modes in the *BABAR* Experiment

M. Saleem, Ph.D.

Advisor: Professor M. Sajjad Alam

The University at Albany, State University of New York, 2005

This dissertation reports on a study of the relative branching fraction measurement of the charmed baryon Λ_c decaying to the Cabibbo-suppressed modes.

A data sample of 125 fb^{-1} is used for these measurements. This data samples was collected with the *BABAR* detector at the $\Upsilon(4S)$ resonance and ~ 40 MeV below the resonance. The branching fractions measurement of the Cabibbo-suppressed decays $\Lambda_c^+ \to \Lambda^0 \ K^+$ and $\Lambda_c^+ \to \Sigma^0 \ K^+$ relative to that of Cabibbo-favored modes $\Lambda_c^+ \to \Lambda^0 \ \pi^+$ and $\Lambda_c^+ \to \Sigma^0 \ \pi^+$ to be $0.044 \ \pm \ 0.004$ (stat.) $\pm \ 0.003$ (syst.) and $0.038 \ \pm \ 0.005$ (stat.) $\pm \ 0.003$ (syst.), respectively, are presented. This analysis also set an upper limit on the branching fraction at 90% confidence level for $\Lambda_c^+ \to \Lambda^0 \ K^+\pi^+\pi^-$ to be $< 4.8 \times \ 10^{-2}$ relative to that of $\Lambda_c^+ \to \Lambda^0 \ \pi^+$. The upper limit of the branching fraction into the decay $\Lambda_c^+ \to \Sigma^0 \ K^+\pi^+\pi^-$ relative to that of $\Lambda_c^+ \to \Sigma^0 \ \pi^+$ has been measured to be $< 2.0 \times \ 10^{-2}$ at the 90% confidence level. We also measure the relative branching fraction for the Cabibbo-favored modes $\Lambda_c^+ \to \Sigma^0 \ \pi^+$, $\Lambda_c^+ \to \Xi^- \ K^+ \ \pi^+$ and $\Lambda_c^+ \to \Lambda^0 \ K_S^0 \ K^+$ relative to that of $\Lambda_c^+ \to \Lambda^0\pi^+$ to be: $0.977 \ \pm \ 0.015$ (stat.) $\pm \ 0.051$ (syst.), $0.481 \ \pm \ 0.016$ (stat.) $\pm \ 0.038$ (syst.) and $0.397 \ \pm \ 0.026$ (stat.) $\pm \ 0.036$ (syst.), respectively. Comparison to previous

experiments and also to the theoretical predictions (wherever needed) are also given.

To my father and (late)mother

Acknowledgments

As with any major endeavour, this thesis was not created in vauum but rather in a fertile academic enviornment with the assistance of many people. I cannot hope to mention every person who has played a part but some individuals are worthy of specific mention.

First of all, I would like to thank all *BABAR* collaborators, without whom this work would not have been possible. The PEP-II staff deserve recognition for the excellent performance of the accelerator and for their hard work in developing one of the highest luminosity e^+e^- collider in the world.

My advisor, Professor M. Sajjad Alam, has been very helpful and encouraging during my time at The University of Albany, State University of New York, and so have my fellow grad students and postdocs Dr. Steve Timm and Dr. Frank wappler here at Albany.

I am highly indebted to Dr. Prafulla K. Behera of University of Pennsylvania, who took upon himself "to show me the ropes". I learned a great deal from him and had a lot of fun working with him. Prafulla deserves a great appreciation and high respect for his patient instructions and kind guidance through out my stay at SLAC from starting of my analysis towards the completion of this thesis and the paper. I am very thankful to Prafulla for being there whenever I was looking for help.

Whilst serving as Data Quality Manager for the *BABAR* collaboration I had the opportunity to work with wide range of collaboration members. I would like thank to my wonderful colleagues at IR2 during this times, in particular to the OEP group members who were always around to help and were great pleasure to work with.

I also have to thank my paper committee, Georges Vesures, Gerry Lynch, Brain

T. Meadows, and David C. Williams. Many thanks to Prafulla and David Williams for making my paper look better. Thanks to the Charm AWG for their help in finishing and polishing my analysis especially to Bill Dunwoodie for his helpful suggestions and help. I would like to thank my thesis committee, Prof. Sajjad Alam, Prof. Brain T. Meadows, Prof. Ariel Caticha, Prof. Jesse Ernst and Dr. Prafulla K. Behera. Special thanks to Prafulla for helping me in writing a better CV.

And finally, I owe a great deal of gratitude to my father, my sisters Rehana, Rukhsana and my brother Saeed who continually encouraged and supported me. I also owe a special thanks to my wife Ruby, who took care of me at each step and sharing my ups and downs and for her encouragement and patiance during my dissertation.

Contents

List of Figures

List of Tables

Chapter 1

Introduction

1.1 Overview of Fundamental Constituents

The purpose of particle physics is to study the ultimate structure of the universe: the fundamental particles which compose the matter the world is made of, and the fundamental interactions between particles, which makes matter as it does. The best understanding we have today of the laws governing the fundamental particles and interactions is called the Standard Model (SM).

In the Standard Model, all matter is composed of 12 point-like elementary particles, grouped in two families: 6 leptons (e : electron, μ : muon, τ : tau, ν_e : electron neutrino, ν_μ : muon neutrino, and ν_τ : tau neutrino) and 6 quarks (u : up, d : down, s : strange, c : charm, b : bottom, and t : top), as shown in Table 1.1. For each elementary particle there is a corresponding antiparticle, which has opposite-equal quantum numbers. Both leptons and quarks have spin 1/2 and are called *fermions*. The three leptons e, μ, τ have unit (negative) electric charge and are massive, while the three corresponding neutrinos ν_e, ν_μ, ν_τ have zero electric

Table 1.1: Quark and lepton properties

Quarks (spin = $\frac{1}{2}$)			Leptons (spin = $\frac{1}{2}$)		
Flavor	Electric Charge	Mass (GeV/c^2)	Flavor	Electric Charge	Mass (GeV/c^2)
u	$+\frac{2}{3}$	0.004	e	-1	0.0005
d	$-\frac{1}{3}$	0.007	ν_e	0	0
c	$+\frac{2}{3}$	1.3	μ	-1	0.106
s	$-\frac{1}{3}$	0.3	ν_μ	0	0
t	$+\frac{2}{3}$	180	τ	-1	1.777
b	$-\frac{1}{3}$	4.8	ν_τ	0	0

charge and are known to have very tiny mass (or mass less than electron). The six quarks are massive, have fractional electric charge and are further characterized by a *color charge* (whereas leptons do not have a *color charge*). There is no free quark in nature but rather quarks are compelled to combine into more complex structures called *hadrons*, which must be color neutral (known as quark confinement). Hadrons are composed of a quark and an anti-quark ($q\bar{q}$: meson), or of three quarks or three anti-quarks (qqq or $\overline{qqq}$: Baryon), where mesons have integral spin (0,1,...) and baryons have half-integer spin (so they are like fermions).

All known interactions between matter particles can be explained in terms of only four fundamental forces, which in order of increasing strength are the *gravitational force*, the *weak force*, the *electromagnetic force*, and the *strong force*. The gravitational force acts between particles with mass and is responsible for the binding of matter on a cosmic and planetary scale, but because of its small strength it has negligible effect on high energy physics phenomena.

The *weak force* acts upon particles with weak charge (all leptons and quarks) and is responsible for some of the spontaneous decays of particles (e.g., the radioactive nucleus β decay). Since the *weak force* is short lived so all the massive particles created at the birth of the universe have since decayed to less massive particles that compose the world we live in today.

Particles with electric charge (all quarks and the three charged leptons) interact through the *electromagnetic force*, the force which binds the atoms and molecules together. The theory which describe this force is called QED.

Finally, the color force (also known as *strong force*) acts between the particles

Table 1.2: Properties of Fundamental Forces

Force	Strength	Theory	Range	Lifetime (s)	Mediating Particles
Gravity	10^{-42}	Quantum Gravity	infinity	$\sim$	Graviton
Weak	10^{-13}	Weak	$\frac{1}{M_W}$	10^{-12} or longer	W & Z
Electromagnetic	10^{-2}	QED	infinity	$10^{-20} \sim 10^{-16}$	photon(γ)
Strong	0.1	QCD	1 fm	10^{-23}	8 gluons(g)

with color charge (all quarks but not the leptons) and is responsible for the confinement of the quarks inside a hadron (and of course on a larger scale, for binding the hadrons in a nucleus). The color force is known to work under the QCD (Quantum Chromodynamics). Both the *electromagnetic* and *strong force* conserve quark and lepton flavor.

When the two matter particles interact through a fundamental force, the process is described as the exchange of "force particle" called *gauge bosons*, as shown in Tables 1.2, 1.3. The gauge bosons are the trains through which fundamental forces are conveyed between particles. The range of each fundamental force is inversely proportional to the mass of the corresponding gauge boson. For example, the elec-

Table 1.3: Properties of Gauge Bosons (Mediating Particles also known as field quanta)

Gauge Boson	Electric Charge	Mass (GeV/c^2)	Spin	Force Mediated
g	0	0	1	color
γ	0	0	1	e-m
$W^{\pm}$	$\pm$ 1	80.6	1	weak
Z^0	$\pm$ 1	91.2	1	weak

tromagnetic force is mediated by the photon γ, which has zero mass: consequently its range is infinite. The weak force instead is mediated by two very massive bosons, $W^{\pm}$ and the Z^0, and it has very short range. Also the color force has short range, here the corresponding gauge bosons are called gluons (g).

1.2 Physics at PEP-II - e^+e^- Asymmetric Collider

At an asymmetric e^+e^- collider like PEP-II the bunches of high-energy electrons (9.0 GeV) are brought into collision with low-energy positrons (3.1 GeV). This is operating at higher luminosity which is of the order $10^{33}\,\mathrm{cm}^{-2}\mathrm{s}^{-1}$ and the total center-of-mass energy E_{cm}=10.58 GeV/c, mass of the $\Upsilon(4S)$ resonance, in an asymmetric mode i.e., with beams of unequal energy. Since electron and positron energies are not equal, therefore the center-of-mass frame is boosted in the laboratory frame, resulting in B mesons with significant momenta in the laboratory frame (the small Q-value of the $\Upsilon(4S)\rightarrow B\overline{B}$ decay results in B mesons almost at rest in the center-of-mass frame, as was in the CESR - e^+e^- symmetric ring, which was limited to number of B meson pairs due to low luminosity). This enables the B meson's decay time to be inferred from their now-measurable difference of the two decays from the two B's and the high luminosities provide enough B mesons, which is important in order to measure the direct CP violation. Besides the CP violation, there are also other interesting phenomena which can be studied at the high luminosity collider. One of them is the production mechanism of charmed baryons produced from the continuum (almost 40 MeV below the $\Upsilon(4S)$ resonance), which needs to be understood very well.

During the e^+e^- collision, some fraction of the time, an electron and a positron annihilate to produce a virtual photon which then fragments into a pair of fermions. The final state must have the same quantum numbers as those of the photon ($J^{PC} = 1^{--}$). The cross section for this process, in the limit of massless electrons and fermions, is given by:

$$\sigma(e^+e^- \rightarrow f\bar{f}) = \frac{4\pi\alpha^2}{3s} e_f^2, \tag{1.1}$$

where e_f is the charge of the resulting fermion, s denotes the square of the center-of-mass energy, and α is the QED coupling constant. If the fermions turn out to be quarks, then they will hadronize into quark jets and the cross section will require QCD corrections. As we know the quarks have fractional charges therefore the relation between the cross-section $\sigma(e^+e^- \rightarrow q\overline{q})$ and the cross-section $\sigma(e^+e^- \rightarrow \mu^-\mu^+)$ has the following form,

$$\sigma(e^+e^- \rightarrow q\overline{q}) = 3e_q^2 \sigma(e^+e^- \rightarrow \mu^-\mu^+). \tag{1.2}$$

where the factor 3 is for the number of colors for each quark flavor. We must sum over all the quarks in the energy range considered, and the ratio R is defined as,

$$R = \frac{\sigma(e^+e^- \rightarrow q\overline{q})}{\sigma(e^+e^- \rightarrow \mu^-\mu^+)} = 3\sum_q e_q^2. \tag{1.3}$$

The hadronic cross-section at different energies is shown in figure 1.1.

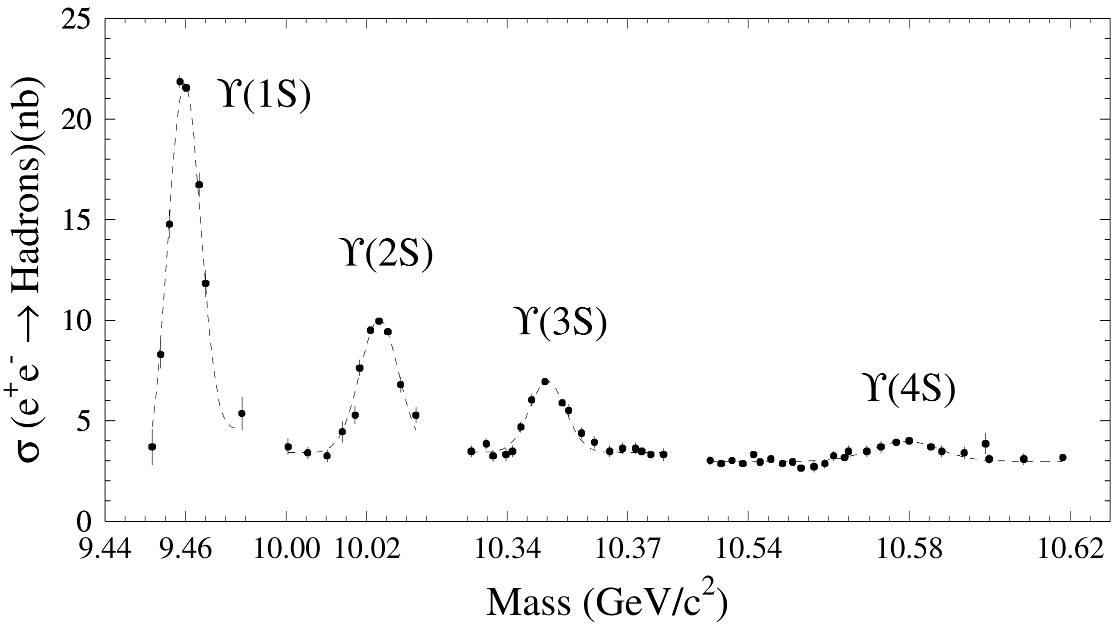

Figure 1.1: The four Υ resonances, as observed at CESR.

1.2.1 $e^+e^-\to B\overline{B}$

If the center-of-mass energy is high enough $b\bar{b}$ pairs can be produced and form bound states, like $\Upsilon(1S)$, $\Upsilon(2S)$, and $\Upsilon(3S)$ resonance. At even higher energies excited $b\bar{b}$ bound states are formed, leading to a family of resonances. The production cross sections for these resonances is shown in Figure 1.1 as a function of energy. The mass of the $\Upsilon(4S)$ (10.58 GeV/c^2) is high enough so that a second pair of light quarks can be produced from the vacuum such that $\Upsilon(4S)$ decays via strong interaction. The $\Upsilon(4S)$ bound state disintegrates and either a $u\bar{u}$ or a $d\bar{d}$ pair is created from the vacuum to form a B and a $\overline{B}$ mesons, each of mass ~ 5.279 GeV/c^2. The availability of this decay channel makes the $\Upsilon(4S)$ significantly broader than the first three Υ resonances, which only have OZI (Okubo-Zweig-Iizuka) suppressed channels available for their decay. Since Υ states have $J^{PC} = 1^{--}$, they can decay via ggg, $gg\gamma$, $\gamma\gamma\gamma$, or γ. Furthermore, each gluon exchange introduces a factor of strong coupling constant, $\sqrt{\alpha_s}$, in the decay amplitude and hence suppresses the annihilation amplitude. The OZI rule [1] states that if in a decay all the energy is transferred via (hard) gluons, then that decay is suppressed, resulting in a narrow width and correspondingly a longer life time. Examples of this suppression can be seen in Figures 1.2 (a) and (b). The electromagnetic annihilation process shown in Figure 1.2 (c) is also suppressed compared to the $\Upsilon(4S) \rightarrow B\overline{B}$ decay mode, but this time because of different relative strengths of the involved interactions. The decay of B mesons can be described by five basic decay diagrams, shown in Figure 1.3: (a) external spectator, (b) internal or color mixed spectator, (c) annihilation, (d) W-exchange, and (e) penguin processes. The external spectator is the simplest process because the light quark does not participate in the weak decay process. One of the final state particles is produced by the W^-, whereas the other one is formed by the c (or u) quark and the light spectator. In the internal spectator (also called color mixed or color suppressed) diagram, the c and the spectator quarks combine with the quarks from the virtual W to form final state particles. It is suppressed because the color of the W-daughter quarks has to match with that of the c and the spectator quark, since the final states have to be colorless. Naively, one would expect this decay to be suppressed by a factor of $1/N_c^2 = 9$, with N_c^2 being the number of colors, but the suppression is mitigated by gluon exchange effects. W-annihilation and W-exchange processes are helicity suppressed, and W-annihilation is also color suppressed. Penguin processes are also heavily suppressed because of additional gluon exchanges between the heavy and the light quark.

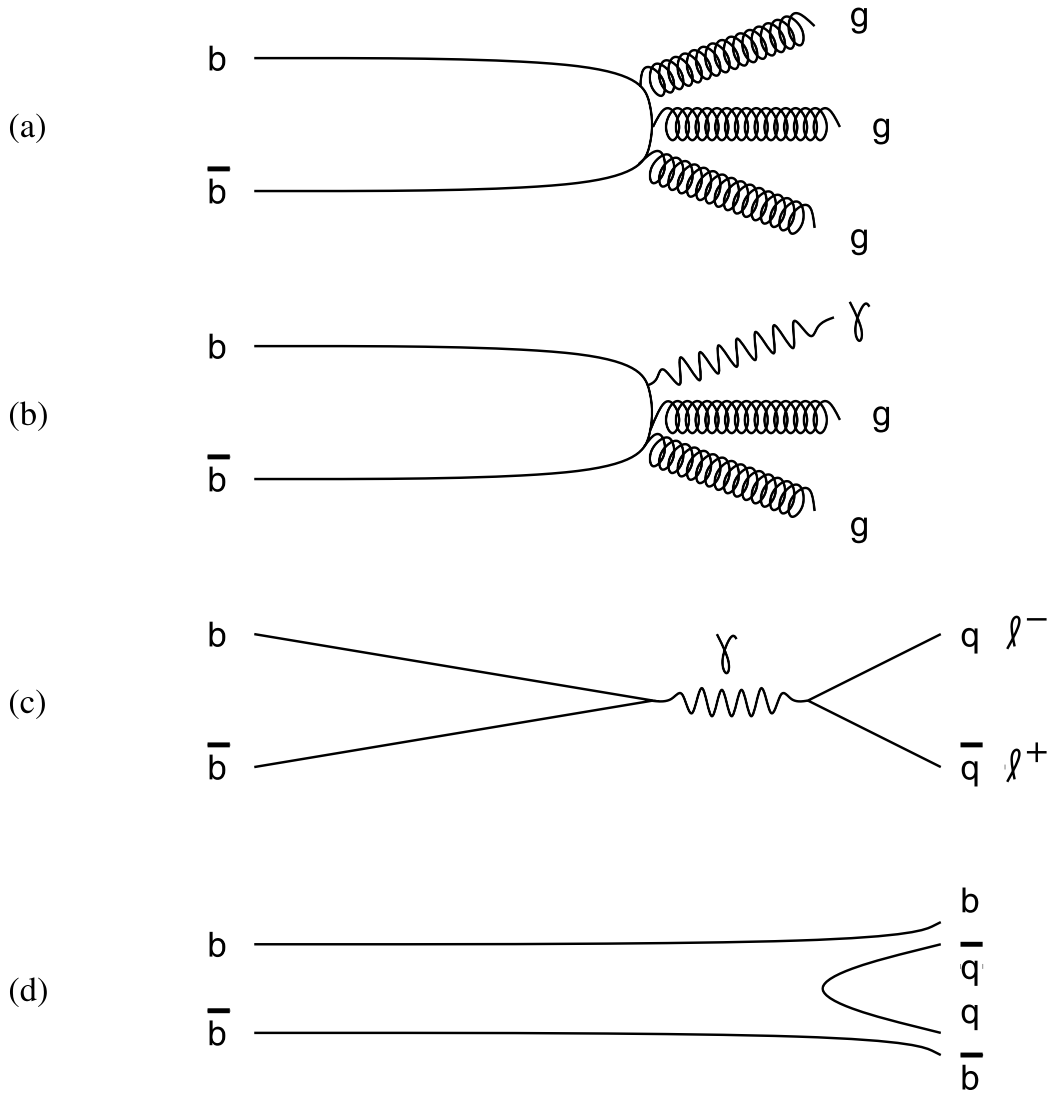

Figure 1.2: Decay mechanisms of the Υ resonances; (a) through (c) show how the $\Upsilon(1S)$ through $\Upsilon(3S)$ resonances decay via annihilation of the b and $\bar{b}$ quarks, and (d) shows how B mesons are formed in $\Upsilon(4S)$ decay.

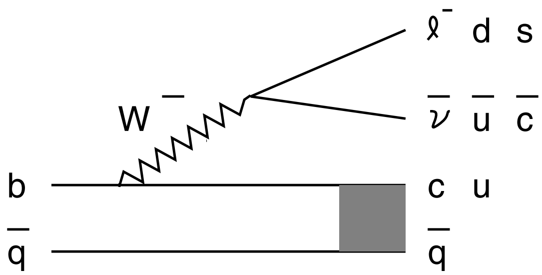

(a) Spectator

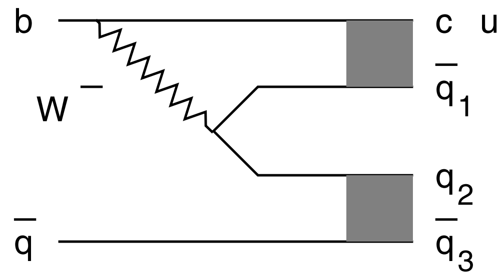

(b) Color Mixed

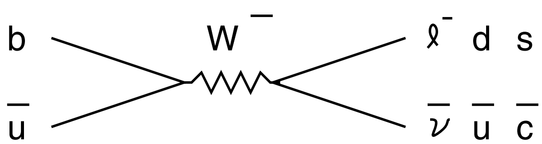

(c) Annihilation

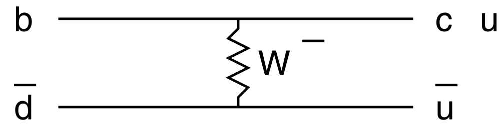

(d) Exchange

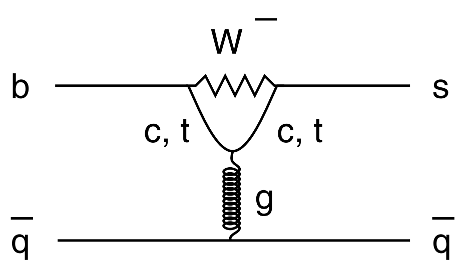

(e) Penguin

Figure 1.3: Decay mechanisms of the B meson, shown in form of the quark level diagrams: (a) External W-emission ("spectator"), (b) Internal W-emission ("color mixed"), (c) Annihilation, (d) W-exchange, and (e) gluonic "Penguin."

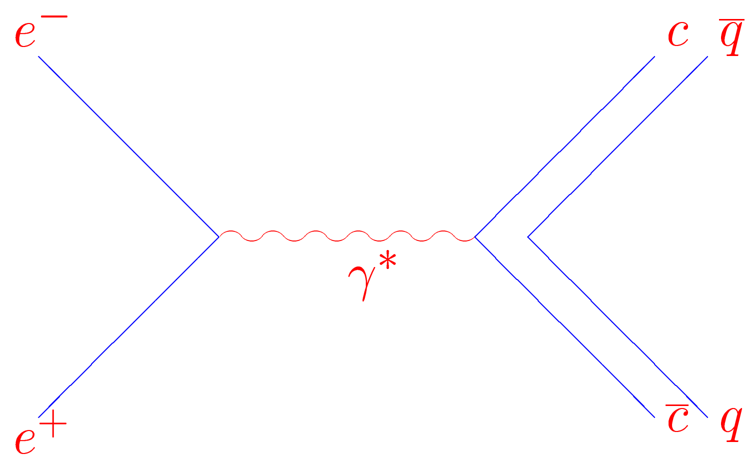

Figure 1.4: Charm mesons from continuum.

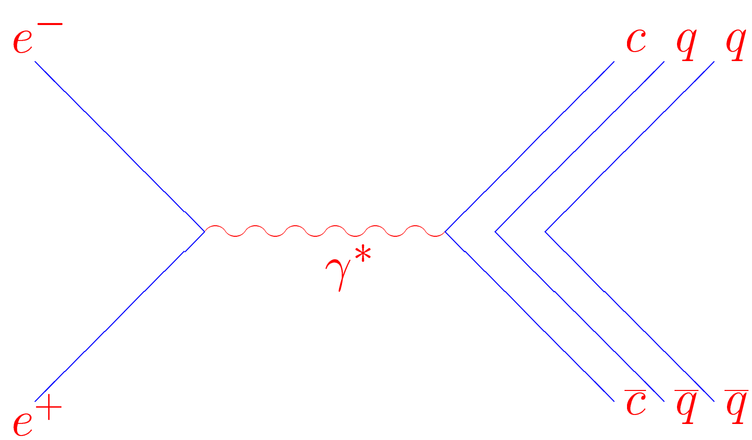

Figure 1.5: Charm baryons from continuum.

1.2.2 $e^+e^-\rightarrow c\overline{c}$

At energies below the $\Upsilon(4S)$ resonance, e^+e^- annihilations can produce any of the four quark - anti-quark pairs as shown below:

$$e^+e^-\rightarrow u\overline{u},\ d\overline{d},\ s\overline{s},\ \text{and},\ c\overline{c}. \tag{1.4}$$

The $\mathrm{q\overline{q}}$ pairs then hadronize, producing the families of mesons and baryons. The hadronic cross-section for the $c\overline{c}$ production is 40% of the total cross-section, so that we get copious $c\overline{c}$ jets just below the $\Upsilon(4S)$ resonance. Figures 1.4 and 1.5 represent possible ways of charmed mesons and charm baryon production at *BABAR*. Most of the times a charmed baryon does not accompany the corresponding charmed anti-baryon, but does accompany some other anti-baryon to conserve baryon number. The decays mechanism of charmed baryons, specific to this thesis, will be discussed later in the next chapter.

Chapter 2

Theoretical Overview

2.1 The Standard Model

The Standard Model SM) is a field theoretic description of unifying the strong and electroweak forces into one framework and is based on the SU(3)$_C\otimes$SU(2)$_L\otimes$ U(1)$_Y$ gauge group. The group symmetry of the Electromagnetic force (QED), U(1)$_e m$, appears in the SM as a subgroup of SU(2)$_L\otimes$ U(1)$_Y$ and it is in this sense that the weak and electromagnetic forces are said to be unified. The SU(2) group represents the Weak force and the SU(3) group represents the Strong force (QCD). The form of Lagrangian in the Standard Model is;

$$\mathcal{L} = \sum \bar{f} i \not{\mathcal{D}} f - V, \tag{2.1}$$

where the sum is over all the fermions f and V contains mass terms and the Higgs field. The covariant derivative $\mathcal{D}$ contains a term for each gauge symmetry of the theory.

$$\mathcal{D}_\mu = \partial_\mu - ig_1 \frac{Y}{2} B_\mu - ig_2 \frac{\tau^i}{2} W^i_\mu - ig_3 \frac{\lambda^a}{2} G^a_\mu, \tag{2.2}$$

where g_1, g_2, and g_3 are the electromagnetic, weak and strong coupling constants, respectively. In the current "Standard Model" there are three types of elementary particles: *leptons*, *quarks*, and *mediators*, as discussed in Section 1.1. In this model, both leptons and quarks are grouped into three generations of electroweak doublets:

$$\begin{pmatrix} \nu_e \\ e \end{pmatrix} \quad \begin{pmatrix} \nu_\mu \\ \mu \end{pmatrix} \quad \begin{pmatrix} \nu_\tau \\ \tau \end{pmatrix}$$

$$\begin{pmatrix} u \\ d' \end{pmatrix} \quad \begin{pmatrix} c \\ s' \end{pmatrix} \quad \begin{pmatrix} t \\ b' \end{pmatrix}$$

In a lepton doublet, the upper component has electric charge 0 and the lower component has electric charge -1 in units of charge; in a quark doublet, the upper and lower components have charge $+\frac{2}{3}$ and $-\frac{1}{3}$, respectively.

During a weak decay a fermion (lepton or quark) transforms into its doublet partner by emission of a charged weak boson $W^\pm$. The $W^\pm$ can then either materialize into a fermion or anti-fermion pair belonging to the same doublet, or couple to another fermion and transform it to its doublet partner. A weak decay can be represented as the interaction of two fermion currents (either leptonic or hadronic), mediated by a charged $W^\pm$ bosonic current. Since only transitions between doublet partners are possible, the weak decay can take place only if it is energetically allowed, i.e., if the ancestor fermion has a larger mass than the daughter fermion. For this reason the quark u and the lepton e, being the lowest mass quark and lepton, do not decay.

The lower component of the electroweak quark doublets d', s', b' are not the mass eigenstates entering the QCD Lagrangian d, s, b, but are linear combinations defined by*

$$\begin{pmatrix} d' \\ s' \\ b' \end{pmatrix} = \begin{pmatrix} V_{ud} & V_{us} & V_{ub} \\ V_{cd} & V_{cs} & V_{cb} \\ V_{td} & V_{ts} & V_{tb} \end{pmatrix} \begin{pmatrix} d \\ s \\ b \end{pmatrix} \tag{2.3}$$

The 3×3 matrix which mixes the mass eigenstates d, s, b into the electroweak eigenstates d', s', b' is called the Cabibbo-Kobayashi-Maskawa (CKM) matrix†. The element V_{ij} describes the strength of the coupling of the weak eigenstate i to the mass eigenstate j by the charged weak current. The individual elements V_{ij} must be determined experimentally. This is a (complex) unitary matrix which depends on four independent parameters (since the phases of five of the six quark fields can be chosen arbitrarily). One possible parameterization consists of choosing the degrees of freedom to be expressed by three real angles of rotation (i.e., the parameters for a rotation in a three dimensional Euclidean space) and a complex phase [2]:

$$\begin{pmatrix} c_{12}c_{13} & s_{12}c_{13} & s_{13}e^{-i\delta_{13}} \\ -s_{12}c_{23} - c_{12}s_{23}s_{13}e^{i\delta_{13}} & c_{12}c_{23} - s_{12}s_{23}s_{13}e^{i\delta_{13}} & s_{23}c_{13} \\ s_{12}s_{23} - c_{12}c_{23}s_{13}e^{i\delta_{13}} & -c_{12}s_{23} - s_{12}c_{23}s_{13}e^{i\delta_{13}} & c_{23}c_{13} \end{pmatrix}, \tag{2.4}$$

with $c_{ij} = cos\theta_{ij}$, $s_{ij} = sin\theta_{ij}$, and i, j denoting the quark generations. Using experimental data, and assuming only three generations of quarks, the 90% confidence limits on the magnitude of the elements of the complete matrix are:

$$\begin{pmatrix} 0.9745 \text{ to } 0.9757 & 0.219 \text{ to } 0.224 & 0.002 \text{ to } 0.005 \\ 0.218 \text{ to } 0.224 & 0.9736 \text{ to } 0.9750 & 0.036 \text{ to } 0.046 \\ 0.004 \text{ to } 0.014 & 0.034 \text{ to } 0.046 & 0.9989 \text{ to } 0.9993 \end{pmatrix} \tag{2.5}$$

*by convention the mixing is only formulated in the (d, s, b) sector; it could as well be formulated in the (u, c, t) sector or in both by simply redefining the phrases of the quark fields - no measurable physical results would change.

†No mixing exists in the lepton sector, provided the lepton neutrinos are massless.

The ranges shown are for the individual matrix elements. The constraints of unitarity connect various elements, so choosing a specific value for one element restricts the range of others.

In the limit $s_{23} = s_{13} = 0$, the third generation of quarks decouple from the first two and the 2×2 upper portion of the CKM matrix becomes:

$$\begin{pmatrix} \cos\theta_c & -\sin\theta_c \\ \sin\theta_c & \cos\theta_c \end{pmatrix} \tag{2.6}$$

which is called the N. Cabibbo matrix and was first introduced by Cabibbo in the framework of a four quark model [2]. The Cabibbo matrix is parameterized by a single real parameter, the Cabibbo angle $\theta_c \sim 13°$.

The coupling constant associated with a quark electroweak vertex $Q \rightarrow qW^{\pm}$ (describing the decay of a heavier quark Q into a lighter quark q) is proportional to the CKM matrix element V_{Qq}. The rate of the decay is proportional to $|V_{Qq}|^2$.

The most probable weak decays between quarks are $t \rightarrow b$, $c \rightarrow s$ and $u \rightarrow d$, this is a reflection of the fact that the diagonal elements of the CKM matrix are close to unity. The off-diagonal elements are much smaller, and therefore the corresponding transitions $t \rightarrow s$, $b \rightarrow c$, $c \rightarrow d$ and $s \rightarrow u$ are much less likely to happen. Finally, the remaining 2 elements V_{ub}, V_{td} are close to zero, making the decays $t \rightarrow d$ and $b \rightarrow u$ extremely unlikely. In the context of four quark model, the matrix elements of $c \rightarrow s$ and $u \rightarrow d$ are proportional to $\cos^2\theta_c$. These transitions are called *Cabibbo-favored* (Figure 2.1, 2.2), while the transitions either with $c \rightarrow d$ or $s \rightarrow u$ have a matrix element proportional to $\cos\theta_c \sin\theta_c$ and decay rate proportional to $\sin^2\theta_c$, are said to be *Cabibbo-suppressed* (Figure 2.3, 2.4, 2.5, 2.6). The transitions with both $c \rightarrow d$ and $s \rightarrow u$ have a matrix element proportional to $\sin^2\theta_c$ and decay rates proportional to $\sin^4\theta_c$. The decay rates proportional to $\sin^2\theta_c$ are called singly *Cabibbo-suppressed* and those proportional to $\sin^4\theta_c$ are doubly *Cabibbo-suppressed*. Here the discussion is confined to the former ones and latter ones are out of the scope of this analysis. vspace1.0in

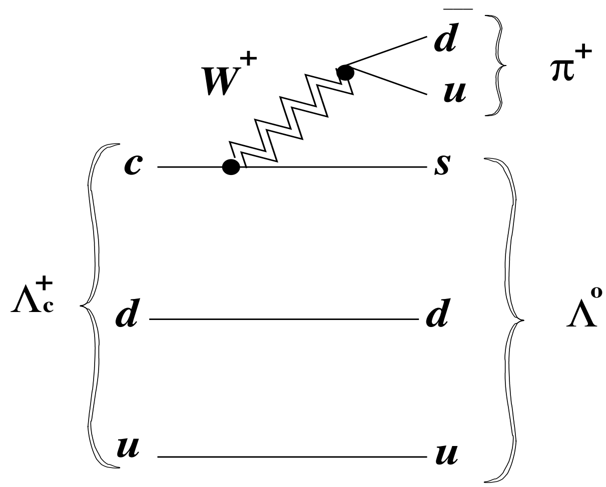

Figure 2.1: Feynman graph for $\Lambda_c^+ \rightarrow \Lambda^0\ \pi^+$(Cabibbo-favored mode).

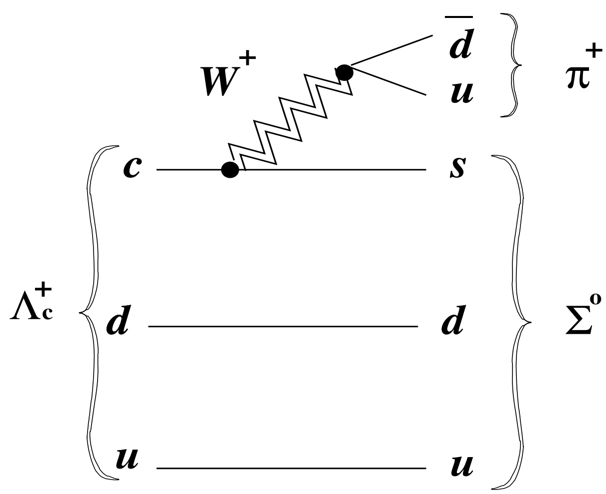

Figure 2.2: Feynman graph for $\Lambda_c^+ \rightarrow \Sigma^0\ \pi^+$(Cabibbo-favored mode).

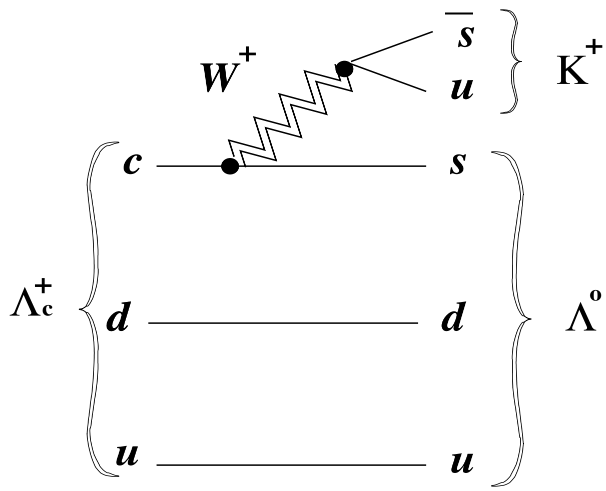

Figure 2.3: Feynman graph for $\Lambda_c^+ \!\rightarrow\! \Lambda K^+$(Cabibbo-suppressed mode).

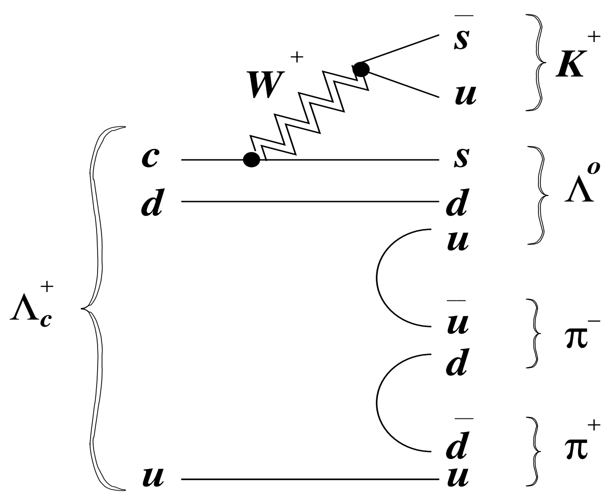

Figure 2.4: Feynman graph for $\Lambda_c^+ \!\rightarrow\! \Lambda K^+ \pi^+ \pi^-$(Cabibbo-suppressed mode).

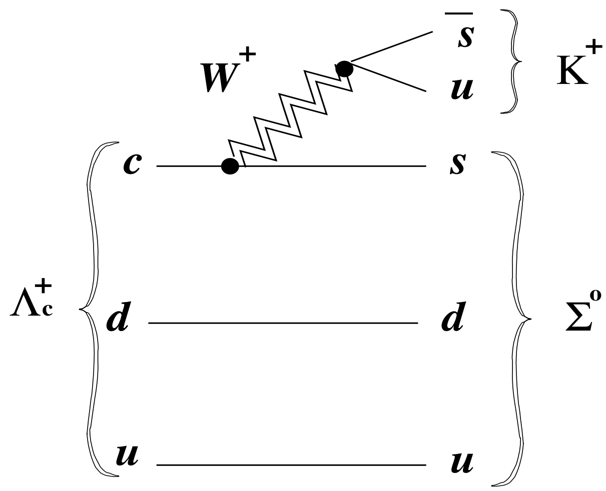

Figure 2.5: Feynman graph for $\Lambda_c^+ \rightarrow \Sigma\ K^+$(Cabibbo-suppressed mode).

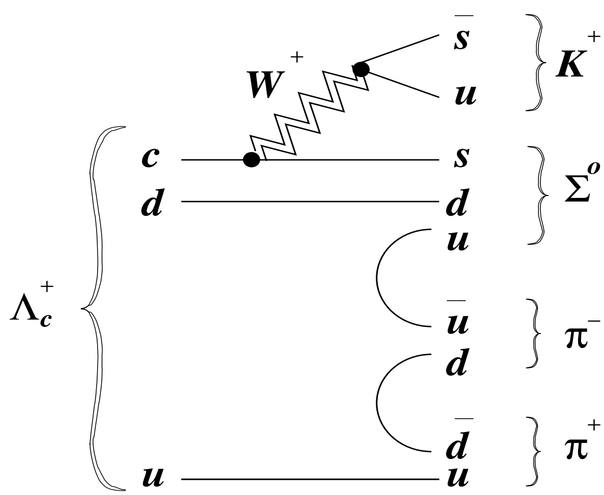

Figure 2.6: Feynman graph for $\Lambda_c^+ \rightarrow \Sigma\ K^+\pi^+\pi^-$(Cabibbo-Suppressed mode).

2.1.1 Weak Decay Mechanism of Charm Hadrons

In the Standard Model, the charm quark decays via a weak charged current into the strange or down quark. The lowest order diagrams through which the decay can proceed are shown in Figure 2.7.

In the (external) spectator decay (Figure 2.7a), the W boson emitted by the charmed quark either materializes as a charged lepton and a neutrino pair (semileptonic decay), or as a quark-antiquark pair (hadronic decay), which then hadronizes into a daughter meson (K or π). The light antiquark $\overline{q}$ is a spectator to the charm decay process and afterwards combines with the daughter s or d quark to form another daughter meson. In the spectator mechanism, the decay rate into any $q\overline{q}$ pair is favored by a factor of three over the decay rate into a $l\nu_l$, because there are three color degress of freedom.

In the internal spectator decay (Figure 2.7b), the $q\overline{q}$ pair resulting from the W boson decay couples to the charm daughter quark s or d and the light antiquark $\overline{q}$ to produce the final state hadrons. Since the color degree of freedom of the coupling quarks must match, the internal spectator decay rate is suppressed by a factor of three with respect to the external spectator rate. The final state for an internal spectator decay is always purely hadronic.

In the annihilation diagram (Figure 2.7c), the charmed quark combines with its light antiquark partner to produce a virtual W, which then decays into a charged lepton and a neutrino pair (purely leptonic decay) or a quark-antiquark pair (hadronic decay). The hadronic modes are again favored by the color degrees of freedom with respect to the leptonic modes.

In the exchange diagram (Figure 2.7d), the charmed quark and the light antiquark composing the meson exchange a virtual W boson and transform into their doublet partners. The final state is always hadronic.

In the case of *charmed meson*, the decay rates for both the annihilation and the exchange diagrams are helicity-suppressed[‡], and consequently the spectator diagrams are expected to be the dominant mechanisms of decay. In the case of *charmed Baryons*, helicity suppression is avoided by the presence of the additional light quark, so that both the internal spectator and exchange diagrams may in principle contribute significantly to the total decay rate (no annihilation diagram is possible for baryons).

[‡]In the weak decay proceeding through the exchange or annihilation diagram, angular momentum conservation forces the two outcoming fermions to have the same helicity, i.e., to be both left-handed or both right-handed. Since in the Standard Model leptons are preferentially left handed and antileptons are preferentially right-handed, this means that one of the two daughters is forced to be suppressed.

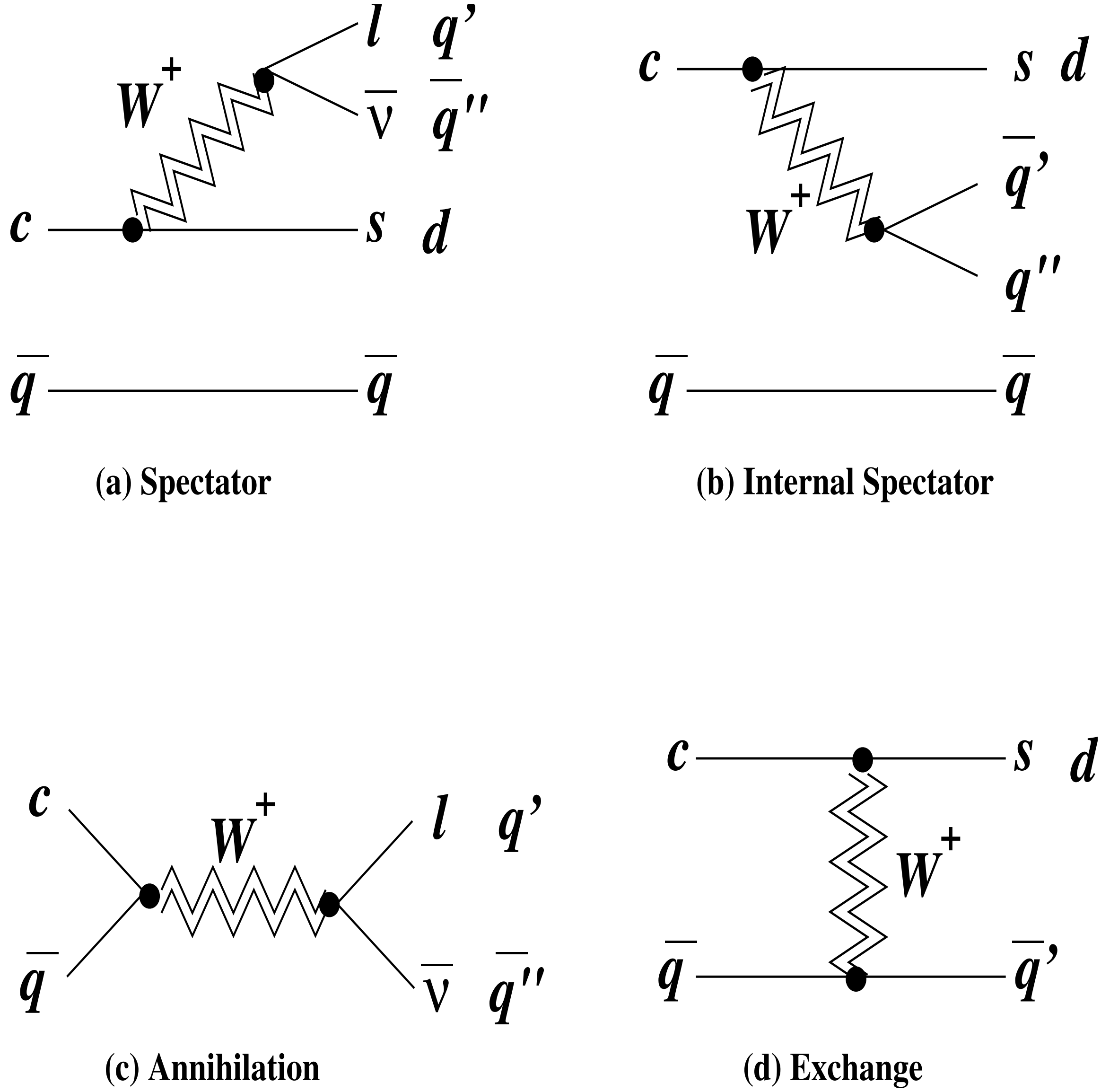

Figure 2.7: Decay mechanisms of the charmed meson, shown in form of quark level diagrams: (a) External W-emission ("spectator"), (b) Internal W-emission ("color mixed"), (c) Annihilation, (d) W-exchange.

Table 2.1: Quantum numbers of four quarks under SU(4)

Symbol	Q[e]	T	T_3	S	B	Y	C
u	$\frac{2}{3}$	$\frac{1}{2}$	$\frac{1}{2}$	0	$\frac{1}{3}$	$\frac{1}{3}$	0
d	$-\frac{1}{3}$	$\frac{1}{2}$	$-\frac{1}{2}$	0	$\frac{1}{3}$	$\frac{1}{3}$	0
s	$-\frac{1}{3}$	0	0	-1	$\frac{1}{3}$	-$\frac{2}{3}$	0
c	$\frac{2}{3}$	0	0	0	$\frac{1}{3}$	$\frac{1}{3}$	1

2.2 Charm Spectroscopy

The discovery of the J/ψ [3, 4] at a mass of 3.1 GeV/c^2 in 1974 led to the era of **Charm Physics**. The resonance was identified as a bound state of charm and anti-charm quark with the mass of $m_c \sim 1.5$ GeV/c^2 and charge 2/3. Later, more resonances with charm quarks were identified. In 1975, the first charmed baryon state Λ_c^+ was discovered at BNL [5] in neutrino interactions using a bubble chamber. With the advent of new powerful accelerators more charmed mesons and baryons were revealed, and the quark model got a big boost and hence the spectroscopic study of charmed baryons and charmed mesons followed. From then on the fourth flavor has been assigned an additional quantum number "charm C" ($C = 1$), isospin $T = T_3 = 0$ and hypercharge $Y = \frac{1}{3}$. The fourth c quark is a singlet under the SU(3) flavor symmetry. Now we have four quarks, the group which incorporates *u, d, s, c* quarks under one framework is the SU(4) group, while the SU(3) remains a subgroup of the SU(4). Like SU(3), the fundamental representations of the SU(4) are [**4**] for quarks and [$\overline{\mathbf{4}}$] for anti-quarks and their quantum numbers are listed in Table 2.1. In subsequent years $\Upsilon(b\overline{b})$ [6] and other heavy mesons and baryons were discovered and identified.

The heavy hadrons composed of charm and bottom quarks are quite different from the light flavored hadrons composed of u, d, and s quarks. This behavior led to the notion of the Heavy Quark Effective Theory (HQET) [7]. In nature we have six quarks grouped into *light* and *heavy* sectors. The *light* sector comprises of u, d, and s quarks with masses less than the scale parameter, $\Lambda_{QCD} \cong 400$ MeV whereas *heavy* sector comprises of c, b, and t quarks with masses much greater than Λ_{QCD}. In the realm of HQET, the QCD Lagrangian is expanded in powers of $1/m_Q$ and the leading terms in the expansion can be interpreted as the heavy quark at the center being surrounded by the light quark cloud, and the light quark cloud interacts with the heavy center via gluons. Gluons do not distinguish flavor hence the light quarks, also known as *light degrees of freedom* (light quark and gluons), do not see the flavor of the heavy quark. The heavy nature of the charm or bottom quark at the center decouples the spins of light quarks from the center. In the heavy quark mass limit, a bottom baryon at rest is identical to a charm baryon at rest. The *light degrees of freedom* look the same regardless of the flavor and the spin orientation of the heavy quark. Therefore, there are two heavy quark symmetries: one is the flavor symmetry and the second is spin symmetry.

Now under the SU(4) flavor symmetry hadrons are classified as $[\mathbf{4}] \otimes [\overline{\mathbf{4}}]$ mesons $(q\overline{q})$ and $[\mathbf{4}] \otimes [\mathbf{4}] \otimes [\mathbf{4}]$ baryons (qqq).

In mesons we have two quarks, each with spin 1/2. From elementary quantum mechanics, the two spin half particles can have either spin 1, or spin 0 depending on how the two quarks aligned as parallel or anti-parallel to each other.

$$\mathbf{S} = \frac{1}{2} \otimes \frac{1}{2} = 1 \oplus 0,$$

whereas for baryons the three quarks have somewhat different configurations,

$$\mathbf{S} = (\frac{1}{2} \otimes \frac{1}{2}) \otimes \frac{1}{2} = (0 \oplus 1) \otimes \frac{1}{2} = \frac{1}{2} \oplus \frac{3}{2}.$$

Angular momentum falls under O(3) group. The hadrons can exist in orbital or radial (*e.g.*, $\chi_{b1}(1P)$, $\chi_{b1}(2P)$or $\Upsilon(3S), \Upsilon(4S)$) excitations [8]. Using a constituent quark model picture the underlying SU(4)⊗O(3) symmetry gives rise to a spectrum of charm mesons and charm baryons. Here we will discuss mostly ground state charmed baryon spectroscopy with a brief introduction to charmed mesons. Here the discussion will be confined to the charmed baryons with one charm quark only.

2.2.1 Charmed Meson

In order to determine the *charm* content for mesons [9], the SU(4) representation $[\mathbf{4}]$ (u, d, s, c) decomposes under SU(3) as the SU(3) triplet $[\mathbf{3}]$ (u, d, s) and the SU(3) singlet $[\mathbf{1}]$ (c). For mesons, we write

$$[\mathbf{4}] \otimes [\overline{\mathbf{4}}] = [[\mathbf{3}] \oplus [\mathbf{1}]^1] \otimes [[\overline{\mathbf{3}}] \oplus [\mathbf{1}]^{-1}]$$

where,

$[\mathbf{3}]$ and $[\overline{\mathbf{3}}]$ are the SU(3) triplets,

$[\mathbf{1}]^1$ is the SU(3) singlet with C=1,

$[\mathbf{1}]^{-1}$ is the SU(3) singlet with C=-1.

$$[\mathbf{4}] \otimes [\overline{\mathbf{4}}] = [\mathbf{8}]^0 \oplus [\mathbf{1}]^0 \oplus [\mathbf{3}]^{-1} \oplus [\overline{\mathbf{3}}]^1 \oplus [\mathbf{1}]^0$$

where the term $[\mathbf{8}]^0$ and $[\mathbf{1}]^0$ makeup the SU(3) nonet, $[\mathbf{3}]^{-1}$ and $[\overline{\mathbf{3}}]^1$ come from the association of the charm quark with the SU(3) triplet representation, $[\mathbf{3}]^{-1}$ states are the D^0 ($c\overline{u}$), D_s^+ ($c\overline{s}$), D^+ ($c\overline{d}$) and $[\overline{\mathbf{3}}]^1$ states are the $\overline{D}^0$ *($u\overline{c}$)*, D_s^- *($s\overline{c}$)*, D^- *($d\overline{c}$)* and the remaining $[\mathbf{1}]^0$ state is η_c .

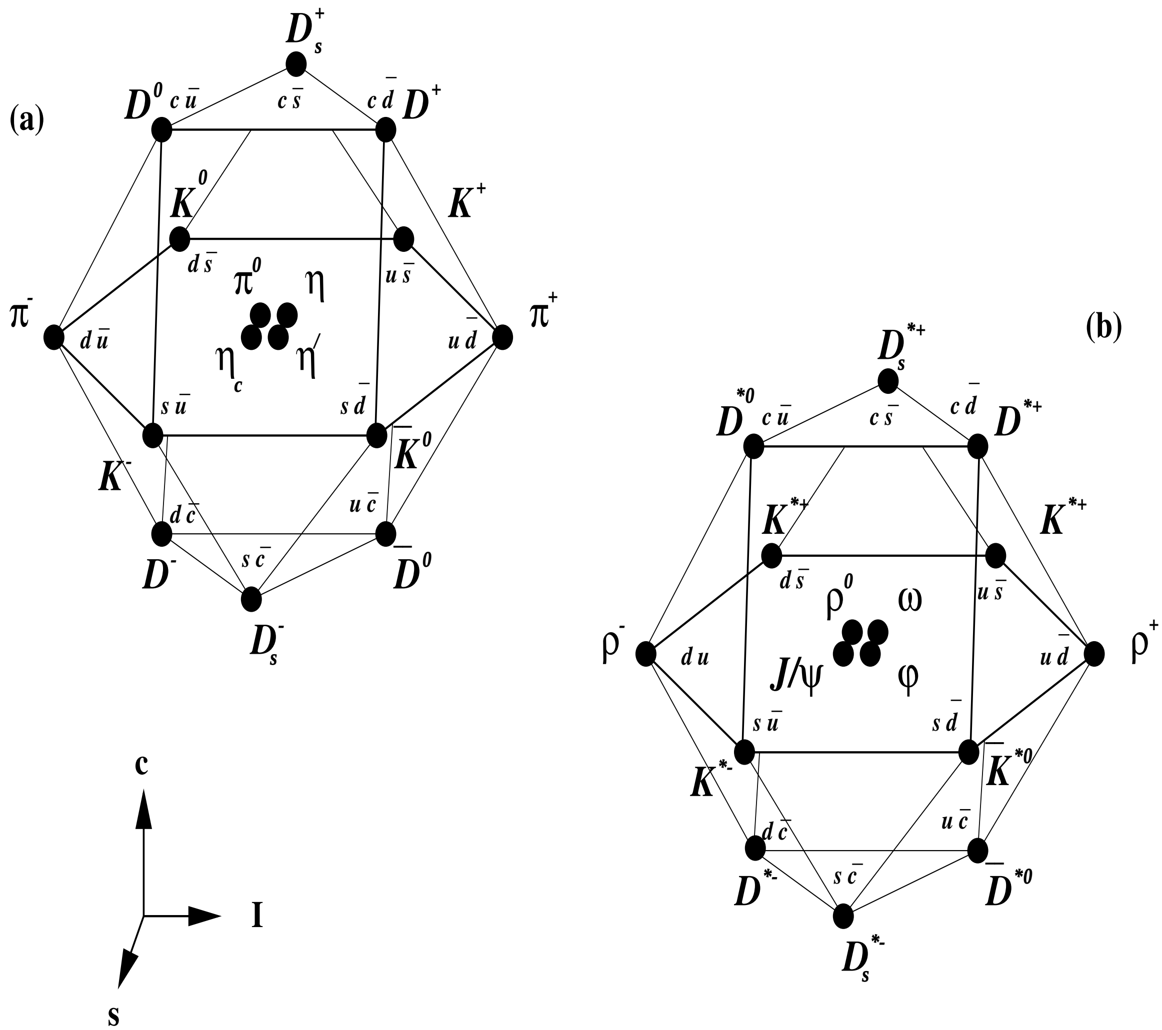

Figure 2.8: SU(4) 16-plets for the (a) pseudoscalar and (b) vector mesons composed of u, d, s, and c quarks. The nonets of the light mesons occupy the central plane, to which $c\overline{c}$ states have been added. The neutral mesons at the centers of these planes are mixtures of $u\overline{u}$, $d\overline{d}$, $s\overline{s}$, and $c\overline{c}$ states.

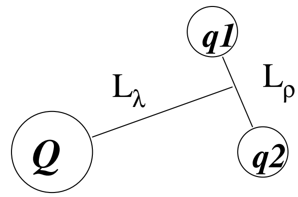

Figure 2.9: L_ρ is the angular momentum of two quarks in the diquark system and L_λ is the relative angular momentum of the diquark in the baryon.

Apart from these mesons with *open charm*, there also exist mesons with *hidden charm*, η_c (paracharmonium spin = 0) and J/Ψ (orthocharmonium spin = 1) bound state of c and $\bar{c}$. For the diquark system the total spin angular momentum can have two possible values, spin 0 or spin 1 and they are classified as *pseudoscalar mesons* ($J^{PC} = 0^{-1}$) and *vector mesons* ($J^{PC} = 1^{-1}$), as shown in Figure 2.8.

2.2.2 Charmed Baryons

The charmed baryons are the bound states formed from a charm quark and a light diquark system. The spin-parity quantum numbers j_l^P of the *light degrees of freedom* are determined from the spin and orbital degrees of freedom of the light quarks in the diquark system. The spin of the diquark can be either 0 or 1. The total orbital angular momentum is the sum of the two angular degrees of freedom L_ρ and L_λ. The L_ρ describes the orbital excitations of the light quarks in the diquark system, and L_λ is the orbital excitation of the light diquark relative to the central heavy quark, as shown in Figure 2.9. Discussions will be limited to the ground state (s-wave) baryons with $L_\rho = L_\lambda = 0$ The light diquark system can have total angular momentum j_l = 0, 1, 2... and parity $P = \pm 1$. To each diquark system with spin-parity j_l^P there is a degenerate heavy baryon doublet with $J^P = (j_l \pm \frac{1}{2})^P$. Exception is the case

$j_l = 0$, since spin half of the charm quark couples with $j_l = 0$ and gives a singlet. In the framework of the quark model, the total wavefunction of a baryon can be factorized as a product of different components as shown below, since each part is independent [10],

$$\Psi = \psi_C \chi \psi_L \psi_F \psi_R \tag{2.7}$$

where ψ_C represents the color part of the wave function, χ denotes the spin wavefunction, ψ_L denotes the angular part of the spatial wavefunction, ψ_F represents the flavor part of the wavefunction, and ψ_R represents the radial part of the spatial wavefunction. The total wavefunction has to be anti-symmetric, since all baryons are fermions. The color part is always anti-symmetric under interchange of a pair of quarks. The ρ and λ coordinates are so chosen to diagonalize the Hamiltonian for the *Potential model* for baryons (two coordinates become independent of each other). The ρ angular part of the spatial wavefunction has a symmetry of $(-1)^{L_\rho}$ under interchange of quarks in the diquark system, whereas the λ angular part of spatial wavefunction is symmetric under interchange of quarks in the diquark system. The radial part is always symmetric under the interchange of quarks, because of the spherical symmetry.

S-wave Baryons

As discussed in the chapter 1, baryons are formed from "qqq" combinations. To determine the charm content we decompose the result into representations of the SU(3) subgroup [9].

$$[\mathbf{4}] \otimes [\mathbf{4}] \otimes [\mathbf{4}] = ([\mathbf{6}] \oplus [\mathbf{10}]) \otimes [\mathbf{4}] = [\mathbf{4}]_a \oplus [\mathbf{20}]_{ms} \oplus [\mathbf{20}]_{ma} \oplus [\mathbf{20}]_s. \tag{2.8}$$

whereas the term $[\mathbf{20}]_{ms}$ and $[\mathbf{20}]_{ma}$ are essentially[§] the same from now on we call them $[\mathbf{20}]$-plet and $[\mathbf{20}]_s$ differ by the composition of SU(3)-multiplets, both contain 20 states, but different SU(3)-multiplets. With three spin half quarks the total angular momentum a baryon can have is either spin 1/2 or spin 3/2. The [20]-plet (spin 1/2) decomposes as under SU(3) $[\mathbf{8}]^0$ with no charm (SU(3) octet), $[\mathbf{3}]^1$ anti-symmetric with one charm (diquarks in antisymmetric configuration Λ_c, Ξ_c^+, and Ξ_c^0), $[\mathbf{6}]^1$ symmetric with one charm (diquark in symmetric configuration Σ_c, Ξ_c', and Ω_c^0), and $[3]^2$ with two charm quarks, (Ξ_{cc}^+, Ξ_{cc}^{++}, Ω_{cc}^+). Similarly, the $[\mathbf{20}]_s$-plet (spin 3/2) under SU(3) decomposes as $[10]^0$ with no charm (SU(3) decuplet), $[\mathbf{6}]^1$ with one charm (Σ_c^*, Ξ_c^*, Ω_c^{0*}), $[\mathbf{3}]^2$ with two charm quarks (Ξ_{cc}^+, Ω_{cc}^+), and $[\mathbf{1}]^3$ with three charm quarks (like Ω_{ccc}^{++}). The $[\mathbf{4}]_a$-plet reproduces part of antisymmetric states in the $[\mathbf{20}]$-plet (Λ, Λ_c, Ξ_c^0, and Ξ_c^+). The two SU(4) 20-plets are shown in Figure 2.10. Consider the Λ_c^+ ($c[ud]$) state in which the diquark $[ud]$ has I = 0, isospin singlet and hence antisymmetric. The total orbital angular momentum for the Λ_c^+ is L = 0 therefore it is symmetric in ψ_L, as the color wavefunction is antisymmetric. In order for the entire wavefunction to be antisymmetric the spin configuration of the diquark should be antisymmetric, spin = 0. The iospin I = 1 partners of the Λ_c^+ are the Σ_c states. Since the flavor (isospin) part is symmetric this implies that the spin of the diquark $\{q_1 q_2\}$ in the Σ_c states should be 1. The spin 1/2 of the charm quark makes the Σ_c system a doublet in 'spin space' $J_P = 1/2^+$ (Σ_c) and $J_P = 3/2^+$ (Σ_c^*). Both the Σ_c and Σ_c^* states decay into Λ_c^+ (being the lightest) via pion transition.

[§] $[\mathbf{20}]_{ms}$ states have diquarks in symmetric combination and $[\mathbf{20}]_{ma}$ states have diquarks in anti-symmetric combination. When the flavor symmetry is combined with the SU(2) of spin symmetry the two multiplets collapse into one.

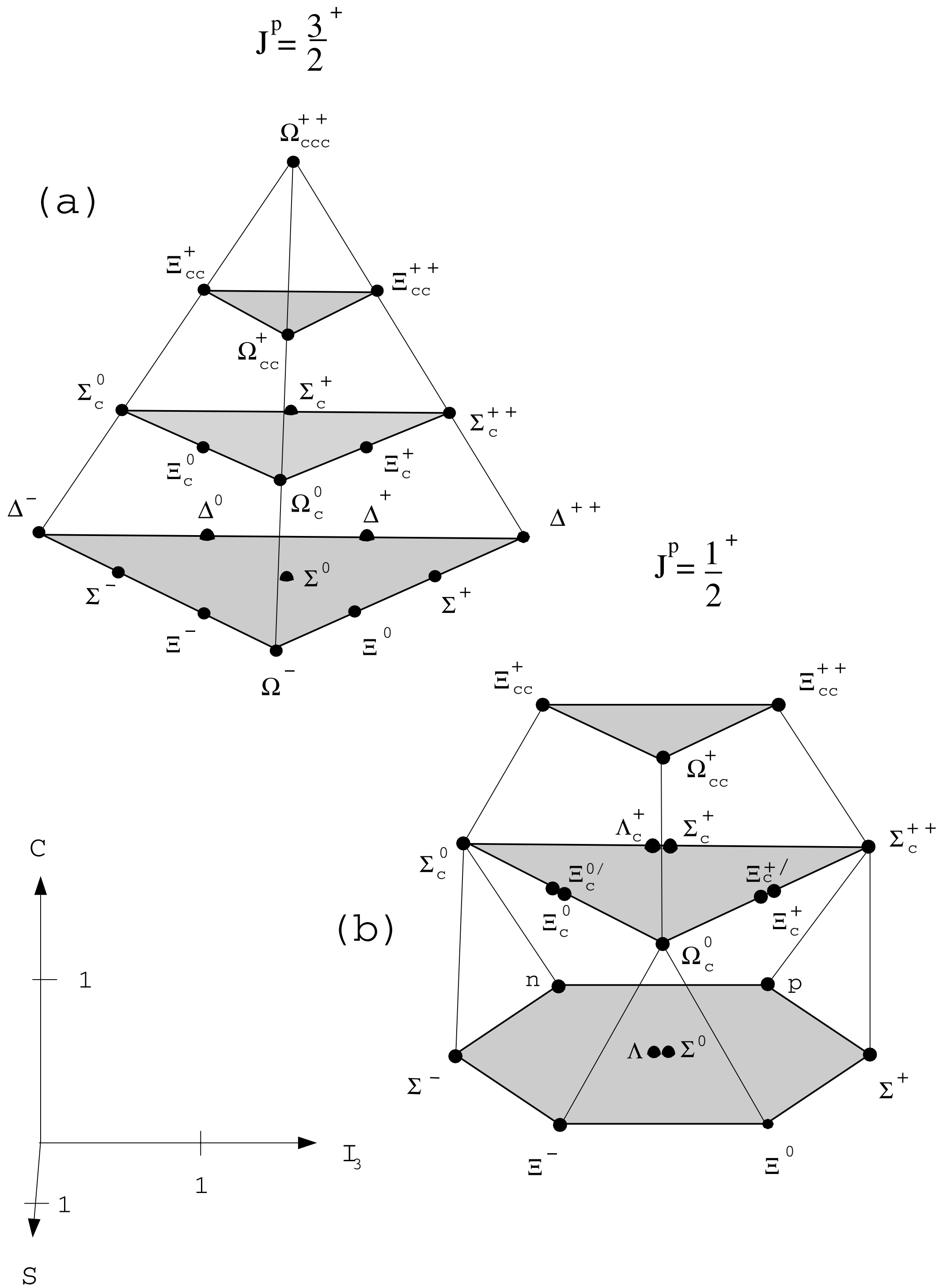

Figure 2.10: SU(4) multiplet of baryons made of u, d, s, and c quarks. (a) The 20-plet with an SU(3) decuplet, $J^P = \frac{3}{2}^+$. (b) The 20-plet with an SU(3) octet, $J^P = \frac{1}{2}^+$.

The Ξ_c system, *csu* and *csd*, contains a strange quark in association with an up or down quark in the diquark system. Now the wavefunction can be symmetric $\{sq\}$ or antisymmetric $[sq]$. If the diquark is in antisymmetric configuration with spin = 0, then we get the Ξ_c^0 and Ξ_c^+ states. If the diquark is in symmetric configuration with spin = 1 then the pair couples with the third charm quark spin and results in the $\Xi_c'(J^P = \frac{1}{2}^+)$ and $\Xi_c^*(J^P = \frac{3}{2}^+)$ states. Ξ_c' is below the pion transition threshold, therefore decays via photon (electromagnetic) transition into the Ξ_c state, while the Ξ_c^* is massive enough to decay into a pion and Ξ_c ground state.

The charmed baryons with quark content *css*, can have only symmetric configuration in the diquark system $\{ss\}$. The diquark with spin 1 couples with the heavy charm quark resulting in two states; Ω_c^0 with $J^P = \frac{1}{2}^+$ and Ω_c^* with $J^P = \frac{3}{2}^+$. The Ω_c^* is expected below the pion transition threshold, therefore it decays electromagnetically to the Ω_c^0 ground state, as shown in Figure 2.11.

2.2.3 Scope of The Thesis

Charmed baryon physics is still a relatively new endeavor when one considers that a significant portion of the charm baryon physics remain undiscovered. The baryon spin-1/2 and spin-3/2 multiplets are discussed in detail in the previous section and are depicted in figure 2.10; only recently the majority of the first group of spin-1/2 charm baryons have been observed experimentally. The lightest charmed baryon Λ_c^+ is the main focus of this thesis.

A wealth of large amount of data from the experiments like *BABAR* will help to understand and improve the the theoretical predictions made by the spectator quark model analysis [36, 37] of incorporating the new information on charm baryon masses, lifetimes and decay branching fractions. Also the present theoreical understanding of the hadrons composed of heavy and light quarks and transitions among such heavy hadrons in the context of heavy quark effective theory (HQET) [15, 38] which puts the quark model approach to non-leptonic charm baryon decays on a much sound theoretical footings. Some of the theoretical predictions relative this thesis are listed in Table 2.2.

The goal of this thesis is to measure the relative branching fractions of the

Table 2.2: Branching fractions for the Λ_c^+ decay modes, as predicted by the theory, using spectator quark model approach [36]

Decay mode	Ratio of Branching Fration
$\Lambda_c^+ \to \Lambda K^+$	$(0.09 - 0.12)\%$
$\Lambda_c^+ \to \Sigma^0 K^+$	$(0.02 - 0.08)\%$
$\Lambda_c^+ \to \Lambda \pi^+$	$(2.15 - 2.33)\%$
$\Lambda_c^+ \to \Sigma^0 \pi^+$	$(0.55 - 2.43)\%$

Cabibbo-suppressed channels of the charm baryon Λ_c^+ relative to its Cabibbo-favored decay channel.

Table 2.3 presents the experimental measuremets of previously measured Λ_c^+ *Cabibbo-suppressed* (relative to this thesis) decay modes from the other experiments.

The data were collected with the *BABAR* detector at the PEP-II e^+e^- asymmeteric collider at SLAC¶. The experiment is described in Chapter 3. In Chapter 4, the particle identification (PID) at *BABAR* and PID used in this analysis has been discussed. Chapter 5 discuss, the data reconstruction and processing methods

¶Stanford Linear Accelrator Center

Table 2.3: Λ_c^+ *Cabibbo-suppressed* decay modes, measured from some other experiments [35]

Decay mode	Ratio of Branching Fration
	Realtive to $\Lambda_c^+ \to pK^+\pi^+$
$\Lambda_c^+ \to \Lambda K^+$	$(6.7 \pm 2.5) \times 10^{-4}$
$\Lambda_c^+ \to \Sigma^0 K^+$	$(5.6 \pm 2.4) \times 10^{-4}$
$\Lambda_c^+ \to \Sigma^+ \ K^+\pi^-$	$(1.7 \pm 0.7) \times 10^{-3}$
$\Lambda_c^+ \to pK^+K^-$	$(7.7 \pm 3.5) \times 10^{-4}$
$\Lambda_c^+ \to p\phi$	$(8.2 \pm 2.7) \times 10^{-4}$

as well as the branching fraction measurements. The results are summarized and concluding remarks are also given in Chapter 5.

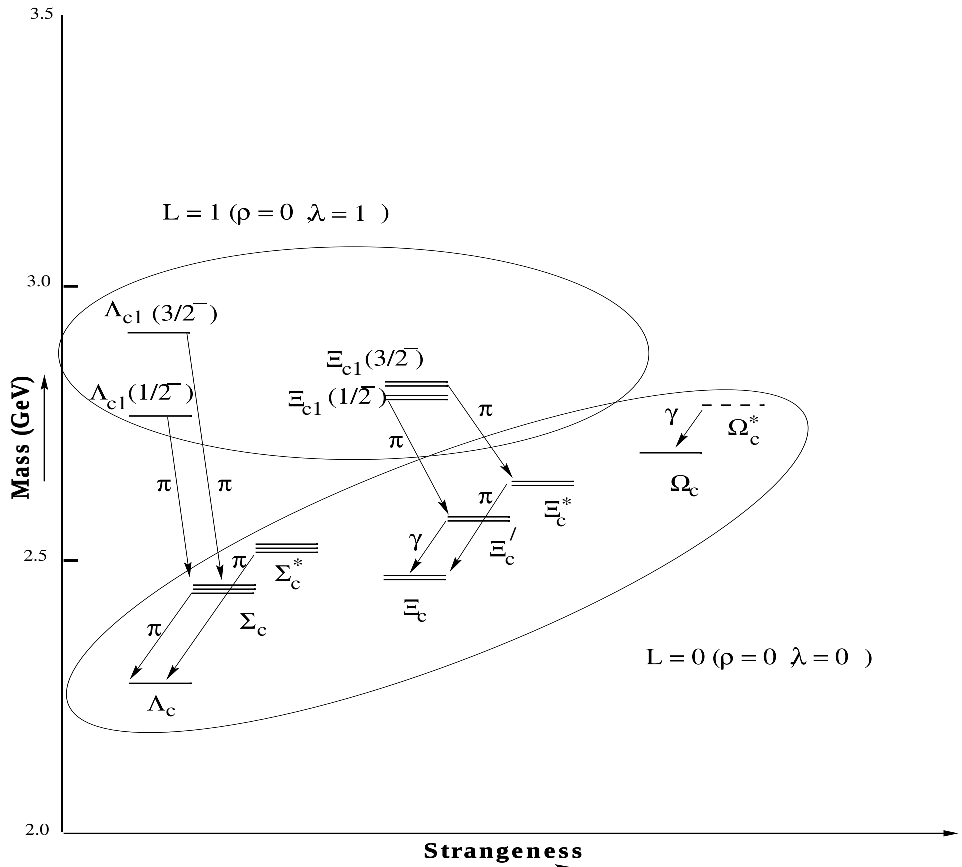

Figure 2.11: Decay transitions of ground state and L = 1 baryons via π and γ.

Chapter 3

The *BABAR* Experiment

The motivation of the *BABAR* detector at SLAC is to study the physics at the $\Upsilon(4S)$ resonance using a high-luminosity, asymmetric e^+e^- collider. In particular, to test the Kobayashi and Maskawa mechanism for CP-violation [2], so as to probe the Standard Model (SM). A detailed description of the *BABAR* detector and PEP-II can be found in [25, 26, 27].

In this chapter we shall provide an overview of PEP-II and also the various sub-detectors of *BABAR*.

Although the B-Factory design was optimized for the study of CP asymmetries in the SM and rare decays in the neutral B meson system, it is also an excellent facility at which to study other types of physics more precisely, such as charm, tau, B (non-CP physics) and two-photon. This thesis is dedicated to the study of the Λ_c^+ baryon, taking advantage of the large sample of charm baryons provided by the high luminosities of PEP-II . Brief descriptions of PEP-II and the *BABAR* detector follow in Sections 3.2 and 3.3 respectively.

3.1 Data Sample

On October 22, 1999, the first colliding beam data currently used for physics analysis was recorded by *BABAR*. At that time the instantaneous luminosity of PEP-II was $0.3 \times 10^{33}\ \mathrm{cm^{-2}s^{-1}}$ and the total integrated luminosity for that day was ~ 1 $\mathrm{pb^{-1}}$. Since then, PEP-II has steadily improved and is now consistently delivering instantaneous luminosities well in excess of the nominal design value of $\sim 3.0 \times 10^{33}$ $\mathrm{cm^{-2}s^{-1}}$. Presently, the best PEP-II peak luminosity is $9.2 \times 10^{33}\ \mathrm{cm^{-2}s^{-1}}$ (May 21, 2004) and the best integrated luminosity in 24-hour period is $681.08\ \mathrm{pb^{-1}}$ (May 24, 2004). Figure 3.1 shows the daily recorded luminosity history of the experiment over the entire 1999-2004 running period. As of July 31, 2004, a total integrated luminosity of $244.06\ \mathrm{fb^{-1}}$ had been recorded by *BABAR* - of this total, $221.38\ \mathrm{fb^{-1}}$ has been taken on the $\Upsilon(4S)$ resonance and $22.68\ \mathrm{fb^{-1}}$ has been taken $\approx$ 40-50 MeV below the resonance(Figure 3.2). This off-resonance running is used in B-physics analysis to characterize backgrounds from continuum events but, for non B-physics, it is an integral part of the total dataset. Charm events, which arise from continuum processes not affected by the presence of the $\Upsilon(4S)$ resonance, are the source of nearly all backgrounds in this analysis (Chapter 5), and on- and off-resonance data are therefore treated identically. The $\sim$125 $\mathrm{fb^{-1}}$ data sample used in the present analysis (Table 3.1) was collected beginning with the first colliding beams physics runs in 1999 and ending with the summer 2003 shutdown of the B-Factory for upgrade and repairs.

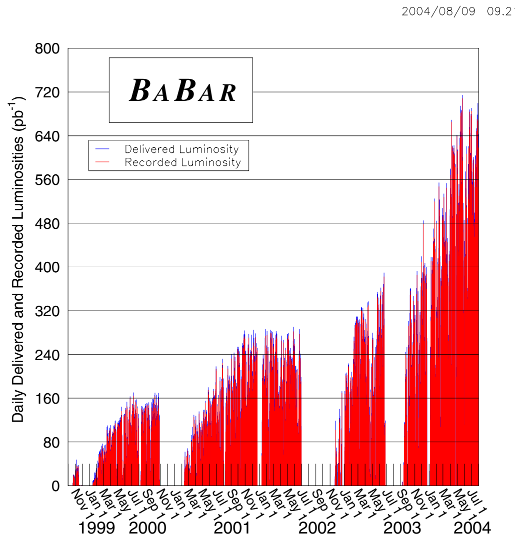

Figure 3.1: Daily recorded luminosity.

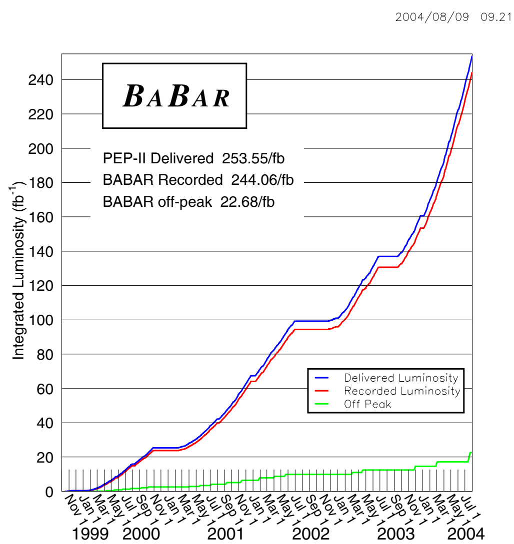

Figure 3.2: Total integrated luminosity.

3.1.1 Monte Carlo Events

Simulated continuum events are produced at *BABAR* using the JetSet generator and a GEANT-based detector model [28] - $\Upsilon(4S)$ events decaying to charged and neutral B

Table 3.1: Composition of the data sample – the small amount of data from 1999 is include in the figures of 2000.

Data Year	Integrated Luminosity (fb^{-1})
on-resonance 2000	18.6
on-resonance 2001	35.8
on-resonance 2002	25.3
on-resonance 2003	33.3
off-resonance all	12.0
Total	125

mesons are produced with several different generators, each of which is dedicated to reproducing as closely as possible the physics of B decays to particular types of final states. *BABAR* has gone through several epochs of event simulation using evolving detector models, generators and reconstruction - the version of simulated events used herein is from the set of events internally designated by *BABAR* as "Simulation Production 5" ("SP5"). As will be repeatedly shown in Chapter 5, there is good agreement between distribution function from data and simulated events for all parameters relevant to this analysis. Wherever a dependence arises in the fit for signal and background events, it is included as part of the systematic uncertainty. The individual samples of generic $q\overline{q}$ simulated events shown in table 3.2 are scaled to the cross-section as presented in the table 3.3 [25]. Simulated signal events were used to study the reconstruction of various Λ_c^+ decays. The *BABAR* offline analysis code base allows both simulated and actual data events to be treated identically and, therefore, both classes of events were analyzed using identical code.

Table 3.2: Composition of the simulated event samples.

Mode	N_{events} ($\times 10^6$)
neutral B (SP5)	18.6
charged B (SP5)	35.8
$c\bar{c}$ (SP5)	25.3
uds (SP5)	33.3

3.2 PEP-II

The PEP-II * is an e^+e^- storage ring. The High Energy Ring (HER) stores 9 GeV electrons and the Low Energy Ring (LER) stores 3.1 GeV positrons. Thus PEP-II operates at a center of mass energy of 10.58 GeV, the mass of the $\Upsilon(4S)$ resonance which is moving with respect to the laboratory frame. The cross-section for the production of fermion pairs at $\Upsilon(4S)$ is shown in Table 3.3.

The asymmetric energies produce a boost of $\beta\gamma = 0.56$ in the laboratory frame in order to facilitate reconstruction of the two B meson daughters resulting from the decay of the $\Upsilon(4S)$. Although the boost is necessary for precision B meson studies, it has no advantage for charm physics.

A schematic representation of the acceleration and the storage system is shown in Figure 3.3. An electron gun is used to create two electron beams that are accelerated to approximately 1 GeV before entering one of the damping rings, whose purpose is to reduce the dispersion in the beams. After that those electrons are accelerated in the Linear accelerator (Linac). Part of the beam is diverted to collide with a tungsten target and to create a positron beam, which in turn passes through the damping ring and is accelerated in the Linac.

*PEP is an acronym for positron Electron Project

Table 3.3: Production cross-section at the $\Upsilon(4S)$ resonance [25].

$e^+e^- \rightarrow$	Cross-section (nb)
$b\bar{b}$	1.05
$c\bar{c}$	1.30
$s\bar{s}$	0.35
$u\bar{u}$	1.35
$d\bar{d}$	0.35
$\tau^+\tau^-$	0.94
$\mu^+\mu^-$	1.16
e^+e^-	40

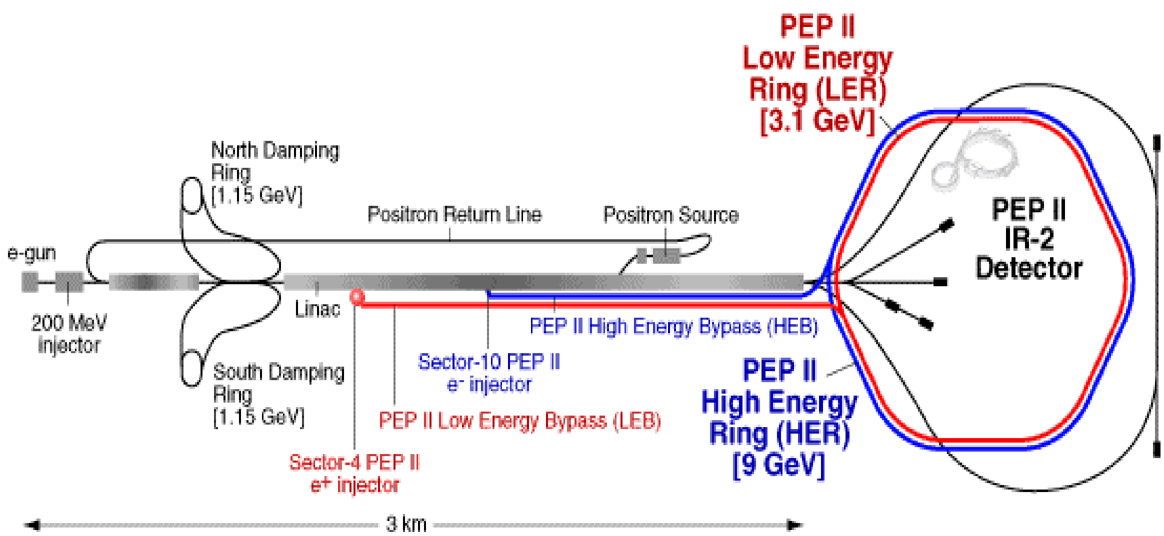

Figure 3.3: A schematic representation of the acceleration and the storage system at the PEP-II.

On reaching the design energies at the end of the Linac, the electron and the positron beams are fed into the PEP-II storage rings, here they collide at the interaction region as shown in figure 3.4. A primary impediment to achieving currents of the required magnitude are beam-beam interference and related beam instabilities. After collision at the interaction point, IP, the beams are separated by the dipole magnet B1, located at ± 21 cm on either side of the IP, the two beams are separated within 62 cm of the IP, thus avoiding spurious collisions between out of phase bunches. To achieve this the B1 magnets had to be located entirely within the *BABAR* detector volume. The strong focusing of the beam is achieved by using an array of quadrupole magnets. The innermost focusing magnet (Q1) is common to both beams and partially enters the detector volume. The support tube of the Q1 magnets run through the center of the detector between the drift chamber and the silicon vertex tracker. Q2 is used to focus only the LER whereas Q4 and Q5 are used only for HER. Both Q1 and B1 are permanent magnets while Q2, Q4 and Q5 are standard iron electro-magnets. The IP is surrounded by a water-cooled Beryllium pipe with an outer radius of 2.8 cm, presenting about 1.08% of a radiation length to particles at normal incidence.

The impressive luminosity of $9.213 \times 10^{33}\,\mathrm{cm}^{-2}\mathrm{s}^{-1}$ was achieved by using a trickle mode (a mode of operation which increases the production of $B\overline{B}$ pairs by upto 50%, with this technique the *BABAR* can keep taking data virtually unintrrupted while the Linac injects the electrons and positrons into the PEP-II storage rings). Within five years of its operation PEP-II has not only achieved its design luminosity but has also surpassed it by about 60%.

The high luminosity of PEP-II has important implications in terms of acceptable background levels for the proper functioning of the detector. Background sources include synchrotron radiation, interactions between the beam and the residual gas in the rings, and electro-magnetic showers produced in the beam-beam collisions. Bremsstrahlung and Coulomb scattering of the beam particles off the residual gas in

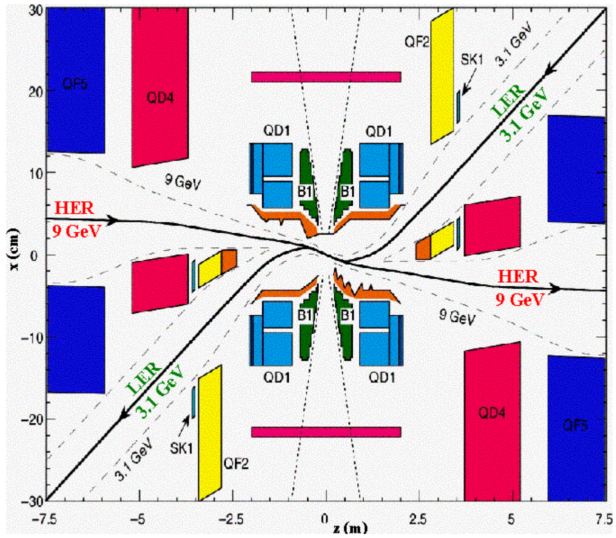

Figure 3.4: A plan view of the interaction region(IR). The vertical scale is exaggerated. The beams collide head-on and are separated magnetically by the B1 dipole magnets. The focusing of the beam is achieved by using the quadrupole magnets, Q1, Q2, Q4 and Q5. The dashed lines indicate the beam stay-clear region and the detector acceptance cutoff at 300 mrad.

the rings dominate the Level 1 trigger rate, the instantaneous silicon vertex detector dose rates, and the total drift chamber current. Energy-degraded beam particles resulting from such interactions are bent by the separation dipole magnets horizontally into the beam pipe, resulting in occupancy peaks for almost all of the *BABAR* sub-detectors in the horizontal plane. The rate of this background is proportional to the product of the beam currents and the gas pressure in the rings. At higher luminosities the background from radiative Bhabha scattering is expected to be crucial.

3.3 The *BABAR* Detector

A layout of the *BABAR* detector is shown in Fig. 3.5 and 3.6.

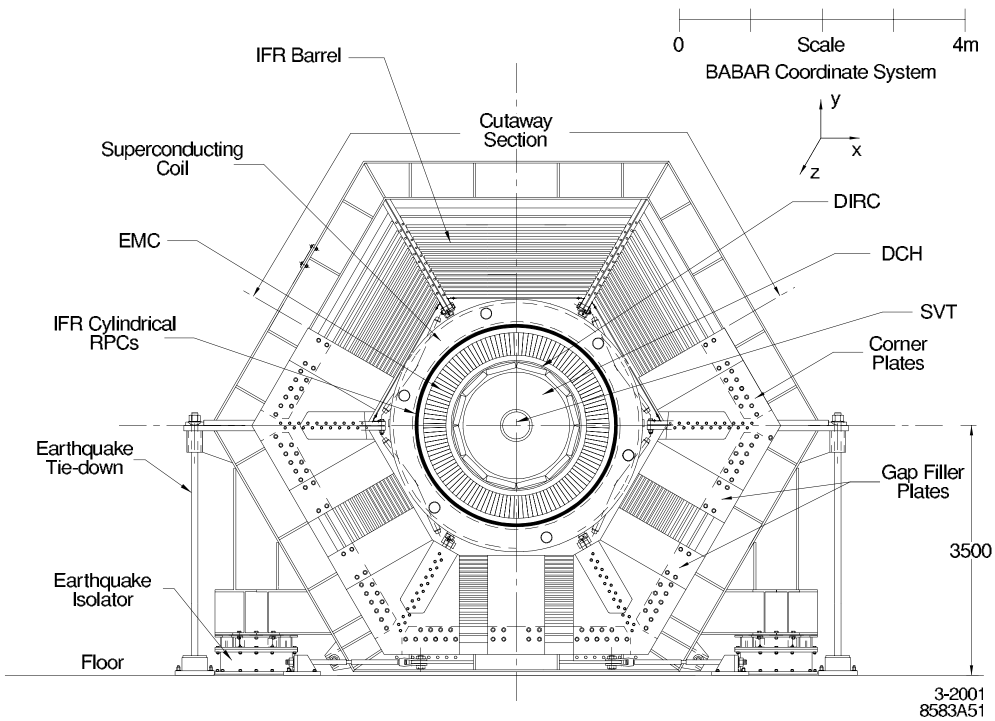

Figure 3.5: *BABAR* detector in cut-away end view.

Trajectories of charged particles are measured in the Silicon Vertex Tracker (SVT) which is surrounded by a cylindrical wire chamber, the Drift Chamber (DCH). A novel Cherenkov detector (DIRC) used for charged particle identification surrounds the drift chamber. The electromagnetic showers of electrons and photons are detected by the CsI crystals of Electromagnetic Calorimeter (EMC) which is located just inside the solenoidal coil of the super-conducting magnet. Muons and hadrons are detected by arrays of resistive plate chambers that are inserted in the gaps of the iron flux return of the magnet (IFR). The detector acceptance is $17^o < \theta_{lab} < 150^o$ in the laboratory frame ($-0.95 < cos\theta_{CM} < 0.87$) where θ is the

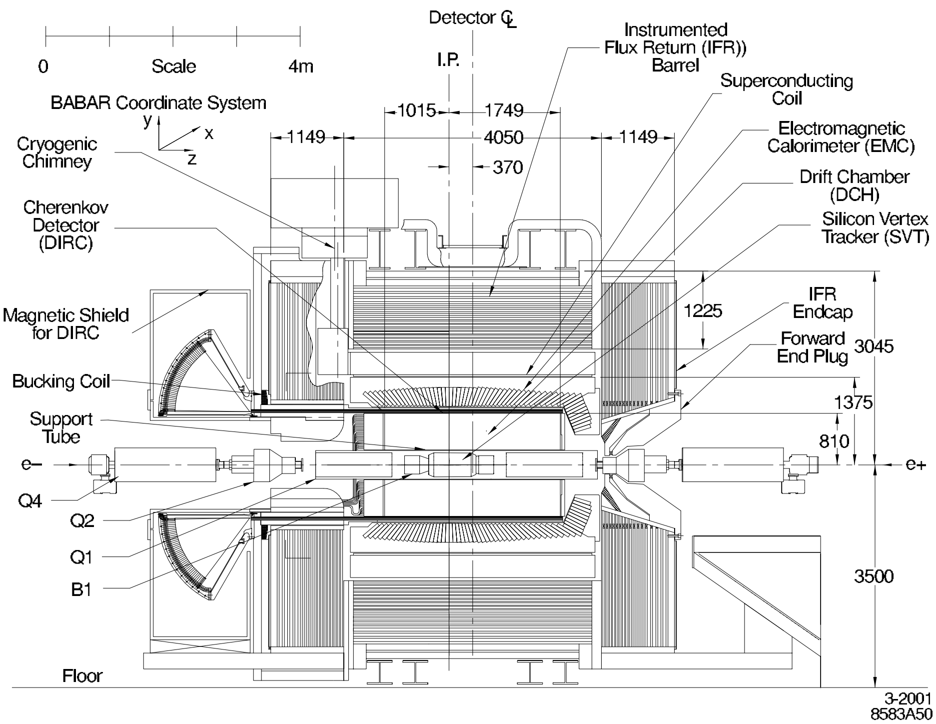

Figure 3.6: *BABAR* detector in longitudinal view.

polar angle. Figure 3.5 shows the *BABAR* detector in cut-away end view, along with a scale and right-handed coordinate system, and Figure 3.6 shows the detector in longitudinal section.

3.3.1 The Silicon Vertex Tracker (SVT)

Charged particle tracks are reconstructed using the SVT and DCH - the SVT is designed to provide angle and position measurements as close as possible to the IP, while the DCH provides momentum measurements. The design of the DCH is discussed in section 3.3.2. The SVT (Figures 3.8 and 3.7) is located radially between the beam-pipe and DCH, and is composed of five layers of double-sided silicon strip detectors. The inner three layers provide most of the information necessary for determination of vertex positions and are mounted as close as possible to the beam-pipe in order to minimize the impact of multiple scattering. The outer two layers are at somewhat larger radii to facilitate linking DCH and SVT tracks, and to make SVT-only momentum measurements for soft tracks which do not reach the DCH. The SVT is designed to provide stand-alone tracking of charged particles with transverse momentum (p_t) less then $\approx 120\ \mathrm{MeV}/c$ which is the minimum p_t required for a reliable DCH momentum measurement. This feature is crucial to the efficient reconstruction of the slow pions used in this analysis. The SVT also provides the good measurements of track angles, which improves the linkage of SVT "+" DCH charged tracks to signals in the DIRC, and provides an independent measurement of dE/dx for use in charged particle identification.

The strips on opposing sides of the double-sided silicon strip detectors are

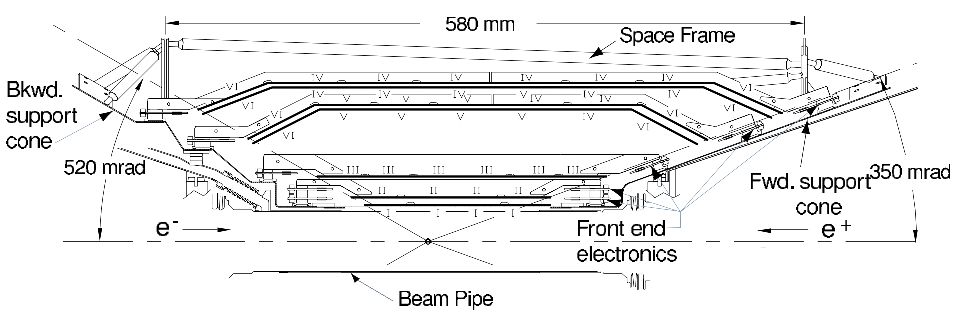

Figure 3.7: Schematic view of the SVT in longitudinal section.

oriented orthogonally to each other: strips which measure the azimuthal angle (ϕ-strips) run along the beam axis and strips which measure z-position (z-strips) are oriented transversely to the beam axis. As can be seen from Figure 3.7, the inner three layers are straight and the outer two layers are arch-shaped, with a straight

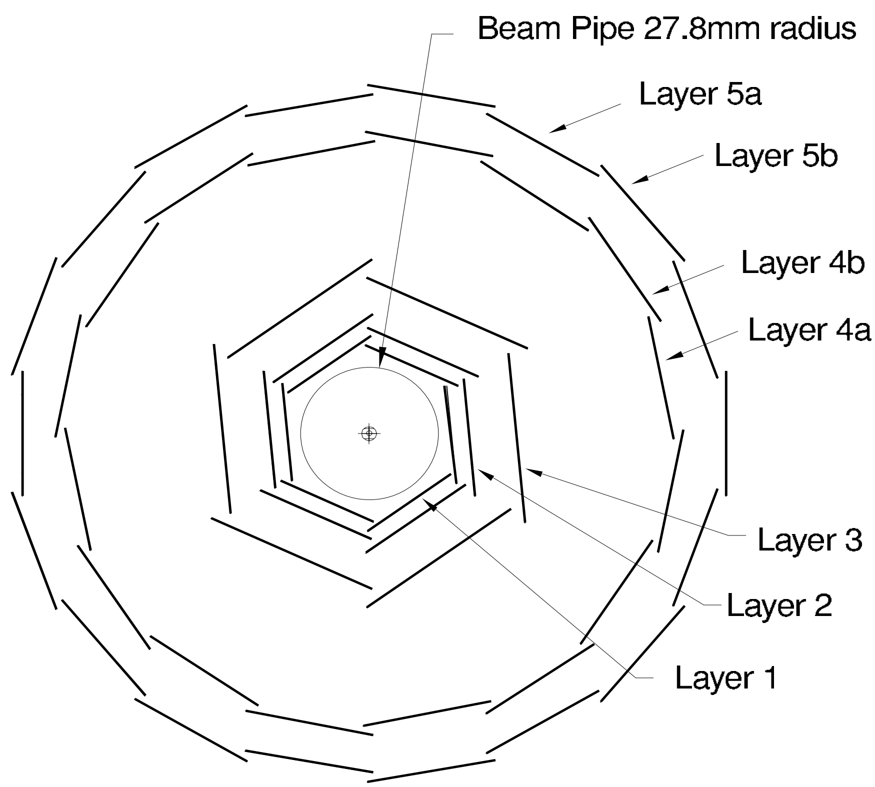

Figure 3.8: Schematic view of the SVT in transverse section.

central section and sections that bend towards the IP both forward and backward ends. This provides polar angle coverage down to 350 mrad in the forward direction and 520 mrad backwards. The SVT single-hit reconstruction efficiency (the probability of associating a z and ϕ hit to a track passing through the active part of the SVT) is $\approx 97\%$.

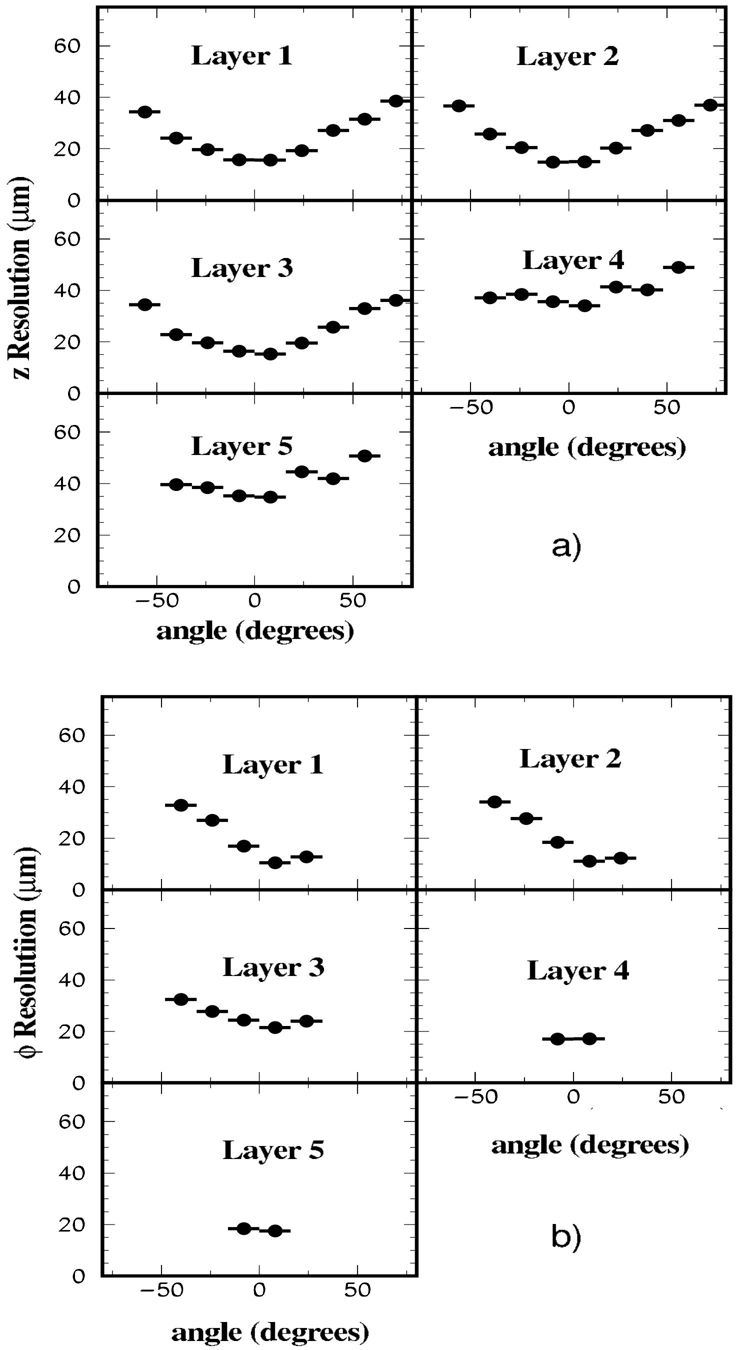

Figure 3.9: SVT hit resolution in z (a) and ϕ (b) coordinate as a function track incident angle. There are fewer points in the ϕ resolution plots for the outer two layers because the range of incident angles subtended is much smaller.

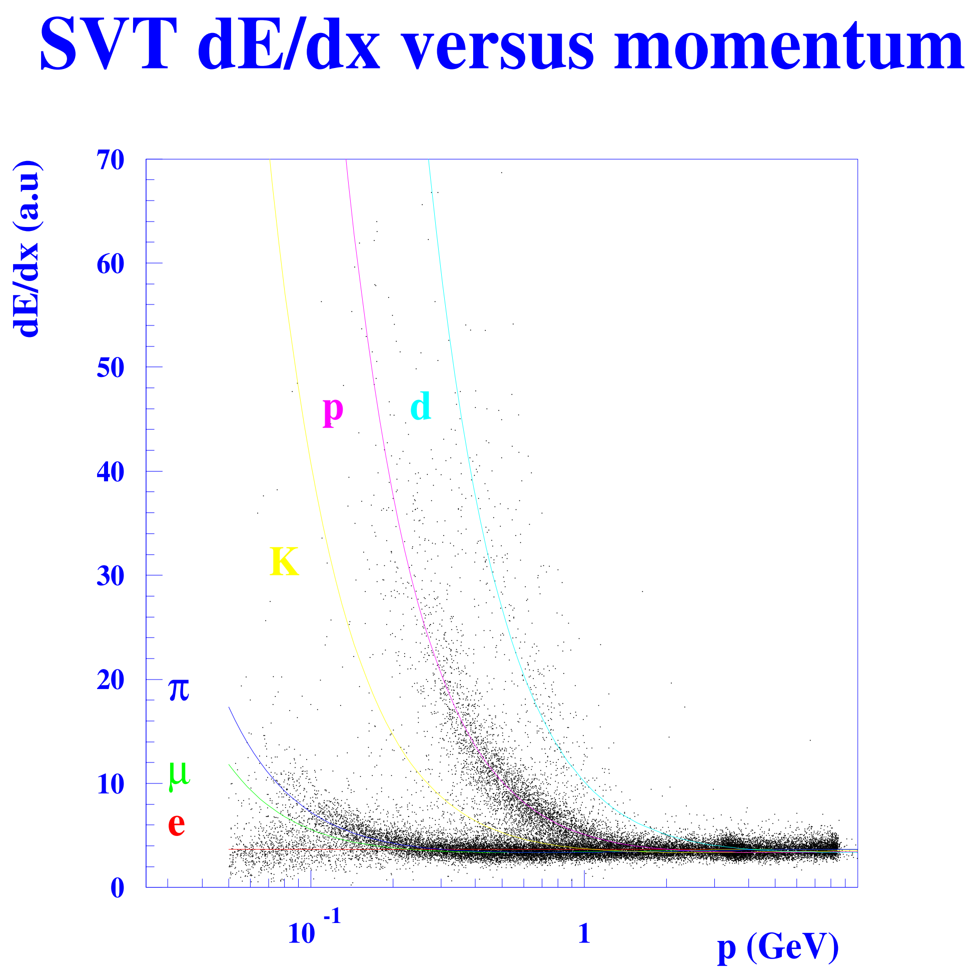

Figure 3.10: Distribution of SVT dE/dx as a function of track momentum.

The overall vertex resolution of the SVT in the xy-plane is set by the need to resolve the vertices of B-meson daughters, which have a typical separation of $\approx 275\ \mu$m in the lab. The SVT was designed to provide a transverse vertex resolution of $\approx 100\ \mu$m perpendicular to the beam line.

Figure 3.9 shows both z and ϕ single-hit resolutions for each of the five SVT layers. The spatial hit resolution for perpendicular tracks is approximately 15 μm (35 μm) for z and 10 μm (20 μm) for ϕ in the inner (outer) layers, which lead to the desired overall vertex resolutions indicated above. Both the hit reconstruction efficiency and spatial resolution are essentially unaffected by the occupancies associated with the highest luminosities and event rates observed by *BABAR* to date.

The five layers of double-sided sensors provide up to ten measurements of dE/dx in the SVT for each charged track. For minimum ionizing particles (MIPs), the dE/dx resolution is $\approx 14\%$ and a two-sigma separation between kaons and pions can be achieved for momenta up to 500 MeV/c and between kaon and proton beyond 1 GeV/c. Figure 3.10 shows SVT dE/dx distributions as a function of both momentum and particle species - the overlaid curves show the Bethe-Bloch prediction of particles for different particle species. The SVT dE/dx information, along with that from the DCH, is combined with DIRC signals to provide charged hadron particle identification.

3.3.2 Drift Chamber (DCH)

The DCH is located radially between the SVT and DIRC (Figure 3.11), and is comprised of 40 radial layers of small hexagonal drift cells which yield spatial and ionization loss measurements for charged particles with p_t larger then ≈ 120 MeV/c. It provides high efficiency precision reconstruction of charged track momentum and supplements the measurement of impact parameter (with respect to the IP), angles and dE/dx provided by the SVT. Longitudinal position information is obtained by placing the wires in 24 of the 40 layers (the "stereo" layers) at slight angles with respect to the z-axis. A 80 - 20 mixture of helium-isobutane and low-Z aluminum field wires minimize multiple scattering with the DCH volume.

The 40 cylindrical layers, with a total of 7,104 drift cells, are grouped into 10

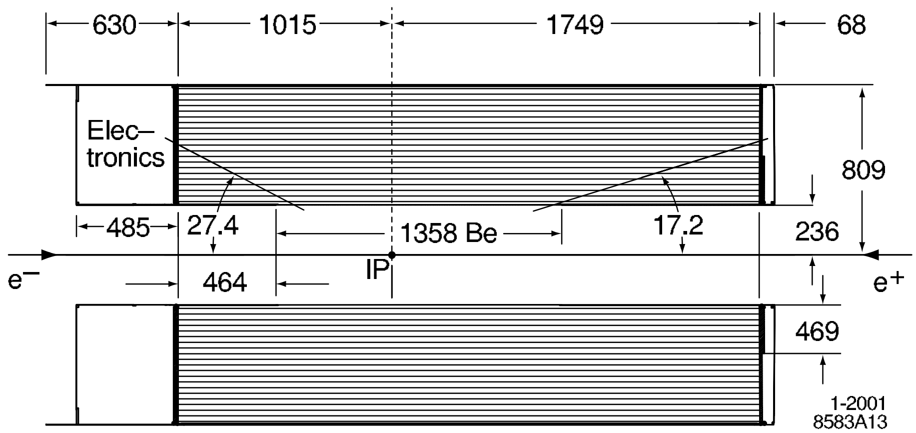

Figure 3.11: Schematic view of the DCH in longitudinal section.

superlayers each consisting of four drift cells. Each cell is approximately 1.2 cm by 1.9 cm along the radial and azimuthal directions, respectively, and consists of one sense wire surrounded by six field-shaping wires. Figure 3.12 shows the arrangement of individual field, sense and guard wires into drift cells in the inner four DCH superlayers. Sense wires are currently operated at a nominal voltage of 1930 V and field-shaping wires at 340 V.

The ionization loss for charged particles traversing the DCH comes from measurements of the total charge deposited in each cell, which are then corrected for effects (such as changes in gas pressure and temperature, differences in cell geometry, etc.) that tend to bias or degrade the accuracy of the measurement. Figure 3.13 shows DCH dE/dx distribution a function of both momentum and particle species - the overlaid curves show the corresponding Bethe-Bloch predictions [29]. Figure 3.14 shows the degree of separation in dE/dx for kaon and pion candidates in a few momentum ranges. The zero of the horizontal axis is the expected dE/dx value

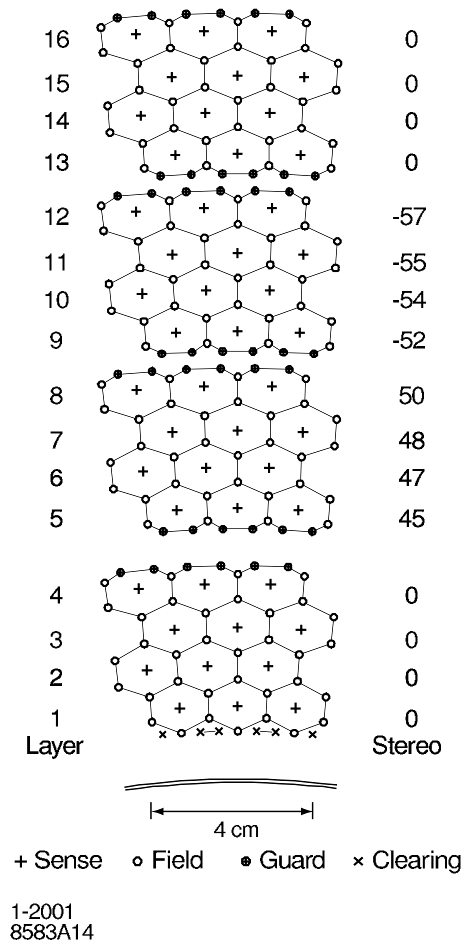

Figure 3.12: Schematic layout of drift cells for the innermost superlayers. Lines have been added between field wires to aid in visualization of the cell boundaries. The numbers on the right side give the stereo angles (mrad) of sense wires in each layer. The DCH inner wall is shown inside of the first layer.

for a kaon averaged over all momenta accessible at *BABAR*. It is clear from this figure that only the relatively soft kaon and pion tracks below ≈ 700 MeV/c (top plot) can to be distinguished by the use of dE/dx alone. Above this threshold, information from the DIRC must be used to differentiate the various charged hadron species.

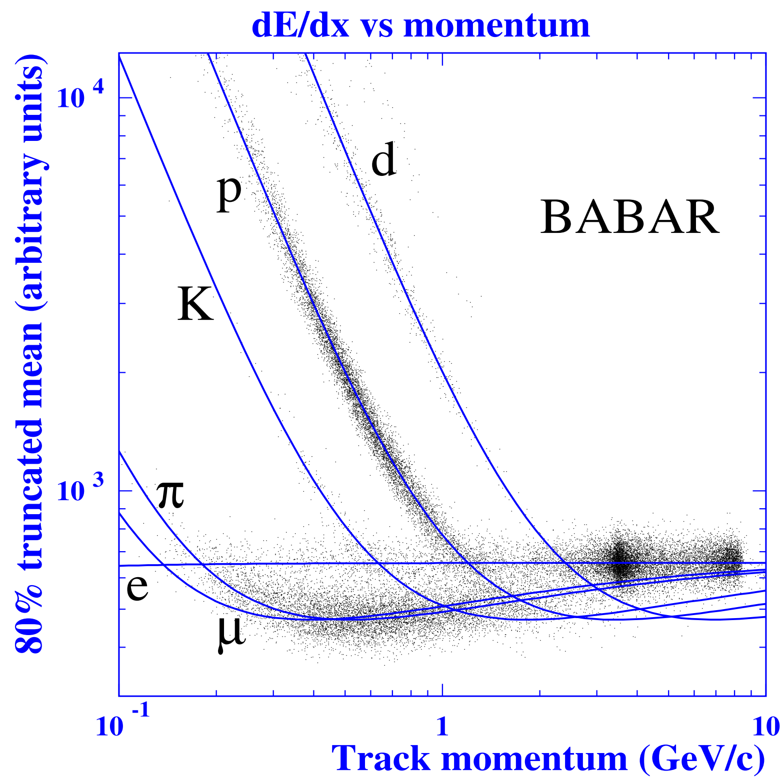

Figure 3.13: Measurement of specific energy loss ionization (dE/dx) in the DCH as a function of track momenta. The data include large samples of beam background triggers, as evident from the high rate of protons. The curves show the Bethe-Bloch corresponding predictions.

3.3.3 Detector of Internally Reflected Cherenkov Light

The DIRC is a unique Cherenkov type detector solely dedicated to charged particle identification (PID). It is designed to provide excellent discrimination of kaons and pions from the turn-on threshold of ≈ 0.7 GeV/c up to ≈ 4.2 GeV/c - below threshold, PID is based upon dE/dx measurements in the SVT and DCH (sections 3.3.1, 3.3.2).

The DIRC is premised upon the detection of Cherenkov photons trapped in a

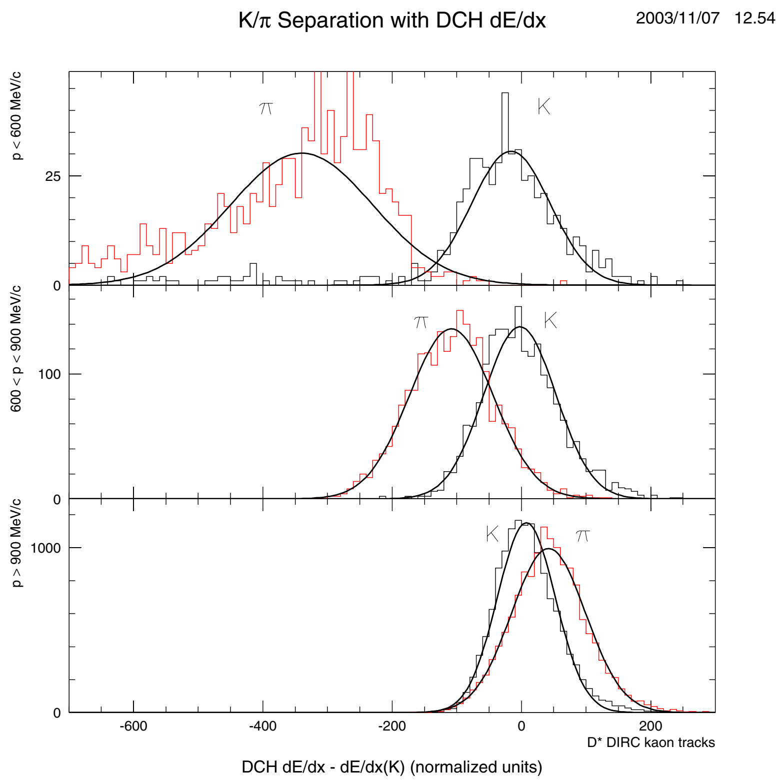

Figure 3.14: Distribution of DCH dE/dx for high-purity kaons and pions obtained from control samples, showing kaon/pion separation in three different momentum regions: $p < 600$ MeV/c (top), $600 < p < 900$ MeV/c (middle), $p > 900$ MeV/c (bottom).

radiator due to total internal reflection. The DIRC radiator consists of 144 long, thin synthetic quartz bars arranged in a 12-sided polygonal barrel. Each bar is 4.9 m long, with a rectangular cross-section of 3.5 cm width in ϕ and 1.7 cm thickness radially. Each quartz bar extends through the steel of the solenoid flux return in the backward direction in order to bring the Cherenkov light, through multiple total internal reflections, outside the tracking and solenoidal volumes where it can be detected by an array of nearly 11,000 photomultiplier tubes (PMTs) arrayed on a roughly toroidal surface about 1.2 m from the bar ends. (Because of the requirement of little material and minimal radius before the EMC, the PMTs must be placed out of the way at the back end of the detector.) Each quartz bar has a mirror, perpendicular to the bar axis, placed at the forward end in order to reflect forward-going photons back toward the instrumented end. Figure 3.15 shows the overall DIRC geometry in longitudinal section.

A schematic of the DIRC geometry to illustrate the principles of light produc-

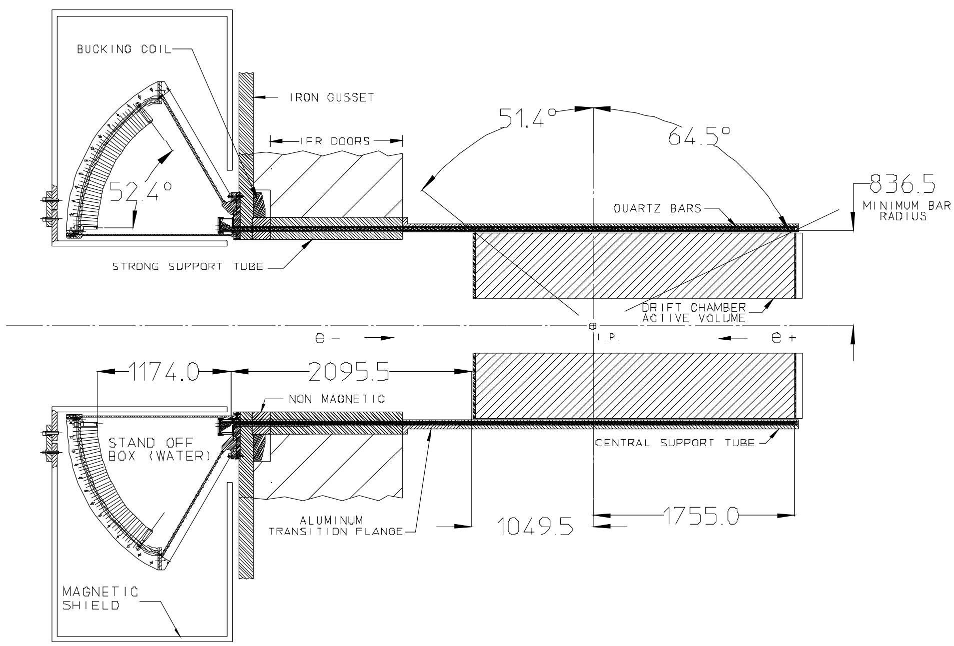

Figure 3.15: Schematic view of DIRC in longitudinal section (all dimensions in mm).

tion, transportation, and imaging is shown in Figure 3.16. A cone of Cherenkov photons is generated as a charged particle passes through a radiator bar, with index of refraction $n = 1.47$, with a Cherenkov angle $cos\theta_c = 1/n\beta$, where $\beta \approx 1$. Given the index of refraction, $n \approx 1$, for the medium (nitrogen) surrounding the quartz radiator in the tracking volume, there will be always some photons within the total

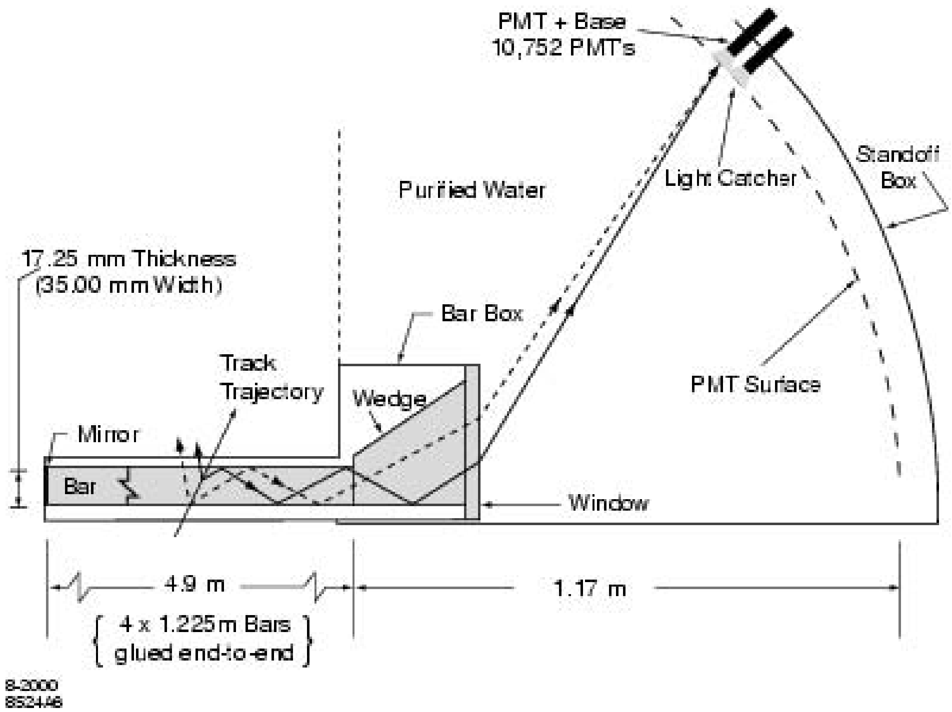

Figure 3.16: Schematic of the DIRC fused silica radiator bar and imaging region.

internal reflection (TIR) limiting angle and, because of the rectangular cross-section of a radiator bar, the magnitude θ_c will be preserved during the successive TIRs (modulo a 16-fold reflection ambiguity of top/bottom, left/right, forward/backward and wedge /no-wedge reflection)†. Therefore, in a perfect bar, the portion of the Cherenkov cone that lies within the TIR angle will be transported without distortion to the end of the bar. A typical DIRC photon has a wavelength $\lambda \approx 400$ nm, undergoes ≈ 200 reflections, and has a 10-60 ns propagation time along a five meter path through the quartz radiator. Cherenkov photons exit a radiator bar and enter

†Timing information and a requirement to use only physically possible photon propagation paths typically reduces the 16-fold reflection ambiguity down to three, which is then further reduced by the use of a pattern-recognition algorithm.

a quartz wedge located at the instrumented end of a bar which efficiently couples the photons into a water-filled expansion region, the so called stand-off box (SOB), which is surrounded by a densely packed PMT array.

The DIRC is a 3-dimensional imaging device which uses the position and arrival times of the PMT signals to reconstruct the Cherenkov angle θ_c, the azimuthal angle of a Cherenkov photon with respect to the track direction ϕ_c and the difference Δt between the measured and expected (using track time-of-flight [TOF] information) photon arrival time. In order to associate the PMT signal with a track traversing a bar, a vector is constructed linking the center of the bar end with the center of the PMT. Since the track position and angles at the DIRC are known from the charged track reconstruction, the photon propagation angles $\alpha_{x,y,z}$ can be calculated and used to determine θ_c and ϕ_c. The timing of the PMT signal relative to the track is useful in suppressing photon backgrounds from PEP-II and, more importantly, exclude other charged tracks in an event as a possible photon source.

The number of Cherenkov photons per track varies from $\approx$ 20-50, with the smaller number generally occurring in the central region of the detector (corresponding to a shorter path length in the quartz radiator) and increasing as the track dip angle increases (corresponding to longer path lengths in the quartz radiator). Figure 3.17 shows the distribution of the number of signal photons for single muons taken from both simulated and actual di-muon events as a function of polar angle - the excess near $cos(\theta_{track}) = 0$ is due to the existence of both forward- and backward-going Cherenkov photons for tracks which traverse a quartz radiator bar at near-normal incidence.

Figures 3.18 and 3.19 show the reconstructed Cherenkov angle θ_c for control sam-

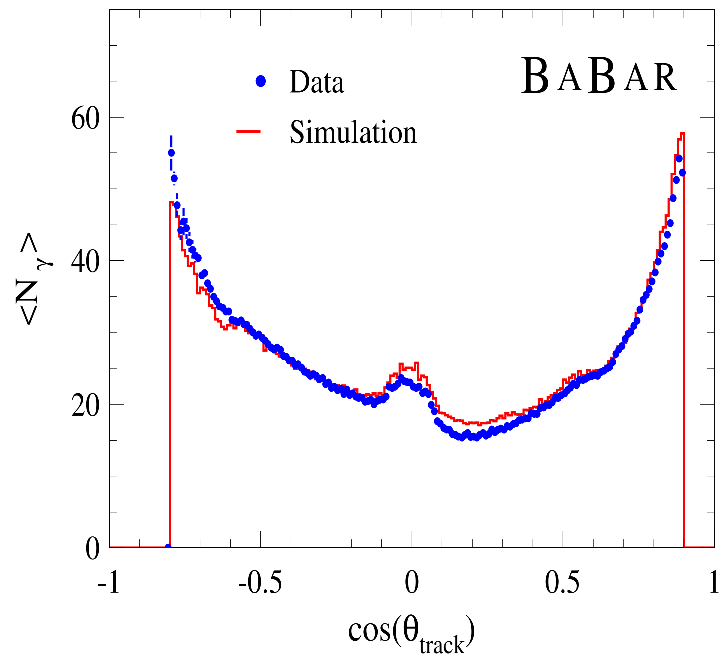

Figure 3.17: Number of signal photons per track for single muons taken from di-muon event plotted as a function of $cos(\theta_{track})$.

ples of charged kaons and pions, respectively, as a function of momentum. Based on the θ_c distributions for control samples as illustrated in these two figures, Figure 3.20 shows the kaon/pion separation power of the DIRC as a function of momentum. As the figure demonstrates, even at the highest lab momenta accessible at *BABAR*, the DIRC provides nearly 3σ separation of kaons and pions. It is also important to note that, in addition to good separation of kaons and pions, the DIRC is also highly efficient. The top plot of Figure 3.21 shows that the efficiency to reconstruct kaons with the DIRC is generally well above 90% - this plot also demonstrates that the DIRC efficiency rises fairly quickly to its maximum value above the DIRC turn-on threshold of $p > 0.7$ GeV/c.

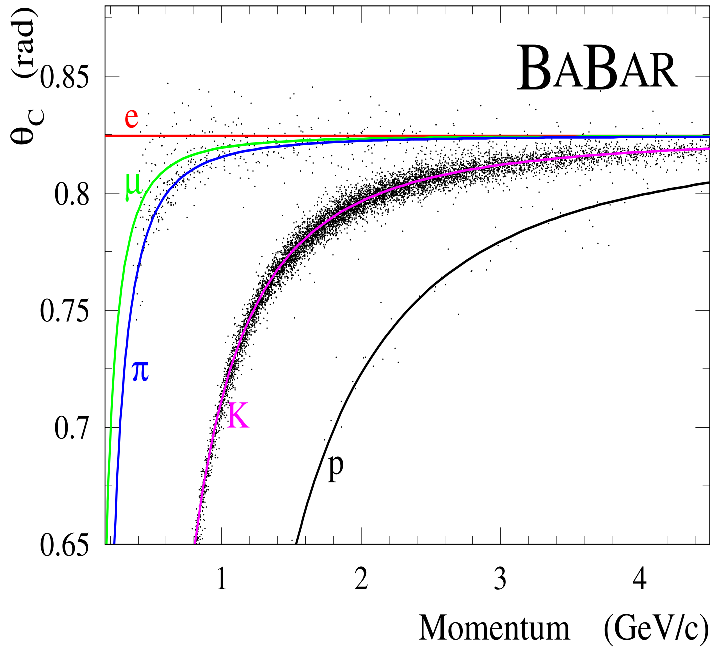

Figure 3.18: Charged kaon Cherenkov angle as a function of momentum-the data points lying off the "K" curve are due to impurities in the control sample of charged kaons used to make the plot.

3.3.4 Electromagnetic Calorimeter (EMC)

The electromagnetic calorimeter of *BABAR* is designed to measure the energy in the electromagnetic showers with excellent efficiency, energy and angular resolution over the energy range of 20 MeV to 9 GeV. This capability allows for reconstruction of π^0 and η mesons and for separation of photons, electrons and positrons from charged hadrons.

The EMC as shown in Figure 3.22, consists of a cylindrical barrel and a conical forward end-cap, extending from $\approx 16° - 142°$ in polar angle, which corresponds

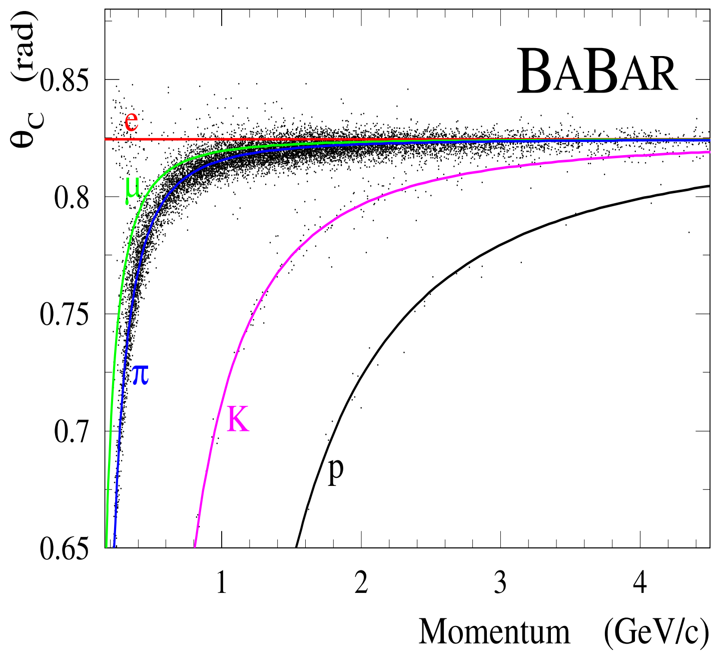

Figure 3.19: Charged pion Cherenkov angle as a function of momentum-the data points lying off the "π" curve are due to impurities in the control sample of charged pions used to make the plot.

to about 90% geometrical coverage in the CM system. The barrel which consists of 5,760 CsI(Th) crystals arranged in 48 azimuthal rings, with the endcap having 820 crystals arranged in eight rings. Each ring of crystals is oriented such that the normal to a crystal face points toward the origin of the *BABAR* coordinate system. The crystals have a tapered trapezoidal cross-section, typically 4.7×4.7 cm^2 at the front face and 6.1×6.0 cm^2 at the back face. The length of the crystal runs from 29.6 cm in the most backward rings to 32.4 cm in the most forward rings in order to limit the effects of shower leakage from the more highly energetic forward-going particles. Because the EMC lies within the solenoid, the photon detector for each

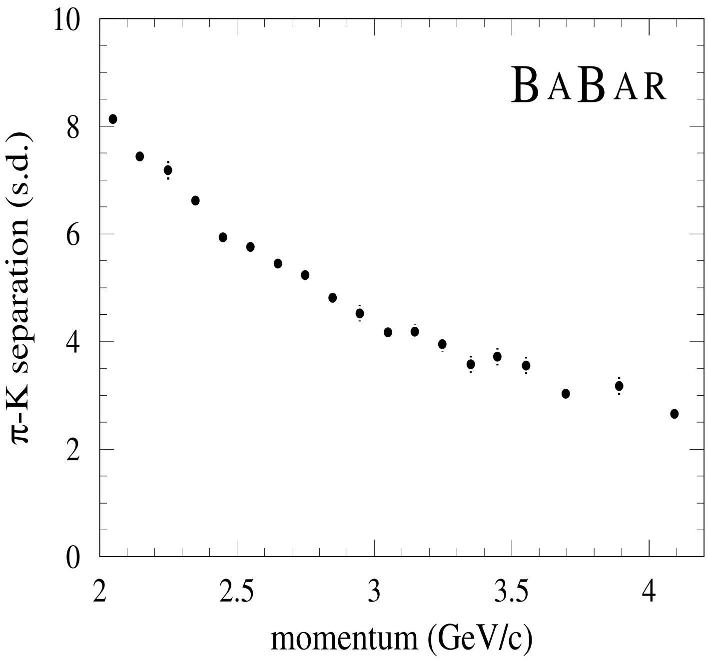

Figure 3.20: Kaon/pion separation using θ_c - the vertical axis gives the separation in units of θ_c standard deviation.

crystal consists of two 2×1 cm^2 silicon pin diodes mounted directly on the back face of each crystal and each of the doides is connected to a low-noise preamplifier board mounted directly behind each crystal.

An electromagnetic shower typically spreads over several crystals, forming a *cluster* of energy deposits. The definition of a cluster requires that at least one crystal registers an energy above 10 MeV. Contiguous neighbors (including corners) of a crystal with at least 3 MeV are considered part of the cluster, as are surrounding crystals with energy above 1 MeV. Pattern recognition algorithms have been developed to efficiently recognize clusters and differentiate merged clusters with more than one energy maximum, called *bump*. This bump is recognized as a γ by assig-

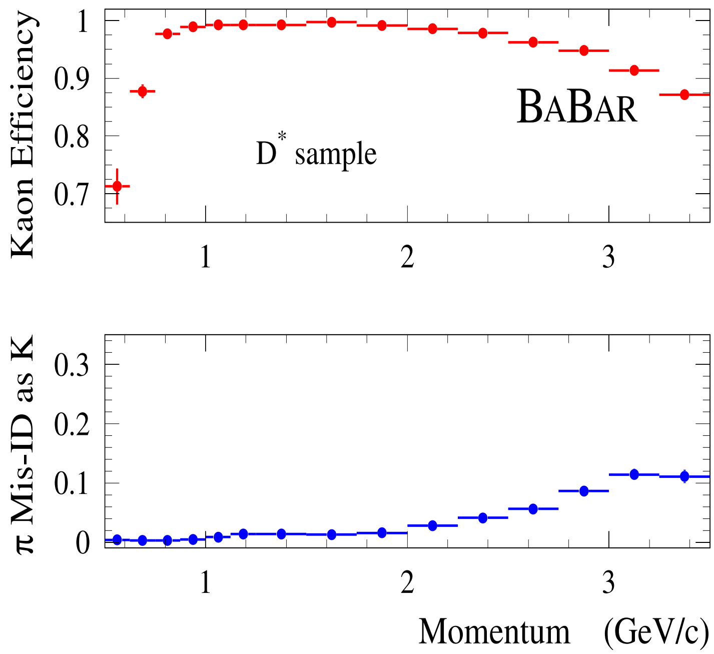

Figure 3.21: Kaon reconstruction efficiency in DIRC (top); probability to misidentify a pion as a kaon based on θ_c (bottom).

nig a photon mass hypothesis. To determine whether a bump is associated with a charged particle, the track is projected to the inner face of the EMC. The distance between the bump centroid and the track impact point is calculated, and if it is consistent with the angle and momentum of the track, the bump is associated with the charged particle. Otherwise, the bump is assumed to come from a neutral particle.

Several different source are used to determine the energy resolution of the EMC. At low energies, it is measured directly using radioactive sources. At high energies the energy resolution is measured from the Bhabha scattering and is parameterized

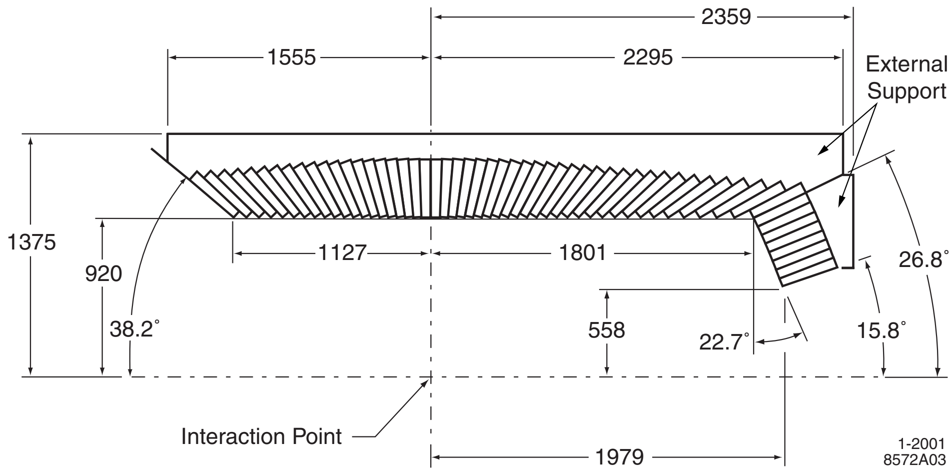

Figure 3.22: A longitudinal cross-section of the EMC (only top half is shown) indicating the arrangement of the 56 crystal rings. The Detector is axially symmetric around the z-axis. All dimensions are given in mm.

as:

$$\frac{\sigma E}{E} = \frac{(2.32 \pm 0.30)\%}{E(\text{ GeV })^{\frac{1}{4}}} \oplus (1.85 \pm 0.12)\%$$

where E is the photon energy in GeV. At lower energy the resolution is dominated by fluctuations in photon statistics and by beam-generated backgrounds, and at energies larger than 1 GeV by the non-uniformity in light collection from leakage or absorption in the material between or in front of the crystals. The reconstructed π^0 has width of 6.9 MeV/c^2. The mass resolution is dominated by the energy resolution at lower energy (below 2 GeV). At higher energies, the mass resolution is dominated by the angular resolution. The latter is determined primarily by the transverse crystal size. The angular resolution can be found from the analyses of π^0 and η decays. The angular resolution can be parameterized as:

$$\sigma_\theta = \frac{(3.87 \pm 0.07)}{\sqrt{(E(\text{ GeV }))}} \oplus (0.00 \pm 0.04) \text{ mrad}$$

3.3.5 Instrumented Flux Return (IFR)

The IFR, shown in Figure 3.23, is the outermost and largest of the *BABAR* subdetectors. It consists of three parts: barrel and the forward and backward endcaps. All of them are subdivided into sextants. The active detectors are 806 Resistive Plate Chambers (RPC), located in the gaps between the layers of steel. There are 19 RPC layers in the barrel, and 18 layers in the endcaps. Additionally, there are two layers of cylindrical RPCs between the EMC and the magnet. The thickness of the steel layers ranges from 2 cm in the inner 9 layers to 10 cm in the outermost layers. RPCs are gas chambers enclosed between bakelite (which is a phenolic polymer) plates. In both the planer the cylindrical RPCs, the gap between the Bakelite sheets is 2 mm, and the sheets themselves are 2 mm thick. One of the plates is kept at approximately 8 kV, and the other is grounded, so that an ionizing particle crossing the gas gap will produce a quenched discharge. The gas used is a mixture of 56.7% Argon, 38.8% Freon-134a, and 4.5% Isobutane.

The IFR is efficient at detecting particles with $p_t > 0.4$ GeV/c. In order to penetrate completely through the detector, a particle must have $p_t > 0.7$ GeV/c. The majority of the tracks entering the IFR are muons, though pions may punch through the calorimeter and fake muon signals (A muon detection efficiency of close to 90% has been achieved in the momentum range of $1.5 < p < 3.0$ GeV/c with a fake rate of pions of about 6 - 8%. Decays in flight contribute about 2% to the pion misidentification probability). These inefficiencies are mainly due to the degradation over time of the detector components.

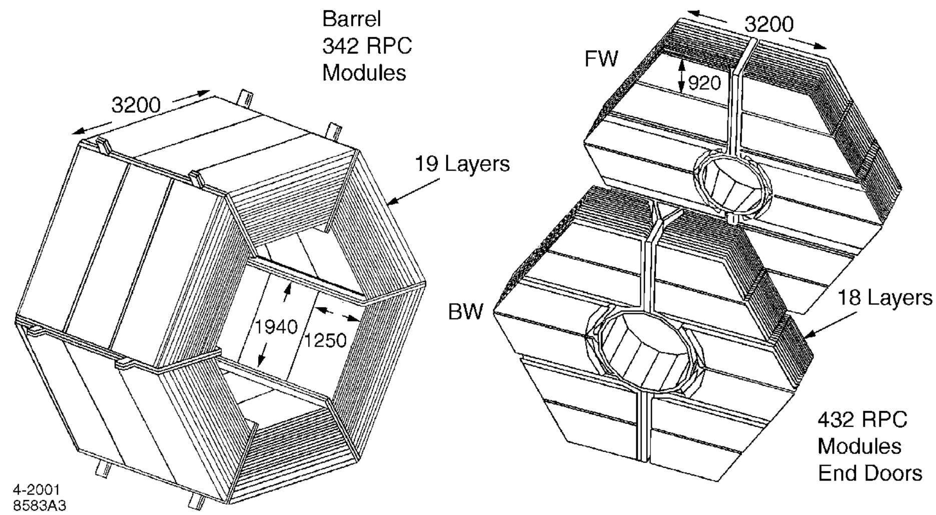

Figure 3.23: Overview of the IFR: Barrel sectors and forward (FW) and backward (BW) end doors; the shape of the RPC modules and their dimensions are indicated.

3.3.6 Trigger (TRG)

The trigger system's primary requirement is to select events for physics studies, for use in either analysis, diagnostic, or calibration studies. The current *BABAR* trigger configuration consists of two levels: Level 1 trigger (L1) and Level3 trigger (L3). The missing Level 2 trigger may be implemented in the future if the load on the trigger system warrants it. Each level has two main independent components, one based on the DCH and one on the EMC. L1 also has a component based on the IFR, mainly to select cosmic ray muons for calibration and diagnostics.

Raw information is used by L1 to form rough tracks and energy clusters. If an event has several tracks in the DCH, especially tracks that are back-to-back, or several clusters in the EMC, it will pass L1. Additionally, if clusters are found in the same azimuthal region as tracks, an event is more likely to pass. Cuts are very loose in L1, resulting in an efficiency greater than 90% for physics events ($> 99\%$ for hadronic events). Typical event rates out of L1 are $\sim$ 1 - 2 kHz, with a latency of about 12 μs.

L3 takes information from L1 and performs higher quality track finding, track fitting, and clustering. Better information regarding the timing and the z positions of hits and clusters allows discrimination against out-of-time noise and beam background tracks. One high p_t track or two low p_t tracks originating from the interaction point are required for the DCH trigger. For the EMC trigger, either a large number of clusters or a large amount of deposited energy throughout the detector is required for acceptance. The average event processing time in L3 is 8.5 ms . The final output of the trigger system is roughly $\sim$ 200 Hz, the efficiency for selecting events for analysis varies from 90% for $\tau^+\tau^-$ events to 99% for $B\overline{B}$ events.

Chapter 4

Charged Particle Tracking and Particle Identification

4.1 Charged Particle Tracking

A charged particle travels in a helical trajectory through a magnetic field. The method for determining the helix parameters and their resolution are discussed in this section.

4.1.1 Track Selection

The tracks are defined by five helix parameters:

- z_0 : the distance from the origin to the point of closest approach along the z-axis.

- d_0 : the distance from the origin to the point of closest approach in the xy-plane.

- ϕ_0 : the azimuthal angle of the track at the point of closest approach.
- λ : the dip angle relative to the transverse plane at the point of closest approach.
- $\omega = \frac{1}{p_t}$: the signed curvature of the helix.

The distance from the origin to the point of closest approach z_0 and ω are variables whose sign depends on the charge of the track. The track finding and fitting procedures use a Kalman fitting algorithm [30] which takes into account the detailed distribution of the material and the magnetic field in the detector. Charged particle tracking has been studied on a wide range of different events: cosmic ray muons, $e^+e^- \rightarrow (e^+e^-, \mu^+\mu^-, \tau^+\tau^-$, and multi-hadron) events.

The reconstruction routine utilizes information provided by the L3 trigger and the tracking algorithm. First it improves the estimate of the event start time, t_0, from a fit to the parameters d_0, ϕ_0, and t_0 based on four-hit track segments found in the DCH super-layers. Tracks are then selected by performing helix fits to the track segments found by the L3 track finding algorithm. Further hits in the DCH that might belong to the track are sought. By using only hits associated with tracks t_0 is further improved.

Two more track procedures are applied to find tracks that either do not pass through the entire DCH or do not originate from the interaction point (IP). These procedures primarily use track segments that have not already been associated with another track. At each iteration, the start time t_0 is improved by the increasingly cleaner tracking environment. At the end of this procedure, all tracks are refit with the Kalman filter.

The tracks found in the DCH are then extrapolated into the SVT. Tracks segments in the SVT are added to a candidate track, accounting for possible multiple scattering in the intervening material and for changes in the magnetic field. Of the SVT track segments, the ones with the smallest hit residuals and the largest number of SVT layers hit are retained, and the Kalman fit is performed on the combined SVT "+" DCH hits.

After the first pass of the combined SVT "+" DCH track finding and fitting, any remaining SVT hits which have not been assigned to a track are analyzed by two supplementary, standalone track finding algorithms. The first one uses matched ϕ and z space points from SVT layers 1, 3, and 5, and any consistent space points from the other two layers. A good track requires a minimum of four space points. This algorithm is efficient on a wide range of d_0 and z_0 values. The second algorithm starts with circular trajectories from ϕ hits and then adds z hits to form helices.

Finally, an attempt is made to combine tracks found by only one of the two tracking systems, and thus to recover tracks scattered in the material between the two detectors.

4.1.2 Track Efficiency

The efficiency for reconstructing tracks in the DCH has been measured as a function of transverse momentum, polar and azimuthal angles, and track multiplicity for multi-track events. These measurements rely on certain final states and exploit the fact that the track reconstruction can be performed independently in the SVT and DCH.

The absolute tracking efficiency in the DCH is determined by the ratio of the number of tracks reconstructed in the DCH to the number of tracks detected in the SVT, provided they fall within the acceptance of the DCH [26]. The track reconstruction efficiency for tracks with both SVT and DCH hits is shown in Figure 4.1 as a function of transverse momentum, polar angle and sense wire operating voltage. There are generally very high efficiencies at all momenta and polar angle (at the design voltage of 1960 V, the efficiency is about $98 \pm 1\%$ per track above 200 MeV/c and for polar angle value $\theta > 500$ mrad). But the efficiency is reduced by $\sim 5\%$ when the sense wire voltage is reduced to 1900 V from 1960 V. There have been significant *BABAR* running periods when the DCH was run at 1900 V for operational reasons, and the DCH is currently being run at 1930 V, but the slight varying efficiency in this analysis is not included as a systematic uncertainty.

After the initial fitting procedure attempts are made to any remaining unassociated SVT hits as low p_t tracks which lacked enough transverse momentum to enter the DCH. As shown in Figure 4.2, charged tracks with p_t as low as ≈ 50 MeV/c are able to be reconstructed with at least 80% efficiency. As with data taken with the DCH voltage 1900 V, the varying efficiency of low p_t tracks is not a factor in this analysis and is not included as a systematic uncertainty.

4.1.3 Track Parameter Resolution

The resolution of the track parameters is studied using cosmic ray muons which pass near the beam interaction point. Because the tracking system is designed for tracks originating at the IP, the cosmic ray track transversing SVT and DCH are split into two segments, one in each of the upper and lower halves of the detector, which are fitted as two separate tracks. To assure that the tracks pass close to the IP, cuts are

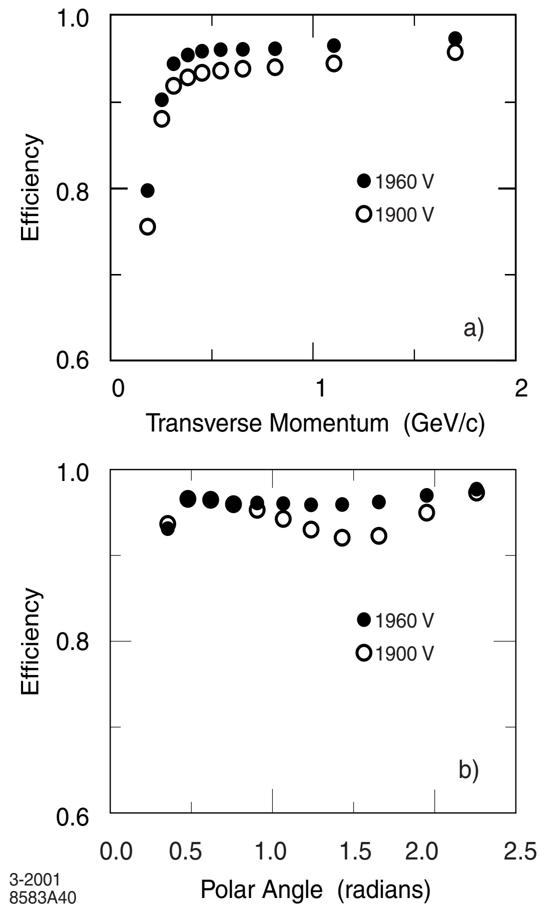

Figure 4.1: Charged track reconstruction efficiency in the DCH at operating voltages of 1900V (open points) and 1960V (filled points) as a function of transverse momentum (top) and polar angle (bottom). The efficiency is measured in multi-hadron events as the fraction of all tracks detected in the SVT for which the DCH track segment is also reconstructed.

applied on the z_0, d_0, and $tan\lambda$. The resolution is derived from the difference of the measured parameters for the two track halves. The results can be seen in Figure 4.3. Based on the full width at half maximum of these distributions the resolutions for single tracks can be stated as:

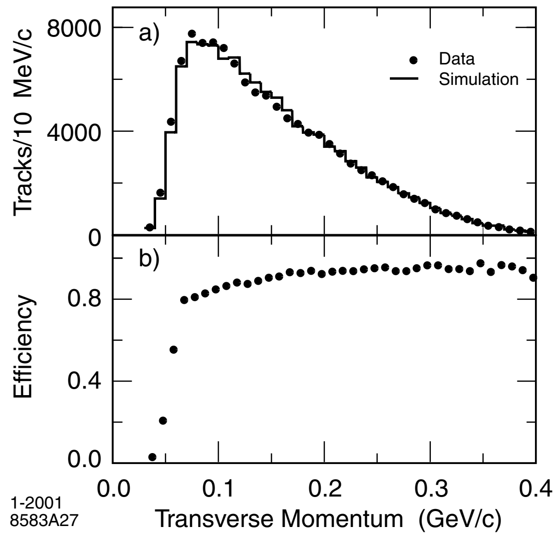

Figure 4.2: (a) Transverse momentum spectrum of soft pions from data (points) and from simulated (histogram) of $D^{*+} \to \pi^+ D^0$ decays in $b\bar{b}$ events; (b) efficiency for soft pion detection taken from simulated events.

$$\sigma_{d_0} = 23\ \mu\text{m} \qquad \sigma_{\phi_0} = 0.43\ \text{mrad}$$

$$\sigma_{z_0} = 29\ \mu\text{m} \qquad \sigma_{tan\lambda} = 0.53 \times 10^{-3}$$

The transverse momentum dependence of the parameters z_0 and d_0 has been measured using multi-hadron events. The resolution is determined from the width of the distribution of the difference between the measured parameters and the coordinates of the vertex reconstructed from the remaining tracks in the event. A plot of the distribution is shown in Figure 4.4.

Measurements of the position and angle near the IP are dominated by the SVT measurements. The DCH contributes primarily to the p_t measurement. The resolution of p_t can be parameterized by the linear function,

$$\sigma_{p_t}/p_t = (0.13 \pm 0.01)\% \times p_t + (0.45 \pm 0.03)\%,$$

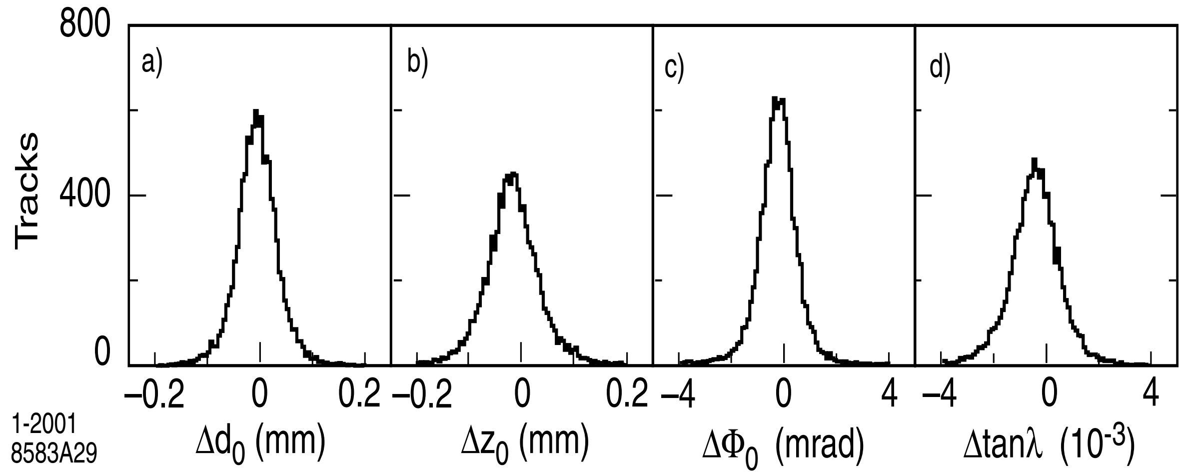

Figure 4.3: Track parameter resolutions based on the differences between the two halves of cosmic ray muon tracks with momenta above 3 GeV/c.

where the p_t is measured in GeV/c.

4.1.4 Tracking Lists

The reconstructed data for physics analysis are candidate lists of charged tracks, neutral particles as energy deposits in the EMC, etc. We use these candidates to reconstruct our final decay products, Λ_c daughter particles. The track lists are provided by the offline prompt reconstruction (OPR) as below:

Charged Tracks

Several charged track lists are defined for analysis purposes, including:

1. `ChargedTracks`:

   Candidates with non-zero charge, with the pion mass hypothesis.

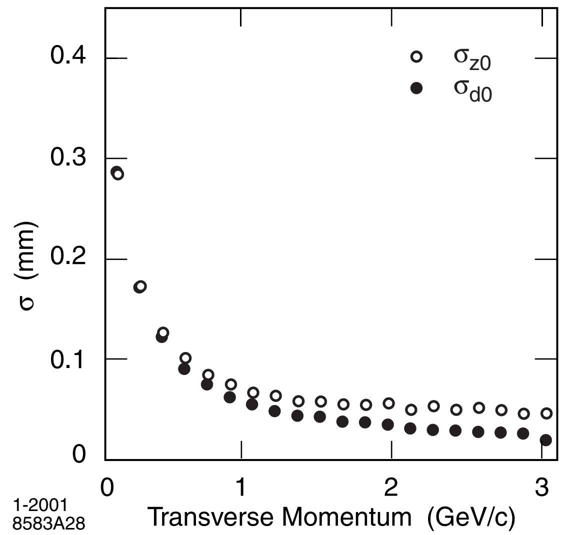

Figure 4.4: Resolution of track parameters d_0 and z_0 as a function of transverse momentum, measured in multi-hadron events. The data are corrected for the effects of particle decays and vertexing errors. The error bars are smaller than the points shown.

2. `GoodTracksVeryLoose`:

   Subset of `ChargedTracks` with additional requirements:

   * $0 < p_t < 10\,\mathrm{GeV}/c$;
   * $\mathrm{DOCA}_{xy} < 1.5$ cm*;
   * $\mathrm{DOCA}_z < 10$ cm.

3. GoodTracksLoose:

   Subset of `GoodTracksVeryLoose` with:

   * $p_t > 0.1$ GeV/c;
   * DCH Hits ≥ 12.

*DOCA: Distance of closest approach of a track to the beam spot center

4. `GoodTracksAccLoose`:

   Subset of `GoodTracksLoose` with:

   * $0.410 < \theta < 2.54$ rad.

5. GoodTracksTight:

   Subset of `GoodTracksLoose` with additional cuts:

   * DCH Hits ≥ 20.

   * $\mathrm{DOCA}_{xy} < 1$ cm.

   * $|DOCA_z| < 3$ cm.

We use the `ChargedTrack` and `GoodTracksVeryLoose` lists for our analysis.

Neutral Particles

Similar to charged tracks, the neutral particles are reconstructed from the EMC are organized in several lists:

- `CalorNeutral`:

  Candidates which are single EMC bumps not matched with any track. Photon mass hypothesis assigned.

- `CalorClusterNeutral`:

  Candidates that are multi-bump neutral clusters or single bumps which are not part of a cluster which is matched with a track.

- `GoodNeutralLooseAcc`:

  Subset of `CalorNeutral` with additional requirements:

  * $E > 30$ MeV;

- ∗ Lateral Moment ≤ 1.1;
- ∗ $0.410 < \theta < 2.409$.

- `GoodPhotonLoose`:

  Subset of `CalorNeutral` with additional requirements:

  - ∗ $E > 30$ MeV;
  - ∗ Lateral Moment ≤ 0.8.

- `GoodPhotonDefault`:

  Subset of `GoodPhotonLoose` with:

  - ∗ $E_\gamma > 100$ MeV;

We use the `GoodPhotonLoose` list for photons in our analysis.

4.1.5 Particle Identification

Only five types of charged tracks are sufficiently long-lived to leave a track in the *BABAR* detector: electrons, muons, pions, kaons, and protons. All other charged particles, except the charged hyprons, decay before reaching the first SVT layer (which has 32 mm radius in both ϕ and z). Due to the dominant number of pions in multi-hadron events, for the general reconstruction, all tracks are assumed to be a pion in the initial tracking fits, and the pion mass is used in defining the 4-momentum of the track. Studies have been done to show that this assumption has a negligible effect except in low momentum particles [31], and it is easy to correct for a different particle hypothesis in the later analysis if another choice is needed. Specialized algorithms have been developed by *BABAR* which are used to identify kaons and protons. Whenever the particle ID is used to select a track, the mass hypothesis used for that track is changed to that of the selected particle.

Proton Identification

Proton selection used in this analysis is based on likelihood selector. The likelihoods are calculated for each of the five sub-detectors: SVT, DCH, DIRC, EMC, and IFR. Each sub-detector is assigned a liklihood (LH) for each of the five possible hypotheses (P, K, π, μ, e). A sub-detector's set of likelihoods is re-scaled such that the most likely hypothesis is given a likelihood of unity. After normalization, any likelihood below a minimum value, the floor value, is set to the floor value. The floor value is assigned per detector, and it acts to limit a detector's ability to discriminate too strongly against a hypothesis. In essence, the floor value does two things: it protects against detector malfunctions that might give unreasonably small likelihoods for any hypotheses, and it adds tails to the idealized likelihood functions used to calculate the likelihoods. The five likelihoods for sub-detectors d for a given hypothesis h are multiplied together, along with an *a priori* (already known-able independently of experiment) likelihood for each hypothesis:

$$\mathcal{L}(h) = \mathcal{L}^{apriori}(h) \times \prod_{d=SVT}^{IFR} max(\mathcal{L}^{floor}(d), \mathcal{L}^{opr}(d,h))$$

In case of charged hadrons selection, the most sensitive part of the detectors for the likelihood calculations are: SVT, DCH, and DIRC. The LH for the SVT is calculated from an asymmetric Gaussian function of the logarithm of dE/dx:

$$\exp^{(}\frac{(ln(dE/dx_{meas}) - ln(dE/dx_{th}))^2}{2\sigma\sqrt{5/N}})$$

with $\sigma = \sigma_L$ for $dE/dx_{meas} < dE/dx_{th}$ and $\sigma = \sigma_R$ for $dE/dx_{meas} > dE/dx_{th}$. The left-side and right-side standard deviations of the asymmetric Gaussian are fixed parameters. These standard deviations are calculated for five measured dE/dx samples, and they are inflated slightly for tracks with fewer samples to account for a wider spread in the truncated mean. N is the number of SVT layers.

A minimum of three out of the five SVT layers are required to provide dE/dx information; otherwise, the SVT is not calculated. In order to mitigate the effects of Landau fluctuations, only the smallest 60% of the dE/dx values are used to calculate the mean dE/dx for a track. For five samples, the lowest 3 values are used for the average; in case of four samples the 3rd lowest value is given a weight of 40% when averaged with the lowest two values. The expected dE/dx is found from a five-parameter Bethe-Bloch equation, using the momentum of the fit to the considered hypothesis:

$$\frac{dE}{dx} = 4\pi r_e^2 m_e c^2 N_A \frac{Z}{A}\frac{1}{\beta^2}\left[\frac{1}{2}ln\left(\frac{2m_e c^2\gamma^2\beta^2 T_{max}}{I^2} - \frac{\delta}{2}\right)\right]$$

where x is a density-corrected length with units g/cm^2, r_e and m_e are electron's classical radius and mass, c is the speed of light, N_A is Avogadro's number, Z is the charge of incoming particle, A is the atomic number of the absorber, β and γ are the relativistic quantities of the incoming particle, I is the mean excitation energy, and δ is density effect correction. T_{max} is maximum transition kinetic energy.

The DCH likelihood for a particle is calculated using a symmetric Gaussian function of the mean measured dE/dx:

$$\exp\left(\frac{(dE/dx_{meas} - dE/dx_{th})^2}{2\sigma}\right)$$

The dE/dx in the DCH is measured in arbitrary units because a direct calibration is tedious and not necessary for analysis. For reference, tracks with momenta between 0.5 and 5.0 GeV have dE/dx values between 400 and 1500 in these arbitrary units.

A dE/dx measurement in a cell is used if the track passes through the inner 95% of the cell area. A minimum of eight usable cell samples is required in order to calculate a reliable likelihood. To mitigate the effects of Landau functions, only the smallest 80% (rounding down) of the samples are used. The expected dE/dx is calculated from a calibrated Bethe-Bloch equation, using the reconstructed value of the momentum in the DCH for a given hypothesis. The uncertainity on the measured dE/dx is a complicated function of the measured mean, the number of samples, the root mean square (RMS) of the dE/dx values, and the track hypothesis. If the error is found to be less than 0.1 units, the calculation is flagged as non-physical and the result is excluded from likelihood comparison.

The DIRC likelihood is calculated using the number of photons detected in the Cerenkov ring and the angle of the Cerenkov cone with respect to the track direction as it enters the DIRC. The expected number of photons, N^{exp}, is taken from a calibration table created using a large number of reconstructed tracks.

The expected Cherenkov angle, θ_C^{exp}, is determined using the track momentum at the entrance to the DIRC, the track mass hypothesis, $\cos(\theta_C) = \frac{1}{n\beta}$ and $\beta = \frac{p}{\sqrt{(pc)^2+(mc^2)^2}}$. The measured Cherenkov angle, θ_C^{meas}, and its error, σ_C, are calculated from fitting the ring of photons observed in the DIRC photo-multiplier tubes.

The final likelihood is found by multiplying a Poisson distribution for the measured number of photons and Gaussian distribution for the measured Cerenkov angle:

$$\mathcal{L} = \frac{1}{\sqrt{2\pi\sigma_C}} e^{\frac{\theta_C^{exp}-\theta_C^{meas}}{2\sigma_C}} \times \frac{e^{-N^{exp}}(N^{exp})^{N^{obs}}}{N^{obs}!}$$

In the case of proton likelihood selector a particle is selected by comparing it's proton likelihood to that of pion and kaon, with an electron veto applied in some criteria. The proton LH selector has 4 distinct criteria - `veryLoose, Loose, Tight, VeryTight`, as in table 4.1. This analysis use the `VeryLoose` protons.

Table 4.1: Selection criteria for the Proton LH Selector

`VeryLoose`	L(p)/L(K) $>$ 4/3 L(p)/L(pi) $>$ 0.5
`Loose`	L(p)/L(K) $>$ 3.0 L(p)/L(pi) $>$ 0.5 if p$>$ 0.75 reject tight "PidLHElectronSelector" electrons
`Tight`	L(p)/L(K) $>$ 5.0 L(p)/L(pi) $>$ 0.75 if p$>$ 0.75 reject tight "PidLHElectronSelector" electrons
`VeryTight`	L(p)/L(K) $>$ 10.0 L(p)/L(pi) $>$ 0.96 if p$>$ 0.75 reject tight "PidLHElectronSelector" electrons reject tight "PidMuonMicroSelector" muons

Kaon Identification

The kaon selection used in this analysis is based on likelihood selector. Kaon LH selectors use information from the SVT, DCH, and DIRC. The selectors depend on the ionization energy loss, dE/dx, in the SVT and DCH, the Cherenkov angle, θ_C, and the number of photons in the DIRC. The kaon information from each of the detectors is limited to particular momentum ranges. Measurement of dE/dx information provides kaon separation below 700 MeV/c, and again above 1.5 GeV/c due to the relativistic rise for pions. The DIRC provides π/K separation above 600 GeV/c.

There are four main selection categories for kaon identification: `NotaPion`, `Loose`, `Tight` and `VeryTight`. The corresponding selection criteria are shown in table 4.2. This analysis used `Loose` and `Tight` kaon selection.

Table 4.2: Kaon ID selection criteria. The momentum cuts to include the likelihood from each detector are also shown. L_i is the likelihood for particle type i. The value r_π represents the ratio of likelihood values. It used as the threshold for selecting the kaon at specific momenta.

	`Loose`	`Tight`
SVT (GeV/c) DCH (GeV/c) DIRC (GeV/c)	p < 0.6; p > 1.5 p < 0.6; p > 1.5 p > 0.6	p < 0.7 p < 0.7 p > 0.6
Likelihood Requirements	L(K)/L(P) $\geq$ 1;L(K)/L(π) $> r_\pi$ P < 2.7 GeV/c: r_π =1 P > 2.7 GeV/c: r_π =80 $0.5 <$ p < 0.7 GeV/c: r_π =15	L(K)/L(P) $>$ 1;L(K)/L(π) $> r_\pi$ P > 2.7 GeV/c: r_π =1 P > 2.7 GeV/c: r_π =80 $0.5 <$ p < 0.7 GeV/c: r_π =15

	`VeryTight`	`NotaPion`
SVT (GeV/c) DCH (GeV/c) DIRC (GeV/c)	p < 0.6; p > 1.5 p < 0.6; p > 1.5 p > 0.6	p < 0.5 p < 0.6 p > 0.6
Likelihood Requirements	L(K)/L(P) $>$ 1;L(K)/L(P) $> r_\pi$ P < 2.5 GeV/c: r_π =3 P > 2.5 GeV/c: r_π =200 $0.4 <$ p < 0.7 GeV/c: r_π =20	Default = true. Reject if: L(P)/L(π) $> r_\pi$; L(K)/L(π) $> r_\pi$ P ≤ 0.5 GeV/c: r_π =0.1 p > 0.5 GeV/c: r_π =1.0

PID Control Samples

In order to properly measure the efficiency of any particle identification algorithm, pure samples of the different particle species are required. The samples must be obtained without using any PID algorithm; otherwise, the efficiencies would be biased. Certain specific events can be used to obtain control samples.

The control samples for hadrons are obtained by reconstructing certain specific decays. The hadrons in question are identifiable among the decay products. The proton control sample is identified from the $\Lambda \to p\pi^-$. The kaon control sample is identified from the decay chain $D^* \to D^0\pi$, $D^0 \to K\pi$. The proton and the kaon in these decays can be cleanly isolated [32]. The pions in the D^0 decay can also be isolated into a control sample in the same reconstruction ($D^0 \to K\pi$). Another control sample for pions uses the decay $K^0_S \to \pi^+\pi^-$.

Chapter 5

Analysis Methods and Branching Fraction Measurements

Our understanding of the physics of charm baryons is rather poor compared to that of the charm mesons because of the shorter lifetimes and smaller production cross sections. Only during the last few years there has been significant progress in the experimental study of the hadronic decays of charmed baryons. Recent results on masses, widths, lifetimes and the decay asymmetry parameters have been published by different experiments [33, 34].
However, the accuracy in the measurements of branching fractions is only about 40% for many Cabibbo-favored modes [35], while for Cabibbo-suppressed decays the accuracy is even worse. As a consequence, we are not yet able to distinguish between the decay rate predictions made by different models e.g., between the quark model approach to non-leptonic charm decays and Heavy Quark Effective Theory (HQET) [36, 37, 38].

This chapter describes the branching ratio measurement for the Cabbibo-suppressed decays: $\Lambda_c^+ \to \Lambda K^+$, $\Lambda_c^+ \to \Lambda K^+ \pi^+ \pi^-$, relative to that of the Cabibbo-favored mode $\Lambda_c^+ \to \Lambda \pi^+$, and also for the Cabibbo-supressed decays: $\Lambda_c^+ \to \Sigma^0 K^+$, $\Lambda_c^+ \to \Sigma^0 K^+ \pi^+ \pi^-$, relative to that of Cabibbo-favored mode $\Lambda_c^+ \to \Sigma^0 \pi^+$. In addition, this chapter also describes the relative branching fraction measurement for the Cabibbo-favored mode $\Lambda_c^+ \to \Sigma^0 \pi^+$ to that of $\Lambda_c^+ \to \Lambda \pi^+$. Charge conjugated states are implied unless otherwise specified.

Monte Carlo simulation is used to determine the detection efficiencies for these decays. The analysis cuts used to select the candidates for each decay are tested using the continuum Monte Carlo as well as a small fraction of the data (used for validation of these cuts). Finally, this chapter concludes with the description of the relative branching ratio measurement results.

5.1 The technique of Branching Ratio Measurement

For a particle Λ_c^+ decaying into two different states such as $\Lambda_c^+ \to \Lambda K^+$ (a Cabibbo-suppressed mode) and $\Lambda_c^+ \to \Lambda \pi^+$ (a Cabibbo-favored mode also one of our normalization mode), the relative branching ratio is determined by the following formula:

$$\frac{\mathcal{B}(\Lambda_c^+ \to \Lambda K^+)}{\mathcal{B}(\Lambda_c^+ \to \Lambda \pi^+)} = \frac{Y(\Lambda_c^+ \to \Lambda K^+)}{Y(\Lambda_c^+ \to \Lambda \pi^+)} \times \frac{\epsilon(\Lambda_c^+ \to \Lambda \pi^+)}{\epsilon(\Lambda_c^+ \to \Lambda K^+)}$$

where Y is the raw yield for each decay mode, and ϵ is the corresponding Monte Carlo efficiency, which is defined as the Monte Carlo event yield for the selected candidate for Λ_c^+ for the final state, such as $\Lambda_c^+ \to \Lambda K^+$ divided by the number of generated Monte Carlo events for that state.

5.2 Event Selection Criteria

The analysis presented here involves either Λ or Σ^0 as one of the final states in each decay mode of Λ_c, in combination either with K^+, or with K^+, π^+ and π^- for Cabibbo-suppressed decay modes, or in combination with π^+ for Cabibbo-favored modes.

5.2.1 Selection of Λ Candidates

All of our decay modes involve Λ in the final state either directly or indirectly, where $\mathcal{B}(\Lambda \to p\pi^-) \approx 64\%$. Candidates for Λ are reconstructed by pairing oppositely charged proton and pion candidates and performing a constrained vertex fit. An acceptable $p\pi^-$ candidate must have a fit probability P_{χ^2} of Λ vertex greater than 0.1%. For proton candidates, we use the likelihood selector 'PidProtonLHSelector' and for pion candidates we use the likelihood selector 'PidPionLHSelector'. We have performed PID optimization for the proton and the pion candidates to achieve the best possible values of the signal significance, $\frac{S}{\sqrt{(S+B)}}$, using different available proton and pion lists which have been mapped to the `ChargedTrack` list using the micro data base. Here S represents the signal yield of Λ candidates obtained from a double-Gaussian fit, and B represents the background count. Based on this selection proton candidates were selected from 'PLhVeryLoose' list and pion candidates were selected from 'PiLHVeryLoose' list, as presented in table 5.2.1.

To suppress combinatorial background we require the (three-dimensional) flight distance r of each Λ candidate between its decay vertex and the interaction point (IP) to be greater than a minimal value r_{min}. As summarized in table 5.2.1, our study finds an optimal selection of Λ candidates for $r > r_{min} = 0.2\ cm$.

Table 5.1: Signal significance of Λ candidates for different PID selections of proton and pion in the continuum MC.

	Proton	Pion	$\frac{S}{\sqrt{(S+B)}}$
1	PLhVeryLoose	PiLHVeryLoose	861.06
2	PLhVeryLoose	PiLLoose	860.96
3	PLhVeryLoose	PiLTight	859.25
4	PLhVeryLoose	PiLHVeryTight	848.19
5	PLhLoose	PiLHVeryLoose	841.39
6	PLhLoose	PiLLoose	840.29
7	PLhLoose	PiLTight	839.82
8	PLhLoose	PiLHVeryTight	830.79
9	PLhTight	PiLHVeryLoose	832.93
10	PLhTight	PiLHLoose	831.85
11	PLhTight	PiLHTight	831.64
12	PLhTight	PiLHVeryTight	823.08

Table 5.2: Signal significance of Λ candidates for different values of minimal flight distance r_{min} in the continuum MC .

	Flight cut r_{min} (cm) for Λ	$\frac{S}{\sqrt{(S+B)}}$
1	> 0.08	900.65
2	> 0.09	900.77
3	> 0.1	900.83
4	> 0.2	901.34
5	> 0.3	900.22
6	> 0.4	898.62

5.2.2 Selection of Σ^0 Candidates

Since $\mathcal{B}(\Sigma^0 \to \Lambda\gamma) \approx 100\%$, Σ^0 hyperon candidates were formed by combining already identified Λ candidates selected from Λ mass band (which is chosen to be

± 3 MeV/c^2) and photon candidates were selected from the 'GoodPhotonLoose' list whose calorimeter cluster energy $E_\gamma > 100\,\mathrm{MeV}$.

5.2.3 Selection of Λ_c^+ Candidates

Λ_c^+ candidates were reconstructed in the six decay modes described in the beginning of this chapter, using the selected Λ and Σ^0 candidates.

In order to suppress combinatorial and $B\overline{B}$ backgrounds, we require Λ_c^+ candidates to have scaled momentum.

$$x_p = \frac{p^*(\Lambda_c^+)}{\sqrt{(\frac{s}{4} - M^2)}} > 0.5$$

where $p^*(\Lambda_c^+)$ and $\sqrt{s}$ are the reconstructed Λ_c^+ momentum and total e^+ e^- beam energy in the center of mass frame, respectively, as shown in Figure 5.1. M is the reconstructed invariant mass of Λ_c^+ in different decays modes mentioned above.

5.2.4 $\Lambda_c^+ \to \Lambda\pi^+$ and $\Lambda_c^+ \to \Lambda K^+$ modes

For Λ_c^+ selection in the decay modes involving Λ in the final state, we first select Λ candidates of invariant mass within an ± 3MeV/c^2 interval around the nominal value, corresponding to a band of 2.0 σ, which has been chosen for optimal significance $\frac{S}{\sqrt{(S+B)}}$ from the different values of Λ resolution as in table 5.2.4.

For $\Lambda_c^+ \to \Lambda\pi^+$ candidates, we combined Λ candidates, selected with a criteria described earlier, with a pion candidate. For the pion candidates `GoodTracksVeryLoose` were used which were then mapped to different pion lists using Likelihood selector

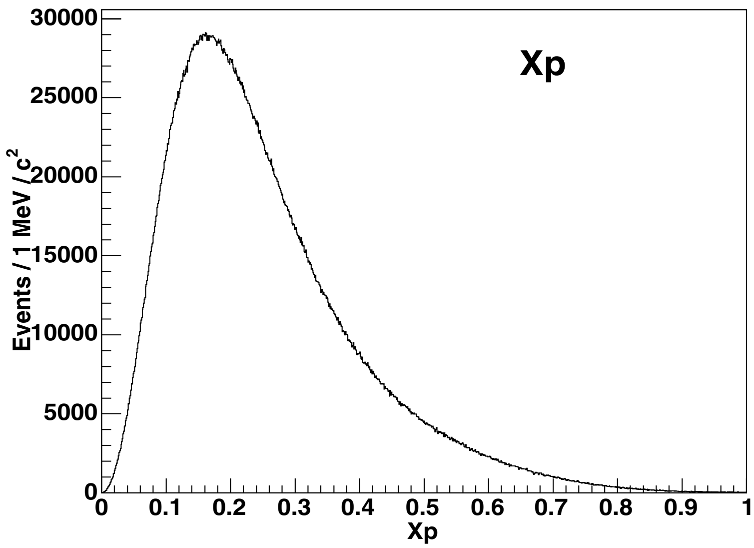

Figure 5.1: Momentum spectrum distribution for Λ_c^+ from Signal MC.

(PidPionLHSelector), For the pion coming from Λ_c^+ the value of $\frac{S}{\sqrt{(S+B)}}$ using different available pion lists as shown in table 5.2.4, we choose 'PiLHLoose'.

To identify the kaon candidates the 'PidKaonLHSelector' was used. As presented in table 5.2.4, the signal significance $\frac{S}{\sqrt{(S+B)}}$ for Λ_c^+ candidates which are thereby obtained is found optimal for kaon candidates from the 'KLHLoose' selector.

5.2.5 The decay mode $\Lambda_c^+ \rightarrow \Lambda K^+ \pi^+ \pi^-$

To search for the Λ_c^+ in the decay mode $\Lambda_c^+ \rightarrow \Lambda K^+ \pi^+ \pi^-$ (which had not been observed yet) we combine each Λ candidate selected with the criteria described above, with a K^+, a π^+, and a π^- candidate. We use 'PidKaonLikelihood' selector to identify kaon and 'PidPionLHSelector' to identify pions. Here mapping was done for kaon (using available PidKaonLikelihood lists) and for pions (using available

Table 5.3: Signal significance of Λ_c candidates for Λ candidates selected from mass bands of different widths (in units of Λ peak resolution, σ) in continuum MC.

	Width $\sigma_{RMS} = \sigma$ of Λ	$\frac{S}{\sqrt{(S+B)}}$
1	1.0 σ	33.77
2	2.0 σ	35.02
3	2.5 σ	34.57
4	3.0 σ	34.33
5	3.5 σ	34.23

Table 5.4: Signal significance of Λ_c candidates for pion candidates satisfying different PID requirements.

	Pion	$\frac{S}{\sqrt{(S+B)}}$
1	PiLHVeryLoose	132.45
2	PiLHLoose	132.67
3	PiLHTight	130.93
4	PiLHVeryTight	125.76

PidPionLHSelector lists) on the tracks coming from `GoodTracksVeryLoose` list.

5.2.6 The decay mode $\Lambda_c^+ \to \Sigma^0 \pi^+$ and $\Lambda_c^+ \to \Sigma^0\ K^+$

The distribution of the difference between invariant masses $\Delta M = M(\Lambda\gamma) - M(\Lambda)$ of the Σ^0 candidates described above is found to have a resolution $\sigma = \sigma_{\Delta M} = 4\mathrm{MeV/c}^2$, as shown in Figure 5.2.

For the Λ_c decay modes involving Σ^0 in the final state, we accept combinations of Λ and γ candidates as Σ^0 candidates if their ΔM has a value within $\pm 10\mathrm{MeV/c}^2$ of the nominal mass difference $M(\Lambda\gamma) - M(\Lambda) = 76.7\mathrm{MeV/c}^2$, corresponding to a

Table 5.5: Signal significance of Λ_c candidates for kaon candidates satisfying different PID requirements.

	Kaon	$\frac{S}{\sqrt{(S+B)}}$
1	KLHLoose	94.22
2	KLHTight	92.94
3	KLHVeryTight	92.63
4	KLHNotTight	88.52

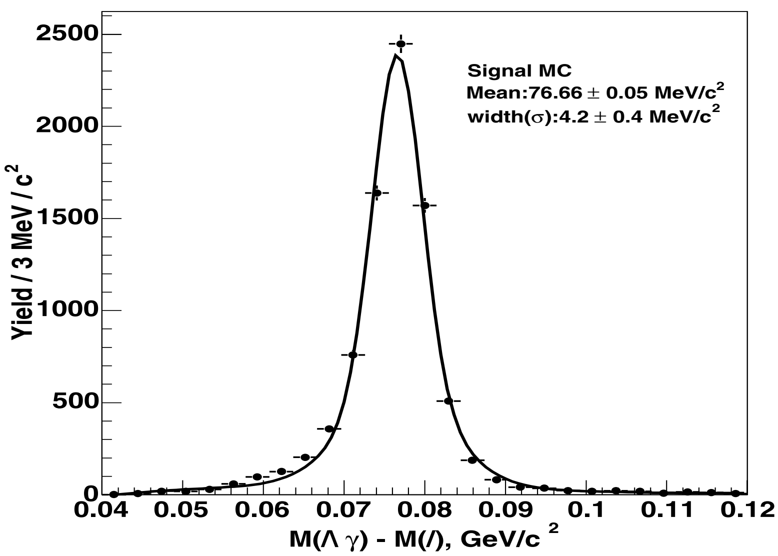

Figure 5.2: Mass Plot showing M($\Lambda\gamma$) - M(Λ) for Signal MC events.

selection within $\pm 2.5\sigma$. Table 5.2.6 shows the variation of the signal significance of Λ_c candidates with selection of Σ^0 candidates for various values of this parameter.

Each Σ^0 candidate satisfying the described selection requirements and one appropriately charged pion or kaon candidate identified through the available lists from 'PidPionLHSelector' or 'PidKaonLHSelector' were combined to form a Λ_c^+ candidate having decayed as $\Lambda_c^+ \to \Sigma^0 \pi^+$ or $\Lambda_c^+ \to \Sigma^0 K^+$, respectively. Here again mapping was

Table 5.6: Signal significance of Λ_c candidates for different selections of Σ^0 candidates from continuum MC.

	Width σ of $\Lambda\gamma$ - Λ	$\frac{S}{\sqrt{(S+B)}}$
1	2.0 σ	33.18
2	2.5 σ	33.43
3	3.0 σ	33.49
4	3.5 σ	33.21
5	4.0 σ	32.51

done using the available lists for pion and kaon to tracks from `GoodTracksVeryLoose` list.

5.2.7 $\Lambda_c^+ \to \Sigma^0 \ K^+\pi^+\pi^-$ mode

In order to reconstruct Λ_c^+ in this decay mode (which has not been observed before), we again accept Σ^0 candidates of ΔM within (76.7 ± 10)MeV/c^2, and combine them with a kaon and two oppositely charged pions. We use 'PidKaonLHSelector' to identify a kaon and 'PidPionLHSelector' to identify pions. Mapping was done using LikelihoodSelctors lists to the tracks from `GoodTracksVeryLoose` lists, for these selected kaon and pions.

5.3 Monte Carlo Study

5.3.1 Signal Monte Carlo

In order to determine fit parameters of the Λ_c signals and the detection efficiencies for the six Λ_c decay modes under consideration, six samples of approximately 100,000

Monte Carlo-simulated signal events in the corresponding mode were generated. PID optimization and studies of background shape were performed using Monte Carlo samples of $B\overline{B}$, $c\overline{c}$ and $u\overline{u}/d\overline{d}/s\overline{s}$ equivalent to an integrated luminosity of 60 fb^{-1}. All Monte Carlo samples were produced in SP5.

5.3.2 Decay modes $\Lambda_c^+ \to \Lambda\pi^+$and $\Lambda_c^+ \to \Lambda K^+$

For decay modes involving Λ in the final state, where $\Lambda \to p\pi^-$, we have reconstructed Λ as described in section 5.2. The Λ invariant mass is fitted using two Gaussian functions with same mean for the signal, plus a second-order polynomial to fit to the combinatorial background. The root-mean-square value of the fit function is calculated as:

$$\sigma_{RMS}^2 = f_1\sigma_1^2 + f_2\sigma_2^2$$

where f_1 and f_2 are fractions of the areas under Gaussian functions one and two, respectively, and σ_1 and σ_2 are two corresponding widths. As shown in Figure 5.3, the fitted mean value and width are found to be: 1116.0 MeV/c^2 and $\sigma_{RMS} = \sigma =$ 1.5 MeV/c^2, respectively.

In order to find the detection efficiency $\epsilon_{\Lambda\pi^+}$ for the decay mode $\Lambda_c^+ \to \Lambda\pi^+$ we have used a sample of 154,000 signal events generated in SP5 MC, containing 98025 Λ_c^+ baryons. The detection efficiency for this decay mode was found to be $\epsilon_{\Lambda\pi^+} = 31.2 \pm 0.2$ $(stat)$ %. The fit values for the mean and the width(σ) of Λ_c^+ are: 2286.0 ± 0.04 MeV/c^2 and 7.9 MeV/c^2, respectively; see Figure 5.4.

The detection efficiency $\epsilon_{\Lambda K^+}$ for the decay mode $\Lambda_c^+ \to \Lambda K^+$ was obtained from

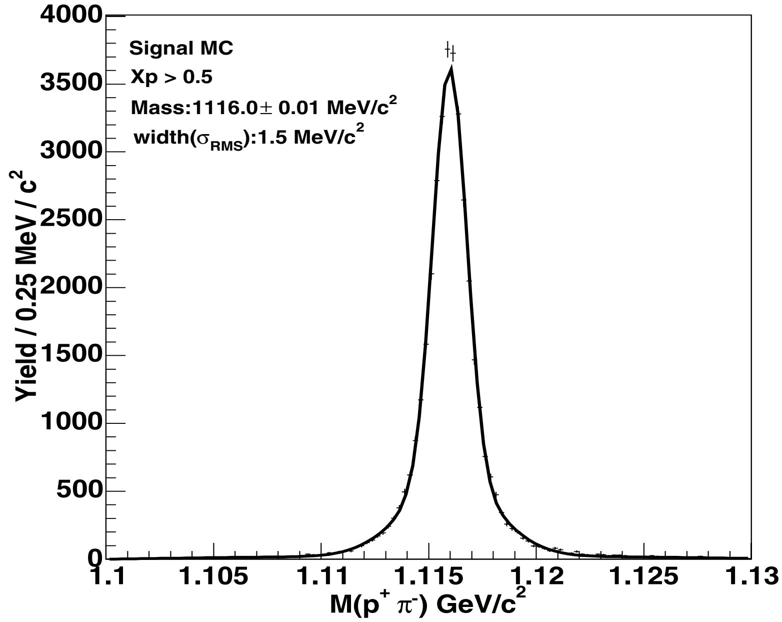

Figure 5.3: Mass plot for $\Lambda \to p\pi^-$for signal MC events.

a sample of 112,000 signal events, in which 72812 Λ_c^+ baryons had been generated. We obtain $\epsilon_{\Lambda K^+} = 25.0 \pm 0.2$ $(stat)$ %, together with fitted width of 6.1MeV/c^2 and a mean of 2285.17 ± 0.05MeV/c^2, as shown in Figure 5.5. The PDG value for the Λ_c^+ mass [35] is:2284.9 ± 0.6MeV/c^2.

5.3.3 Decay mode $\Lambda_c^+ \to \Lambda K^+ \pi^+ \pi^-$

To determine the detection efficiency for the decay mode $\Lambda_c^+ \to \Lambda K^+ \pi^+ \pi^-$ we use a sample of 76,000 signal events generated in SP5 MC. This decay mode is a first time search. Detection efficiency is found by using the number of events at the generator level for $x_p > 0.6$. The contribution due to Cabibbo-favored modes $\Lambda_c^+ \to \Xi^- K^+ \pi^+$ and $\Lambda_c^+ \to \Lambda \overline{K^0} K^+$ was removed, which have been discussed briefly in

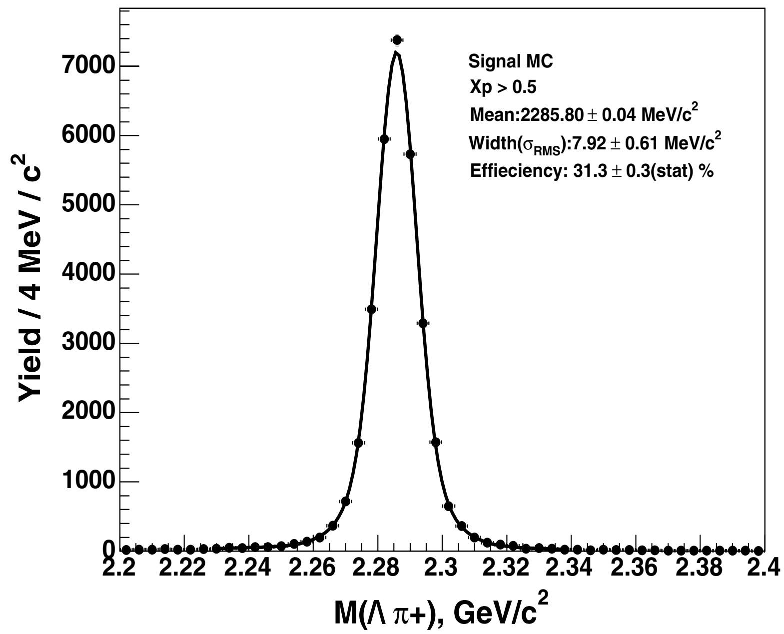

Figure 5.4: Mass plot for $\Lambda_c^+ \to \Lambda\pi^+$for signal MC events.

the coming sections. The fitted mean and width are 2286.5 ± 0.1(stat) MeV/c^2, and 5.0 ± 0.1(stat) MeV/c^2 respectively, as shown in Figure 5.6. The detection efficiency $\epsilon_{\Lambda K^+\pi^+\pi^-}$ for this mode is found to be: $11.1 \pm 0.1\%$.

5.3.4 Decay modes $\Lambda_c^+ \to \Sigma^0\pi^+$ and $\Lambda_c^+ \to \Sigma^0 K^+$

For decay modes involving Σ^0 in the final state we use $\Sigma^0 \to \Lambda\gamma$ with $\Lambda \to p\pi^-$. The mass difference between M($\Lambda\gamma$) - M(Λ) is fitted using two Gaussian functions to fit the signal region and a 3rd order polynomial for the background. We find the width(σ) is about 4 MeV/c^2 as shown in Figure 5.2. We accept candidates with $(\Sigma^0 - \Lambda)$ mass window within ± 10 MeV/c^2 to reconstruct Λ_c^+.

Determination of the detection efficiency $\epsilon_{\Sigma^0\pi^+}$ was based on a sample of 110,000

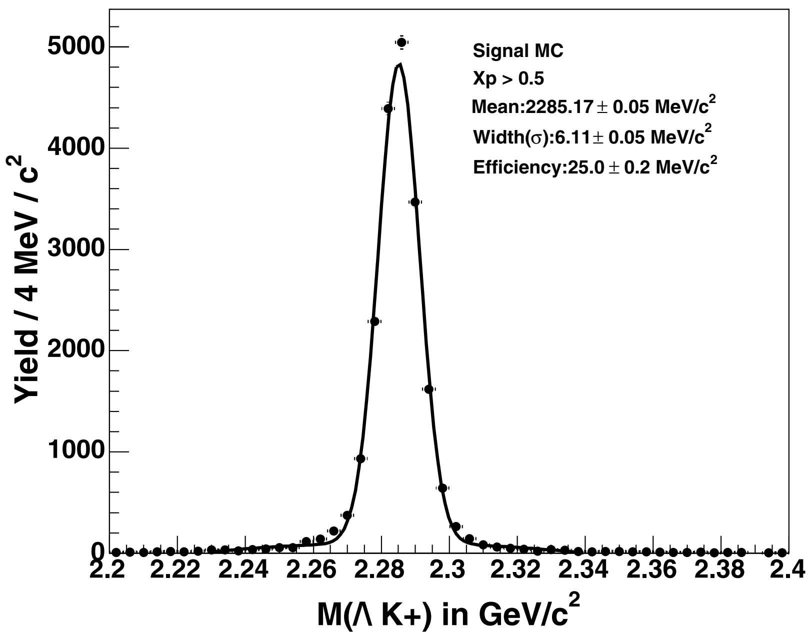

Figure 5.5: Mass plot for $\Lambda_c^+ \to \Lambda K^+$ for signal MC events.

signal MC events (produced in SP5). We found 70202 events at the generator level. Fitting the invariant mass histogram of reconstructed Λ_c^+ candidates with a single Gaussian function and a third order polynomial, accounting for the shapes of the signal and the combinatorial backgrounds, respectively (Figure 5.7), we obtain a signal mean of 2285.0 ± 0.1MeV/c^2 and a width of 7.0 ± 0.1 MeV/c^2. The detection efficiency is found to be $\epsilon_{\Sigma^0 \pi^+} = 11.9 \pm 0.1$(stat)%.

The Cabibbo-suppressed decay mode $\Lambda_c^+ \to \Sigma^0\ K^+$ is reconstructed by combining already reconstructed Σ^0 with a kaon. We use 110,000 SP5 signal MC events inorder to find the detection effeciency for this mode. The fit to signal Monte Carlo obtains 2285.0 ± 0.1MeV/c^2 for a Mean and 6.1 ± 0.1 MeV/c^2 for a width, where the detection efficiency comes out to be 9.5 ± 0.1(stat)%, as shown in Figure 5.8.

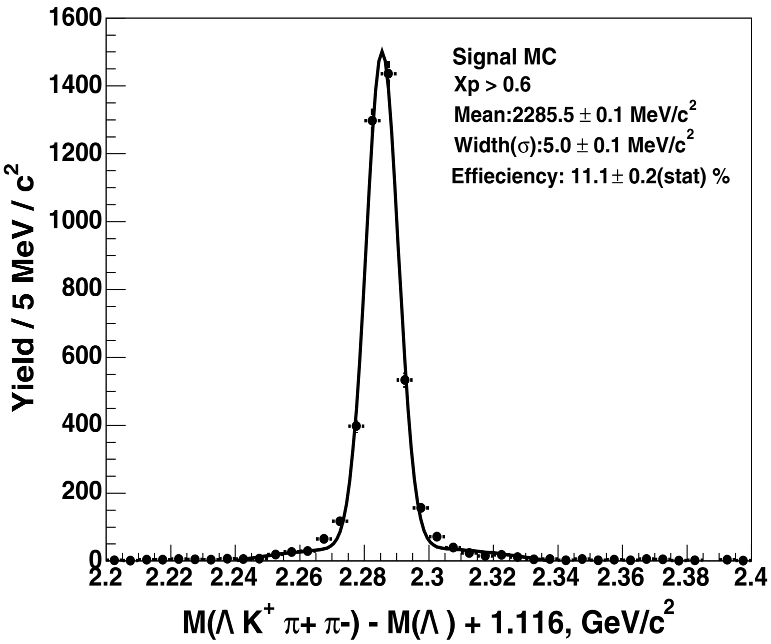

Figure 5.6: Mass plot for $\Lambda_c^+ \to \Lambda K^+\pi^+\pi^-$for signal MC events.

5.3.5 Decay mode $\Lambda_c^+ \to \Sigma^0\ K^+\pi^+\pi^-$

We have used 76,000 signal MC events for this decay mode. In order to measure the detection efficiency we have used 48213 events at the generator level. The detection efficiency $\epsilon_{\Sigma^0 K^+\pi^+\pi^-}$ is found to be $5.3 \pm 0.1\%$. The fitted mean value and the width (σ) are 2285.0 ± 0.1 MeV/c^2 and 4.4 ± 0.1 MeV/c^2 respectively; as shown in Figure 5.9. Table 5.3.5 summarizes for each decay mode the number of signal MC events generated, and the detection efficiencies found.

5.3.6 Continuum MC Study of $c\overline{c}$ and $u\overline{u}/d\overline{d}/s\overline{s}$

We modelled signal and background originating from $c\overline{c}$ and $u\overline{u}/d\overline{d}/s\overline{s}$ continuum with a SP5 MC sample of 83.56×10^6 $c\overline{c}$ events and 68.42×10^6 $u\overline{u}/d\overline{d}/s\overline{s}$ events.

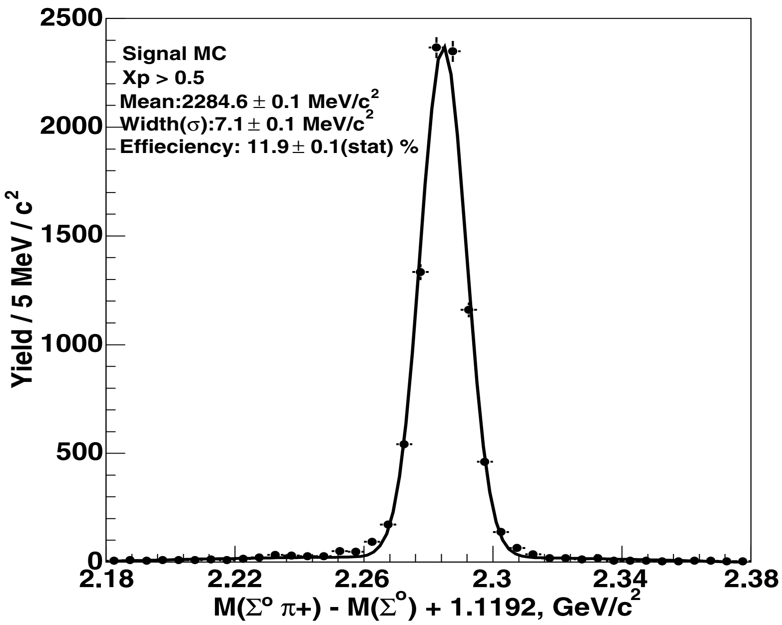

Figure 5.7: Invariant mass of $\Sigma^0\pi^+$ combinations from signal MC events.

The methods for reconstructing Λ_c^+ candidates were applied as described above, and where appropriate, a normalization to equivalent luminosity was carried out subsequently.

5.3.7 Decay modes $\Lambda_c^+ \to \Lambda\pi^+$and $\Lambda_c^+ \to \Lambda K^+$

The invariant mass of Λ candidates reconstructed in the entire MC samples is shown in Figure 5.10.

In order to reconstruct Λ_c^+ in the decay modes involving Λ in final state we select as Λ candidates all $p\pi^-$ combinations within a mass window ± 3 MeV/c^2 around the Λ nominal mass value, corresponding to 2σ of the invariant mass distribution of Figure 5.11. For decay mode $\Lambda_c^+ \to \Lambda\pi^+$, the invariant mass of Λ_c^+ is shown in

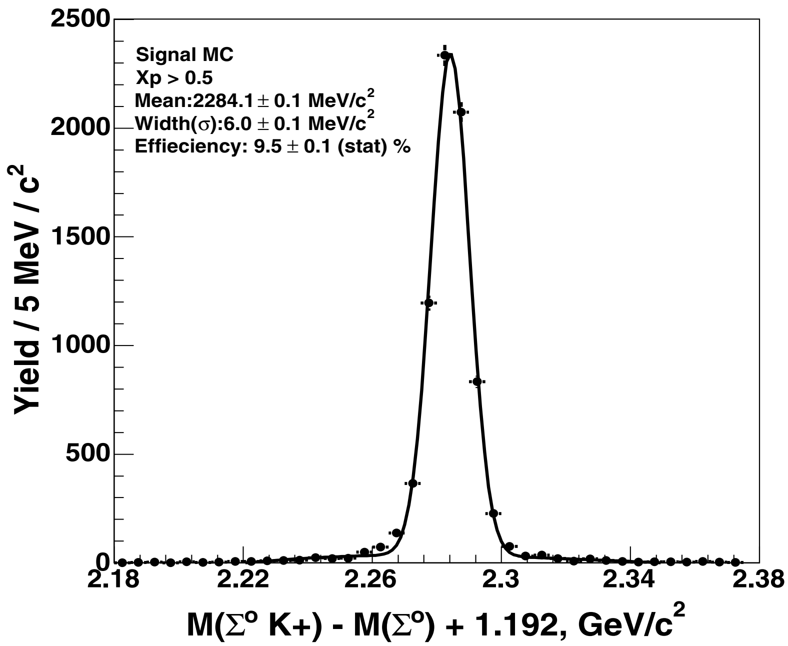

Figure 5.8: Invariant mass of $\Sigma^0 K^+$ combinations from signal MC events.

Figure 5.15.

In case of $\Lambda_c^+ \to \Lambda\pi^+$, Figure 5.12, it is evident that the background around and under the Λ_c signal region is not an approximately smooth function. An excess of $\Lambda\pi^+$ combinations below the Λ_c^+ mass, approximately in the mass range (2.12 ... 2.243) GeV/c^2, is clearly visible. As was already well-known from previous analyses and as we confirmed using MC-Truth matching, this background shape is mainly attributable to a reflection where the selected Λ and π^+ candidates were produced in the decay chain $\Lambda_c^+ \to \Sigma^0\pi^+$, $\Sigma^0 \to \Lambda\gamma$; therefore a "missing photon reflection".

In the course of our Monte-Carlo studies, we identified another source of correlated $\Lambda\pi^+$ background, whose shape, approximately in the mass range (2.1 ... 2.32) GeV/c^2, extends even under the Λ_c peak. Part of this shape is visible as a shoul-

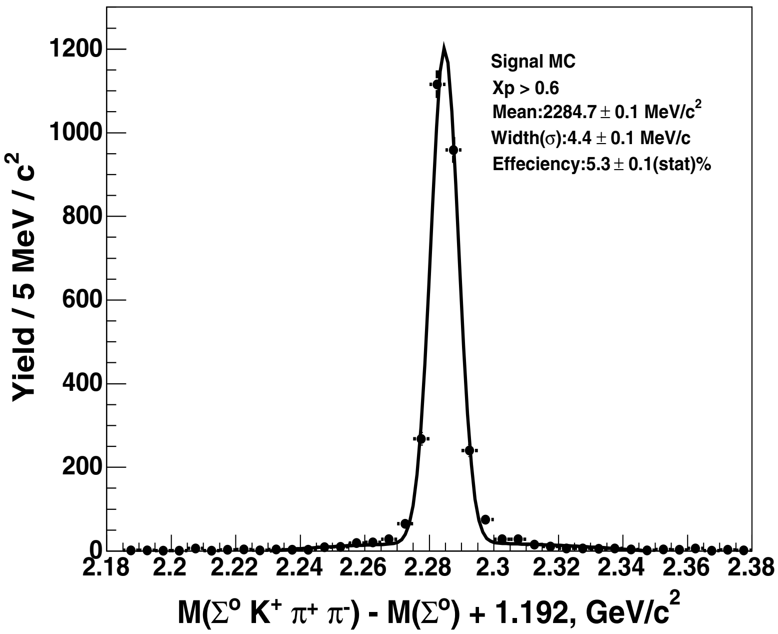

Figure 5.9: Invariant mass of $\Sigma^0 K^+\pi^+\pi^-$ combinations from signal MC events.

der above the Λ_c peak, as indicated in Figure 5.13. It arises as a "reflection from Ξ_c": due to the selected π^+ candidates having originated from decays $\Xi_c^0\to\Xi^-\pi^+$ or $\Xi_c^+\to\Xi^0\pi^+$, and the selected Λ candidates having been produced in the corresponding subsequent decays $\Xi^-\to\Lambda\pi^-$ or $\Xi^0\to\Lambda\pi^0$, respectively, with the π^- or π^0 are undetected. The invariant mass distributions of $\Lambda\pi^+$ combinations from these background sources are given in Figure 5.14, while Figure 5.15 shows fit curves to these two distributions with a square function which was smeared bin-by-bin according to the resolution of the Λ_c^+ signal. Fitting for this plot was performed using two Gaussians with same mean for the signal region and 7th order polynomial for the background.

The broad structure on the left hand side of the signal (which is due to $\Lambda_c^+\to\Sigma^0$

Table 5.7: Summary of SP5 signal MC events used and Effeciencies found for different decay modes involved in this analysis.

	Decay Mode	Number of Generated events	Effeciency(ϵ)
1	$\Lambda_c^+ \to \Lambda\pi^+$	154K	31.2 $\pm$ 0.2(stat) %
2	$\Lambda_c^+ \to \Lambda K^+$	112K	25.0 $\pm$ 0.2(stat) %
3	$\Lambda_c^+ \to \Lambda K^+\pi^+\pi^-$	76K	11.1 $\pm$ 0.1(stat) %
4	$\Lambda_c^+ \to \Sigma^0\pi^+$	110K	11.9 $\pm$ 0.1(stat) %
5	$\Lambda_c^+ \to \Sigma^0 K^+$	110K	9.5 $\pm$ 0.1(stat) %
6	$\Lambda_c^+ \to \Sigma^0 K^+\pi^+\pi^-$	76K	5.3 $\pm$ 0.1 (stat) %

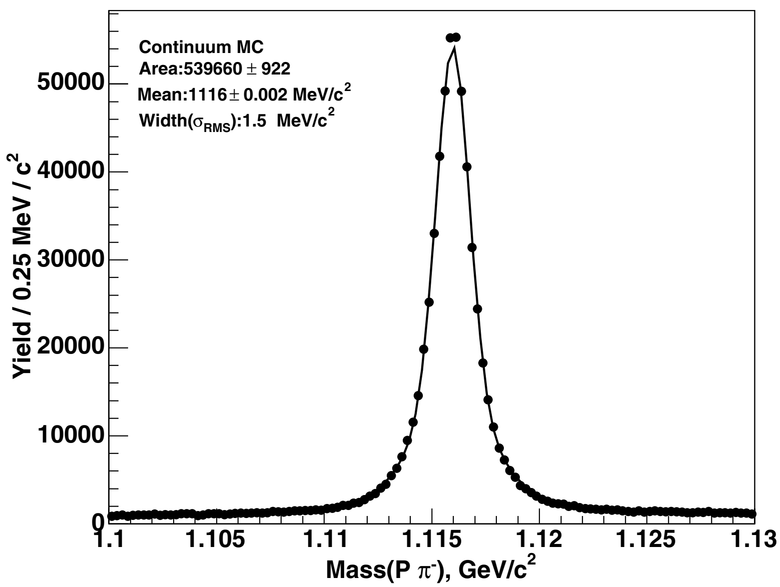

Figure 5.10: Invariant mass of $p\pi^-$ combinations from continuum MC events.

π^+ backgorund, where $\Sigma^0 \to \Lambda\gamma$, with a missing γ as described above) is fitted with a square wave function which has been sliced for each bin and then smeared according to Λ_c^+ resolution function by looping over each bin.

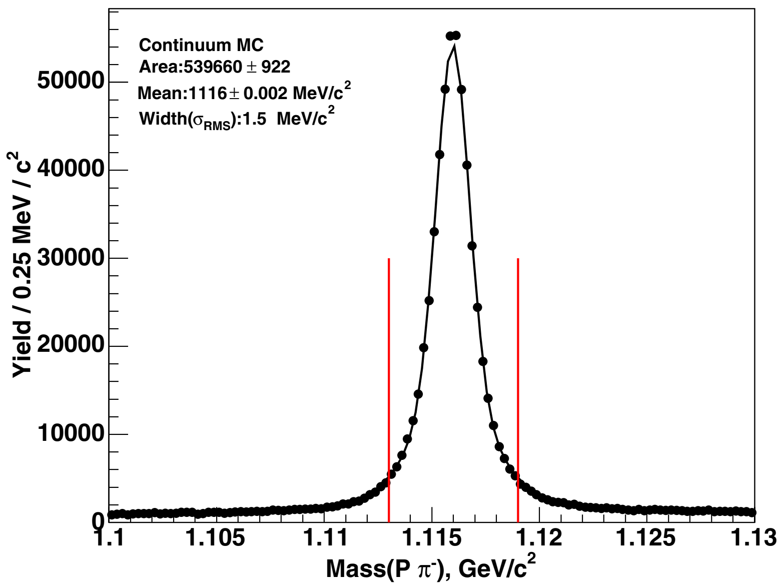

Figure 5.11: Invariant mass of $p\pi^-$ combinations from continuum MC events. Indicated is the mass window for selection of Λ candidates.

For the structure on right hand side immediately after the Λ_c^+ signal (which is due to $\Xi_c^0 \to \Xi^- \pi^+$ with $\Xi^- \to \Lambda\pi^-$, π^- undetected and this also has contribution from $\Xi_c^+ \to \Xi^0 \pi^+$ with $\Xi^0 \to \Lambda\pi^0$, π^0 undetected) is also fitted with a square wave function. Again this has been sliced for each bin and smeared according to the Λ_c^+ resolution function.

Figure 5.16 presents the invariant mass distribution of ΛK^+ combinations reconstructed from continuum MC events. We fit this distribution with a Gaussian function to represent the signal from the Cabibbo-suppressed decay mode $\Lambda_c^+ \to \Lambda K^+$, and a third order polynomial to model the background.

We obtained a raw Λ_c^+ yield of 5586$\pm$122, with a fitted mass of 2285$\pm$0.1 MeV/c^2 and width (σ) of 6.1 ± 0.1 MeV/c^2. Subsequently we noticed that 'DECAY.DEC',

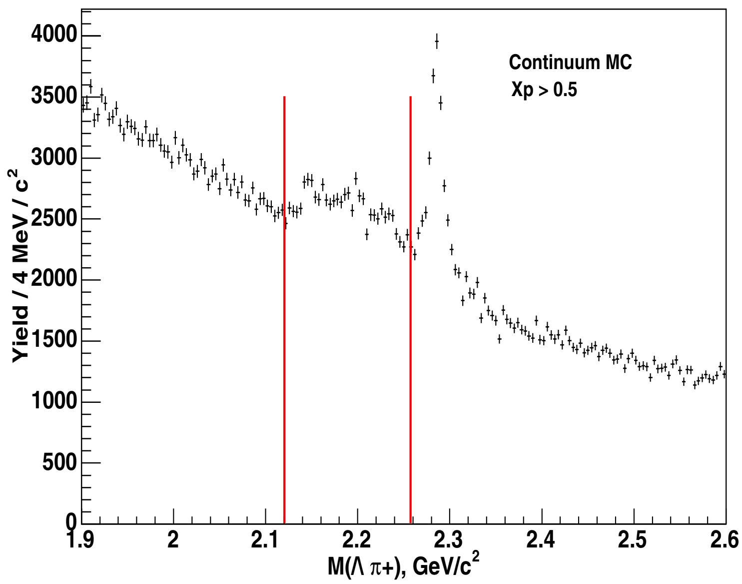

Figure 5.12: Invariant mass of $\Lambda\pi^+$ combinations for continuum MC events. Indicated is the mass range of the “missing photon reflection”.

the generic input file to the MC event generator, had prescribed the value of the Λ_c^+ branching fraction in decay mode ΛK^+ as (5.0×10^{-3}), differing by an order of magnitude from the current PDG value of $(6.7 \pm 2.5) \times 10^{-4}$ [35]. Correspondingly we expect to find a much smaller raw Λ_c^+ yield in our data sample.

5.3.8 Decay modes $\Lambda_c^+ \to \Lambda K^+ \pi^+ \pi^-$

Our analysis presents a search for, and first observation of, this decay mode of Λ_c^+, which was therefore not listed explicitly in the generic input file ‘DECAY.DEC’ to the MC event generator. Instances of the decay $\Lambda_c^+ \to \Lambda\ K^+\pi^+\pi^-$ were indeed found in our sample of continuum MC events, and the signal peak in Figure 5.17 illustrates that Λ_c^+ candidates were reconstructed accordingly. This Λ_c^+ final state

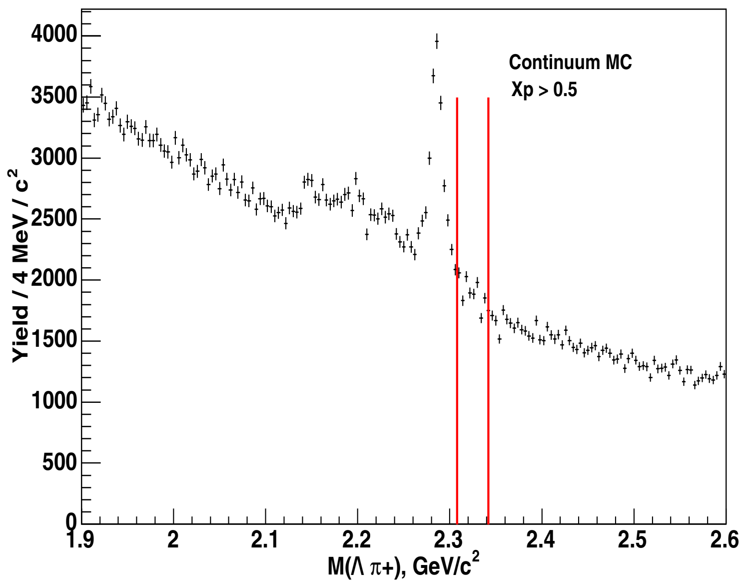

Figure 5.13: Invariant mass of $\Lambda\pi^+$ combinations for continuum MC events. Part of the background shape attributed to "reflection from Ξ_c" is visible as a shoulder of the Λ_c^+ signal peak in the indicated mass range.

seems to be a contributions from the two Cabibbo-favored decays $\Lambda_c^+ \to \Xi^- K^+ \pi^+$ and $\Lambda_c^+ \to \Lambda \overline{K^0} K^+$, where Ξ^-decays to $\Lambda\pi^-$ and K_S^0 decays to $\pi^+\pi^-$. Both of these modes has already been measured. We confirmed these contributions using MC-Truth matching for our continuum MC.

5.3.9 Decay modes $\Lambda_c^+ \to \Sigma^0\ \pi^+$and $\Lambda_c^+ \to \Sigma^0\ K^+$

In order to reconstruct Σ^0 with $\Sigma^0\ \to \Lambda\gamma$, where $\Lambda \to p\pi^-$, we combined a selected Λ candidate with a photon with calorimeter cluster energies greater than 100 MeV, using Σ^0 - Λ mass difference, as shown in Figure 5.18, to reconstruct Λ_c^+ in decay modes involving Σ^0 in the final state; as described in section 5.2.2. The invariant

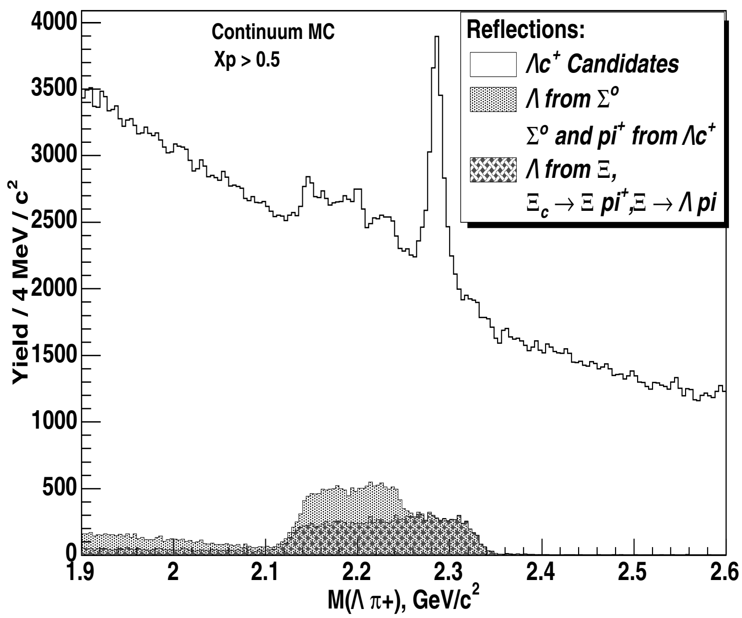

Figure 5.14: Invarant Mass of $\Lambda\pi^+$ combinations found in $c\bar{c}$ MC events; for all events, and for three sources of correlated background.

mass of Σ^0 π^+ combinations reconstructed from continuum MC is presented in Figure 5.19.

Performing a fit using a Gaussian function for the Λ_c^+ signal and a third order polynomial to fit the background, we find a raw Λ_c^+ yield of 2563 ± 95 at mass 2285 ± 0.2 MeV/c^2, and with width $\sigma = 6.3 \pm 0.2$ MeV/c^2. Combining each selected Σ^0 candidate instead with a K^+ candidate, we obtain the invariant mass distribution shown in Figure 5.20.

The fit to a Gaussian function for the Λ_c^+ signal and a third order polynomial results in 817 ± 57 Λ_c^+ candidates (raw yield) with mass 2283 ± 0.5 MeV/c^2 and width $\sigma = 6.5 \pm 0.5$ MeV/c^2.

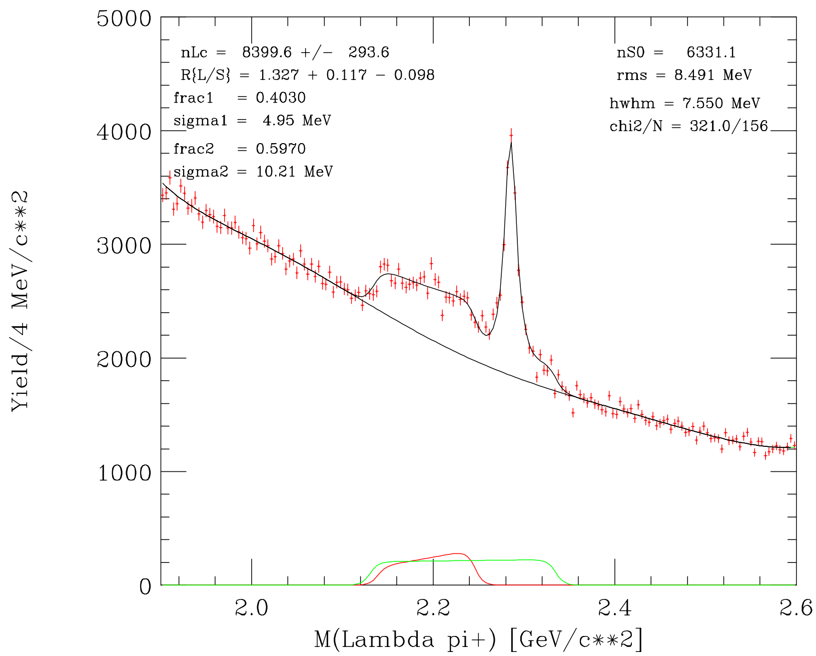

Figure 5.15: Fits to invarant mass distributions of $\Lambda\pi^+$ combinations found in $c\bar{c}$ MC events.

As for $\Lambda_c^+ \rightarrow \Lambda\ K^+$, we again found a discrepancy for the branching fraction of the Cabibbo-suppressed decay $\Lambda_c^+ \rightarrow \Sigma^0\ K^+$ between the assignment in 'DECAY.DEC', (2.0×10^{-3}), and the current PDG value of $(5.6 \pm 2.4) \times 10^{-4}$ [35]. In decay mode $\Sigma^0\ K^+$, therefore, we do not expect raw yield of Λ_c^+ candidates to be found in the data to be comparable with the equivalent amount of the continuum MC (which is found by normalizing, the number of MC events used, to the luminosity).

5.3.10 Decay mode $\Lambda_c^+ \rightarrow \Sigma^0\ K^+\pi^+\pi^-$

Prior to our analysis, this decay mode of Λ_c^+ had not been observed experimentally either, and therefore it, too, was not listed explicitly in the generic input file 'DECAY.DEC' to the MC event generator. Instances of the decay $\Lambda_c^+ \rightarrow \Sigma^0\ K^+\pi^+\pi^-$

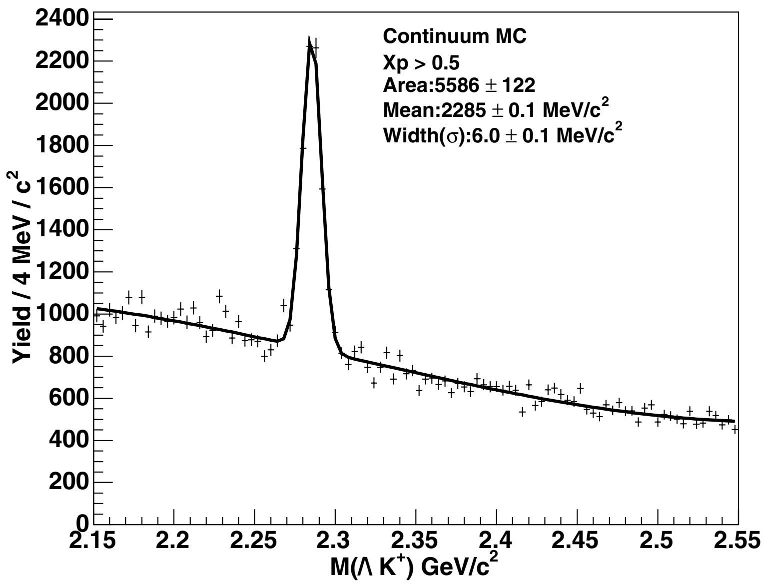

Figure 5.16: Mass distribution for $\Lambda_c^+ \to \Lambda K^+$ for continuum MC events.

were nevertheless present in our sample of continuum MC events, due to JETSET fragmentation and hadronization, and Figure 5.21 shows a corresponding Λ_c^+ signal.

5.4 Study with data

For this study, all of our cuts were validated on a randomly chosen 10% subset of the data. As already mentioned in chapter 3, this analysis used almost $125 fb^{-1}$ of series 12 on-resonance plus off-resonance data available, which includes the running period for Run1, Run2 and Run3. Since we mixed both on- and off-resonance data, in order to see any inconsistency we checked the ratio of the signal yield both from on-resonance as well as from the off-resonance data by normalizing these yields to the luminosity, $112 fb^{-1}$ on-resonance and almost $13 fb^{-1}$ off-resonance. We have

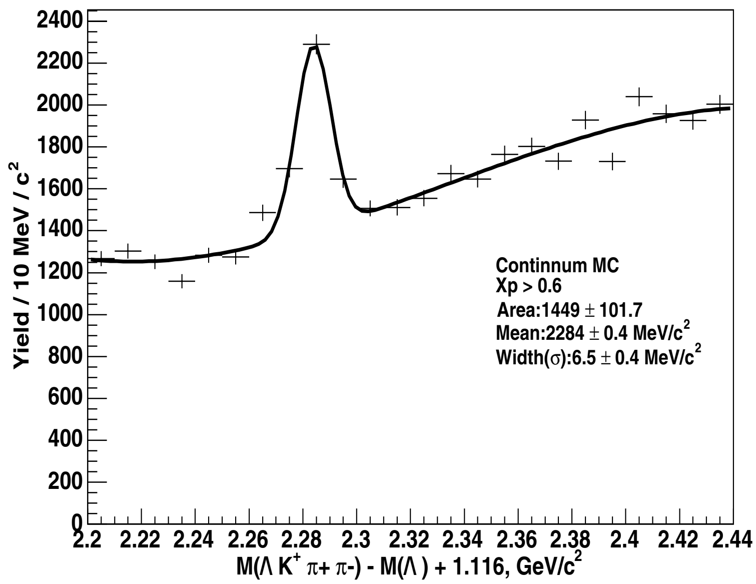

Figure 5.17: Invariant mass distribution for ($\Lambda K^+\pi^+\pi^-$) combinations from continuum MC. The excess yield above the smooth background is due to decays of Λ_c^+ into the Cabibbo-favored final states $\Xi^- K^+\pi^+$ and $\Lambda K_S^0 K^+$, which are contributing to this Cabibbo-suppressed decay mode and are present in our MC samples.

found the ratio to be 1.04 ± 0.04(stat).

5.4.1 Observation of $\Lambda_c^+ \to \Lambda\pi^+$

As discused earlier in this chapter, all of our decay modes involve Λ in the final state directly or indirectly (as $\Sigma^0 \to \Lambda\ \gamma$). Therefore, we have reconstructed the Λ first, in the decay mode $\Lambda \to p\pi^-$ using the reconstruction method described in section 5.2. The RMS value of the width (σ) from the MC is found to be consistent with the RMS value of the width (σ) from the data which is 1.5 MeV/c^2, as illustrated in Figures 5.22 from data and 5.3 from MC. The $\Lambda_c^+ \to \Lambda\pi^+$ was reconstructed using

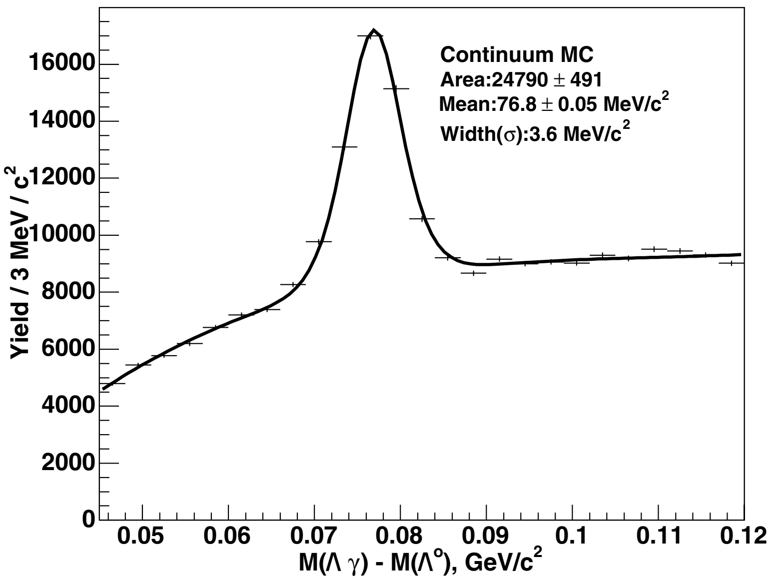

Figure 5.18: Mass difference distribution M($\Lambda\gamma$) - M(Λ) from continuum MC, used to model the data.

the already selected Λ candidates, which is our normalization mode for the decay modes involving Λ in the final state, with selection criteria described in section 5.2. We fit the signal region with two Gaussians having the same mean and use a square wave function to fit the broad structure in the region 2.12 to 2.24 GeV/c^2, which is a reflection due to $\Lambda_c^+ \to \Sigma^0\ \pi^+$, $\Sigma^0 \to \Lambda\gamma$ with a missing γ, contributing to the background. Also there is small bump just below the Λ_c^+ signal region leading the signal, contributing to the background, this reflection is due to $\Xi_c^0 \to \Xi^-\pi^+$ with $\Xi^- \to \Lambda\pi^-$, π^-undetected and also due to $\Xi_c^+ \to \Xi^0\pi^+$ with $\Xi^0 \to \Lambda\pi^0$, π^0 undetected (as discussed in section 5.3.6), is fitted with a square wave function. we use 7th order polynomial function to fit the background. Fit yields 33543.0 ± 334 (stat), $\Lambda_c^+ \to \Lambda\pi^+$. The width floated $\sigma_{RMS} = 8.2$ MeV/c^2, which is close to our Monte Carlo

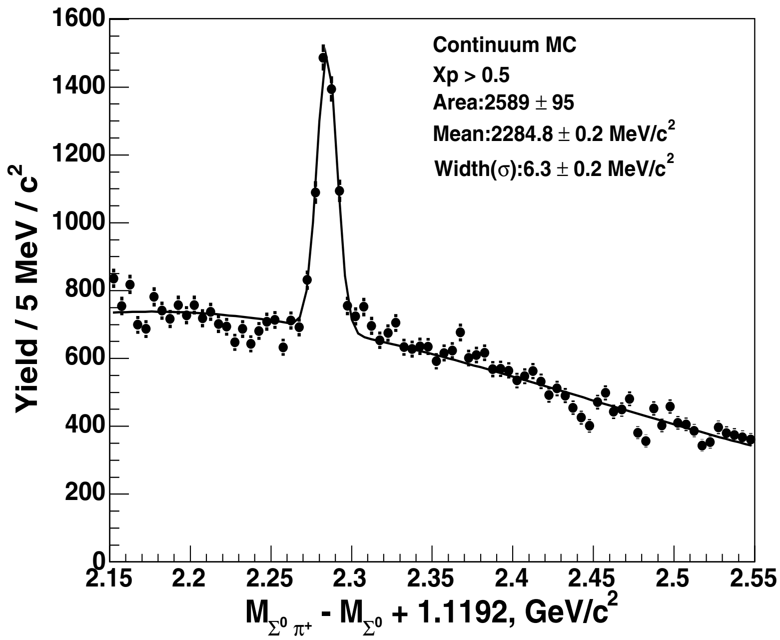

Figure 5.19: Invariant mass distribution for $\Lambda_c^+ \to \Sigma\ \pi^+$ from continuum MC, used to model the data.

value for the σ_{RMS} = 8.3 MeV/c^2. Fit also yields 32693.0 ± 324 (stat) , $\Lambda_c^+ \to \Sigma^0$ π^+, $\Sigma^0 \to \Lambda\gamma$ (with a missing γ), in the broad region from 2.12 to 2.24 GeV/c^2, as shown in Figure 5.23.

For $\Lambda_c^+ \to \Lambda\pi^+$the fit matches nicely to give almost equal number of $\Lambda_c^+ \to \Sigma^0\pi^+$ $\Sigma^0 \to \Lambda\gamma$ with a missing γ in it as discussed earlier in detail and is also illustrated in the Figure 5.23. We include the measurement of branching ratio for $\Lambda_c^+ \to \Sigma^0\pi^+$ to $\Lambda_c^+ \to \Lambda\pi^+$ from this fit. Relative detection efficiency ratio for this measurement is found to be:

$$\frac{\epsilon(\Lambda_c^+ \to \Sigma^0\pi^+)}{\epsilon(\Lambda_c^+ \to \Lambda\pi^+)} = \frac{0.317}{0.313} = 1.01 \pm 0.01(\text{stat}).$$

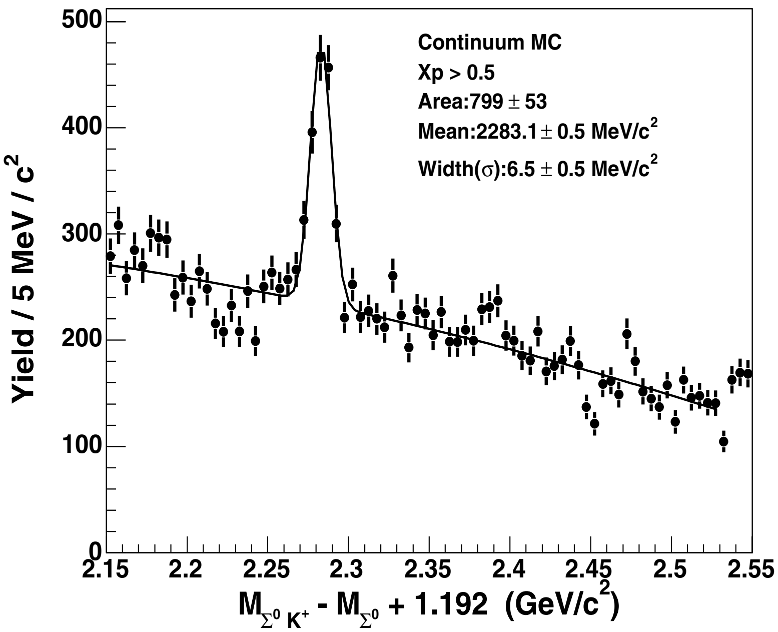

Figure 5.20: Invariant mass distribution for $\Lambda_c^+ \to \Sigma\ K^+$ from continuum MC, used to model the data.

5.4.2 Observation of $\Lambda_c^+ \to \Lambda K^+$

The first evidence of the Cabibbo-suppressed decay $\Lambda_c^+ \to \Lambda K^+$was published by BELLE collaboration in 2002 [33]: they found 265 events in the signal region. Reconstructing the ΛK^+combinations with the selection criteria described in section 5.2. A nice signal peak with much better statistics at the Λ_c^+ mass is shown in Figure 5.24. The mass distribution is fitted using a Gaussian with floating width for the signal and a second order polynomial for the background. The fit yields 1162 $\pm$ 101 (stat.) events; the fitted width $\sigma = 5.5 \pm 0.6$MeV/c^2 is consistent with the MC prediction of 6.0MeV/c^2.

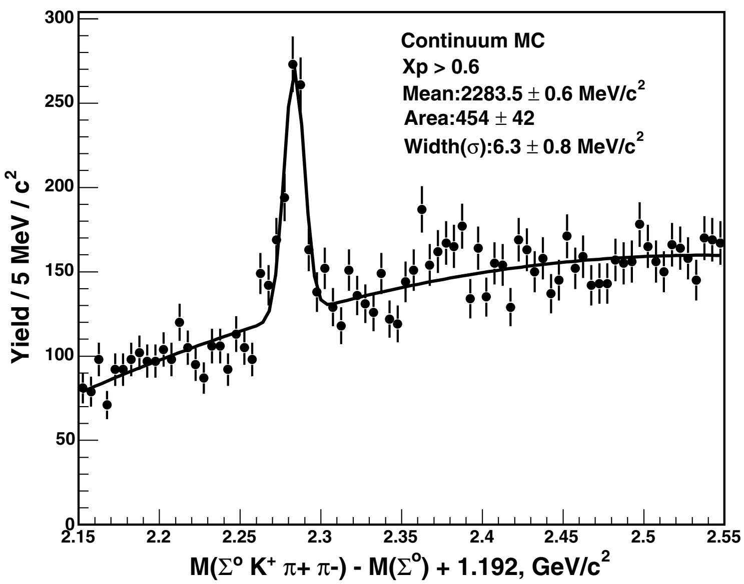

Figure 5.21: Invariant mass distribution for $(\Sigma^0 K^+\pi^+\pi^-)$ combinations from continuum MC. The excess yield above the smooth background is due to decays of Λ_c^+ into this final state, whose presence in this MC sample is attributable to Λ_c^+ decays being modelled with JETSET.

The relative detection efficiency ratio is found to be:

$$\frac{\epsilon(\Lambda_c^+ \to \Lambda K^+)}{\epsilon(\Lambda_c^+ \to \Lambda\pi^+)} = \frac{0.250}{0.313} = 0.80 \pm 0.01(\text{stat}).$$

5.4.3 Search for the $\Lambda_c^+ \to \Lambda K^+\pi^+\pi^-$

The Cabibbo-suppressed decay mode $\Lambda_c^+ \to \Lambda K^+\pi^+\pi^-$has never been observed before. Being a multi-body charged particle decay, it should be difficult to observe as the signal sits over a big combinatorial background. For this purpose one needs high statistics. *BABAR* provides this environment and a clear peak was seen in this

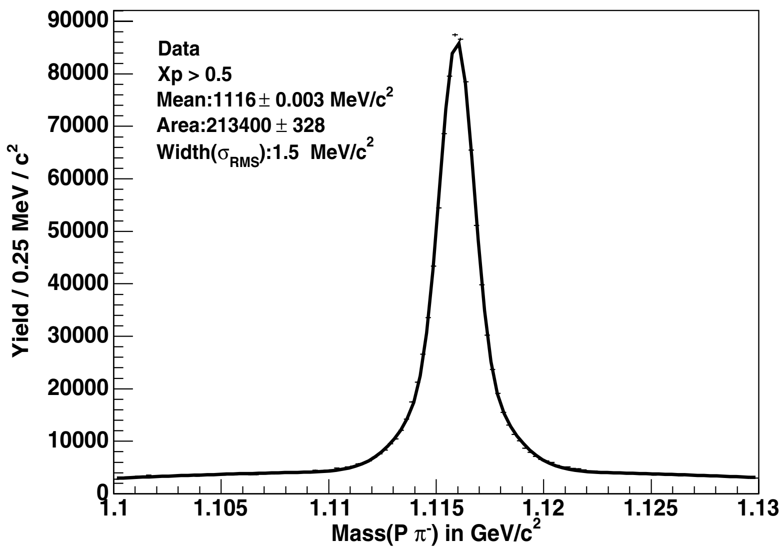

Figure 5.22: Mass distribution for $\Lambda \rightarrow p\pi^-$from data.

mode. The Λ_c^+ signal in this mode contains both resonant and non-resonant contributions to the $\Lambda_c^+ \rightarrow \Lambda K^+\pi^+\pi^-$. In order to reduce the large background in this Cabibbo-suppressed decay mode the PID for kaon and pions was tightened (using KLHVeryTight and PiLHVeryTight) coming from the Λ_c and also the limits for the scaled momentum was increased from $x_p > 0.5$ to $x_p > 0.6$. We use a Gaussian and a 2nd order polynomial to fit the signal and background respectively. The fit obtains a width (σ) 6.4 $\pm$ 0.2 MeV/c^2, where as the fit yields 3561 $\pm$ 132 (stat.), as shown in Figure 5.25. In order to see the contributions from different combinations of particles in the various decay modes of Λ_c^+ which results in $\Lambda K^+\pi^+\pi^-$ combinations. we analyze our data as a scatter plot with Λ_c^+ on the Y-axis versus the mass distribution for the $\Lambda\pi^-$ combination on the X-axis, as shown in Figure 5.26. Here we see a clear overlap at the crossing of the two bands for the two mass distributions.

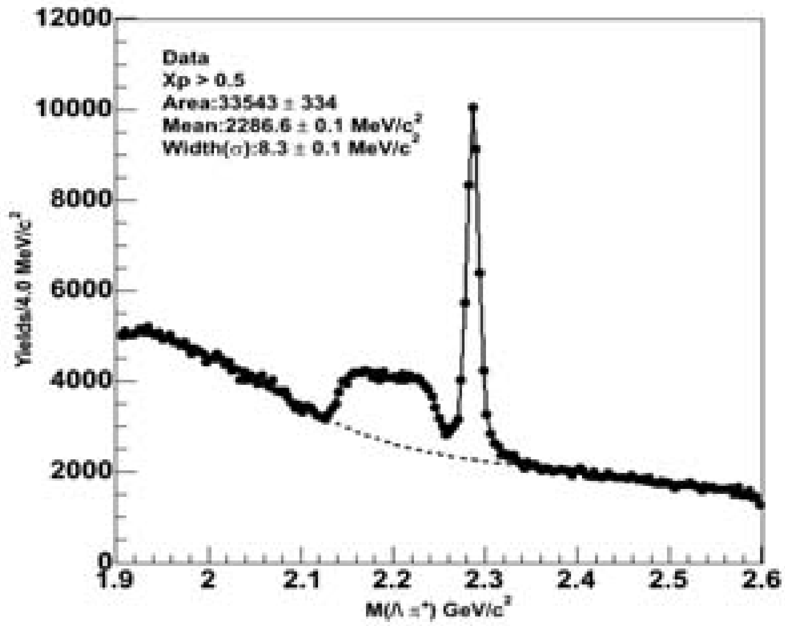

Figure 5.23: Mass distribution for $\Lambda_c^+ \to \Lambda\pi^+$from data at $x_p > 0.5$.

The population at the cross-section of the Λ_c^+ and $\Lambda\pi^-$ mass bands is seen at Ξ^- mass region.

The Figure 5.27 shows the invariant mass $\Lambda\pi^-$ in Λ_c^+ signal region after background subtraction. The background has been estimated from the side bands of Λ_c^+ mass distribution. The peak at Ξ^- mass region is a contribution from the Cabibbo-favored decay mode $\Lambda_c^+ \to \Xi^- K^+ \pi^+$. We reject this contribution from our Cabibbo-suppressed decay mode $\Lambda_c^+ \to \Lambda K^+ \pi^+ \pi^-$ by choosing $\pm$15MeV/c^2 Ξ^- mass window around the nominal value (which is $M_{\Xi^-} = 1321.3$MeV/c^2). The value for this mass window was choosen based on the $\Xi^- \to \Lambda\pi^-$ resolution prediction from the signal Monte Carlo (signal MC width(σ) = 6.0 MeV/c^2).

We also checked through the scatter plot for the mass distribution between Λ_c^+

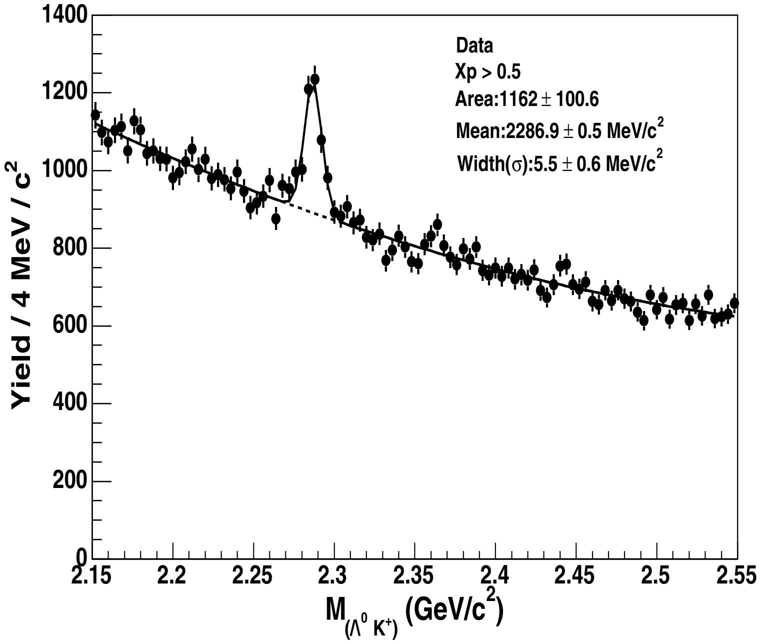

Figure 5.24: Mass distribution for $\Lambda_c^+ \to \Lambda K^+$from data.

from $\Lambda K^+\pi^+\pi^-$ along Y-axis and the mass distribution for $\pi^+\pi^-$combination along X-axis as shown in Figure 5.28. We see a clear overlap at the crossing of the two bands for the two mass distributions. The population at the cross-section of the Λ_c^+ and $\pi^+\pi^-$ mass bands is seen at the K_S^0 mass region.

Figure 5.29 shows the invariant mass $\pi^+\pi^-$ in Λ_c^+ signal region after backgraound subtraction. The background was estimated from the side band Λ_c^+ mass. The peak at K_S^0 mass region is a contribution from the Cabibbo-favored decay mode $\Lambda_c^+ \to \Lambda K_S^0 K^+$. We reject this contribution from our Cabibbo-suppressed decay mode $\Lambda_c^+ \to \Lambda K^+\pi^+\pi^-$ by choosing $\pm$10MeV/c^2 K_S^0 mass window around the nominal value (which is $M_{K_S^0} = 497.7$MeV/c^2). After rejecting the contributions from the above mentioned Cabibbo-allowed decays we plot the $\Lambda_c^+ \to \Lambda K^+\pi^+\pi^-$ mass dis-

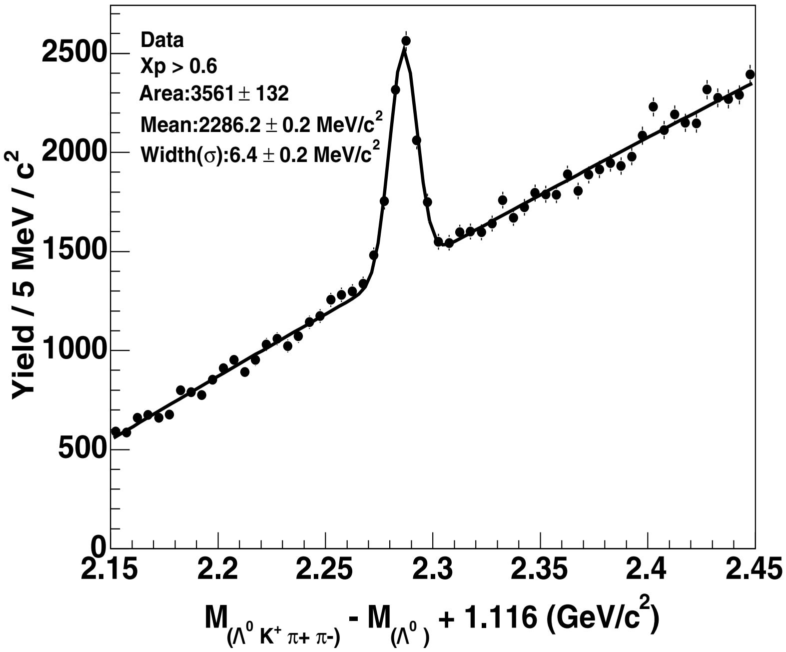

Figure 5.25: Invariant mass distribution for $\Lambda_c^+ \to \Lambda K^+ \pi^+ \pi^-$ from data.

tribution as shown in Figure 5.31. We use a single Gaussian with, mean: 2285.0 MeV/c^2 and width (σ): 5.2 MeV/c^2 fixed to the signal MC, and a 2nd order polynomial to fit the background shape for $\Lambda_c^+ \to \Lambda K^+ \pi^+ \pi^-$. The fit yields: 201 $\pm$ 64 Λ_c^+.

The relative detection efficiency is found to be:

$$\frac{\epsilon(\Lambda_c^+ \to \Lambda K^+ \pi^+ \pi^-)}{\epsilon(\Lambda_c^+ \to \Lambda \pi^+)} = \frac{0.111}{0.321} = 0.35 \pm 0.01(\text{stat}).$$

In this case the normalization mode ($\Lambda_c^+ \to \Lambda \pi^+$) also uses the scaled momentum spectrum $x_p > 0.6$. The fit for the normalization mode yields: 22204.4 ± 256.7 (stat.) as shown in Figure 5.30.

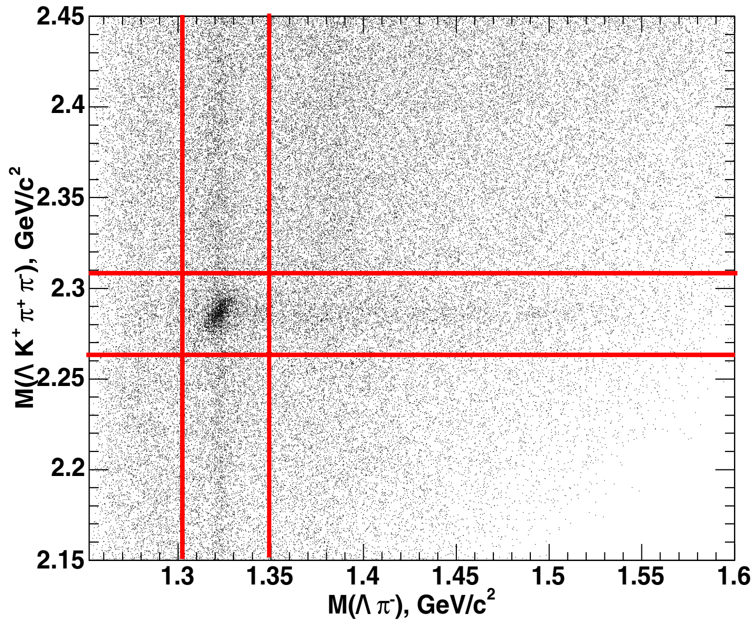

Figure 5.26: Two dimensional Invariant mass distribution for $\Lambda_c^+ \to \Lambda K^+ \pi^+ \pi^-$ and $\Lambda\pi^-$combination from data.

5.4.4 $\Lambda_c^+ \to \Xi^- K^+ \pi^+$ and $\Lambda_c^+ \to \Lambda \overline{K^0} K^+$

Since our Cabibbo-suppressed decay mode has major contributions from the these two Cabibbo-favored decays, we have plotted the Λ_c^+ from the contributing Cabibbo-allowed decay modes $\Lambda_c^+ \to \Xi^- K^+ \pi^+$ and $\Lambda_c^+ \to \Lambda \overline{K^0} K^+$ for the chosen Ξ^- mass windows (which is ± 15 MeV/c^2). We see a peak in the Λ_c^+ mass region which comes from $\Xi^- K^+ \pi^+$, $\Xi^- \to \Lambda \pi^-$, we use a single Gaussian to fit the signal region and 2nd order polynomial to fit the background shape. The fit yields: 2665 ± 84 Λ_c^+'s decaying to $\Xi^- K^+ \pi^+$ and the width(σ) comes out to be: 6.6 ± 0.2 MeV/c^2, as illustrated in Figure 5.32.

The Cabibbo-allowed decay mode $\Lambda_c^+ \to \Lambda \overline{K^0} K^+$ was plotted using the chosen

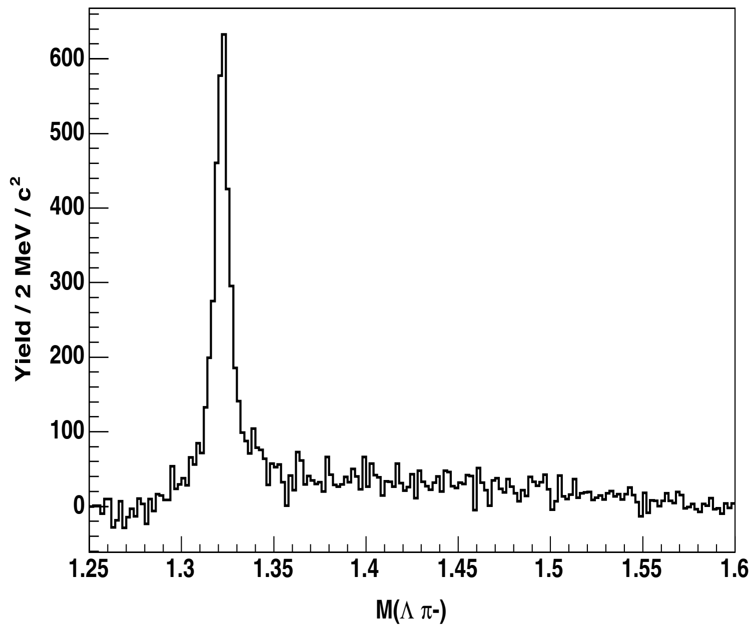

Figure 5.27: Invariant mass distribution for $\Xi^- \to \Lambda\pi^-$, when plotted from Λ_c^+ signal region and side-band subtracted from data.

K_S^0 mass window (which is ± 10 MeV/c^2). We use a single Gaussian to fit the signal region and a 2nd order polynomial to fit the background for this Λ_c^+ mass distribution. The fit yields: 460 ± 30 Λ_c^+ decaying to $\Lambda\overline{K^0}K^+$ and width (σ) comes out to be: 5.5 ± 0.4 MeV/c^2, as shown in Figure 5.33.

This gives us a motivation to include these measurements in our analysis. So we find the relative effeciency for the $\Lambda_c^+ \to \Xi^- K^+ \pi^+$ to that relative to $\Lambda_c^+ \to \Lambda\pi^+$ as:

$$\frac{\epsilon(\Lambda_c^+ \to \Xi^- K^+ \pi^+)}{\epsilon(\Lambda_c^+ \to \Lambda\pi^+)} = \frac{0.088}{0.321} = 0.274 \pm 0.003(\text{stat}).$$

For the Cabibbo-favored contribution $\Lambda_c^+ \to \Lambda K_S^0 K^+$ relative to that of $\Lambda_c^+ \to \Lambda\pi^+$ the relative effeciency is:

$$\frac{\epsilon(\Lambda_c^+ \to \Lambda K_S^0 K^+)}{\epsilon(\Lambda_c^+ \to \Lambda\pi^+)} = \frac{0.054}{0.321} = 0.168 \pm 0.020(\text{stat}).$$

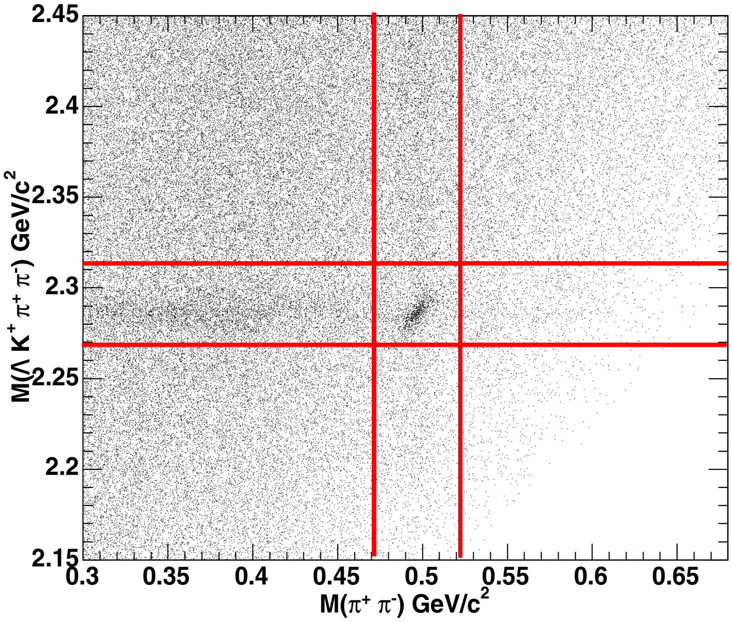

Figure 5.28: Two dimensional Invariant mass distribution for $\Lambda_c^+ \to \Lambda K^+ \pi^+ \pi^-$ and $\pi^+\pi^-$combination from data.

5.4.5 Observation of the $\Lambda_c^+ \to \Sigma^0 \pi^+$

As stated earlier in section 5.2, we will be using $\Lambda_c^+ \to \Sigma^0 \pi^+$ as a normalization mode for the decay modes involving Σ^0 in the final state, where $\Sigma^0 \to \Lambda\gamma$, $\Lambda \to p\pi^-$. We first reconstruct $\Sigma^0 \to \Lambda\gamma$, using already reconstructed $\Lambda \to p\pi^-$, as discussed in detail in section 5.2. We use $\Sigma^0 - \Lambda$ mass difference to reconstruct Λ_c^+ with $\pm$10MeV/c^2 mass window (2.5σ) around $M_{\Sigma^0} - M_{\Lambda}$ invariant mass, which is 77.6 MeV/c^2, as illustrated in Figure 5.34. For $\Lambda_c^+ \to \Sigma^0 \pi^+$, the fit uses a Gaussian and 3rd order polynomial for signal and background, respectively. Fit yields 12490 ± 162 (stat.): $\Lambda_c^+ \to \Sigma^0$ π^+ with floated width (σ): 6.7 ± 0.1 MeV/c^2 which is consistent with our signal Monte Carlo width (σ): 7.0MeV/c^2;as shown in figure 5.35.

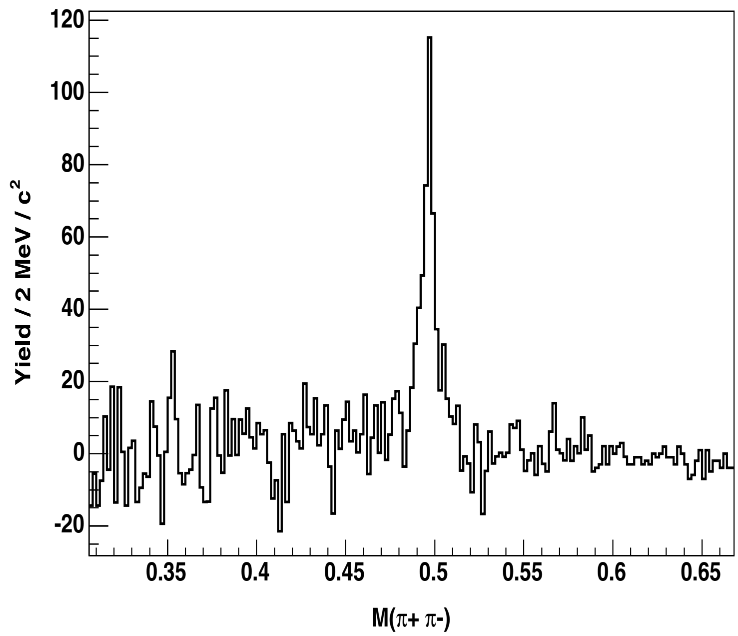

Figure 5.29: Invariant mass distribution for $K_S^0 \rightarrow \pi^+\pi^-$, when plotted from Λ_c^+ signal region and side-band subtracted as well as Ξ^- rejected from data.

5.4.6 Observation of the $\Lambda_c^+ \rightarrow \Sigma^0 K^+$

The Cabibbo-suppressed decay $\Lambda_c^+ \rightarrow \Sigma^0\ K^+$, Figure 5.36, was first observed by the BELLE collaboration in 2002 [33] with 70 events in the signal region at $x_p > 0.6$. Here we measure this decay mode with much better statistics at $x_p > 0.5$. Figure 5.36 shows the invariant mass distribution for the $\Lambda_c^+ \rightarrow \Sigma^0\ K^+$ combination selected according to selection criteria described in section 5.2. A clear peak is seen at Λ_c^+ mass. Fit for this distribution uses a Gaussian (with width (σ) fixed to our MC prediction of 6.0 MeV/c^2) plus a 3rd order polynomial to fit the signal and the background shape: the fit yields 375.6 $\pm$ 44.5 (stat.) $\Lambda_c^+ \rightarrow \Sigma^0\ K^+$ events.

For normalization mode, we reconstruct the $\Lambda_c^+ \rightarrow \Sigma^0\ \pi^+$ decay mode with equiv-

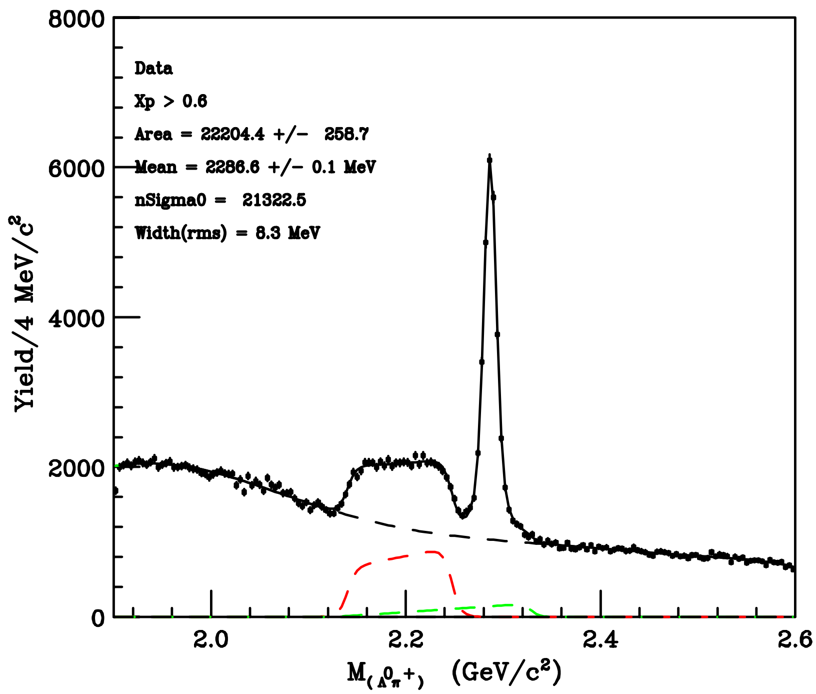

Figure 5.30: Mass distribution $\Lambda_c^+ \to \Lambda\pi^+$from data for $x_p > 0.6$.

alent cuts, as shown in Figure 5.35. The relative detection efficiency for $\Lambda_c^+ \to \Sigma^0$ K^+ decay to that of $\Lambda_c^+ \to \Sigma^0$ π^+ decay was measured as:

$$\frac{\epsilon(\Lambda_c^+ \to \Sigma^0 K^+)}{\epsilon(\Lambda_c^+ \to \Sigma^0 \pi^+)} = \frac{0.095}{0.119} = 0.80 \pm 0.01(\mathrm{stat}).$$

5.4.7 Search for the $\Lambda_c^+ \to \Sigma^0$ $K^+\pi^+\pi^-$

The Cabibbo-suppressed decay mode $\Lambda_c^+ \to \Sigma^0$ $K^+\pi^+\pi^-$has never been observed before. We reconstructed Λ_c^+ in this decay mode using the Σ^0 selection criteria described in section 5.2. We combined already selected Σ^0 with a K^+ , a π^+ and a π^-. We did not see the Λ_c^+ signal in this decay mode, using almost $125 fb^{-1}$ of available data, Figure 5.37. We fit the distribution by fixing mass and the width (σ) to our

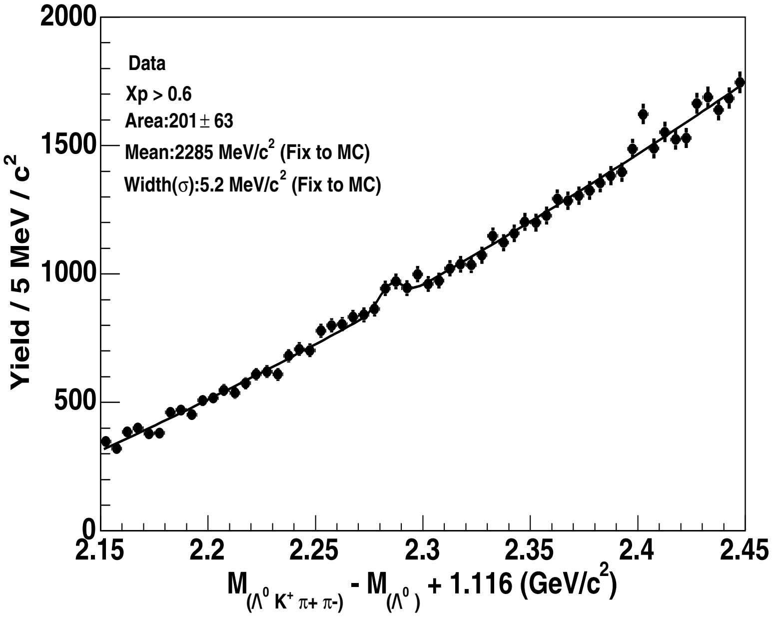

Figure 5.31: Invariant mass distribution for $\Lambda_c^+ \to \Lambda K^+\pi^+\pi^-$ from data after rejection from the contributing Cabibbo-favored decays of Λ_c^+ as mentioned above.

signal MC predictions for this mode: 2285.0 MeV/c^2 and 4.4 MeV/c^2, respectively. Fit yields 20.7 ± 23.7 (stat.) Λ_c^+ decaying to Σ^0 $K^+\pi^+\pi^-$.

In this case we use $\Lambda_c^+ \to \Sigma^0\pi^+$ as the normalization mode at $x_p > 0.6$. The fit yields: 8848 ± 125.6 (stat.) Λ_c^+ candidates for the normalization mode. We found the relative reconstruction efficiency:

$$\frac{\epsilon(\Lambda_c^+ \to \Sigma^0 K^+\pi^+\pi^- \ )}{\epsilon(\Lambda_c^+ \to \Sigma^0\pi^+)} = \frac{0.053}{0.125} = 0.42 \pm 0.01(\mathrm{stat}).$$

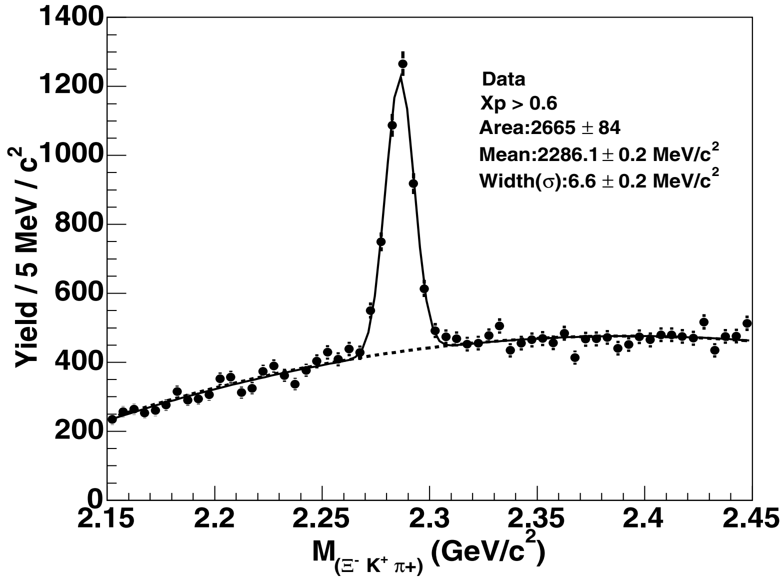

Figure 5.32: Invariant mass distribution for $\Lambda_c^+ \to \Xi^- K^+ \pi^+$ with $\overline{K^0}$rejection to this mode, which constitutes a major contribution to our Cabibbo-suppressed decay mode $\Lambda_c^+ \to \Lambda K^+ \pi^+ \pi^-$ from data.

5.5 Summary tables of the Cuts used

In this section, we summarize our selection cuts used for the Λ_c^+ in $\Lambda\pi^+$, ΛK^+, $\Lambda K^+\pi^+\pi^-$ and Σ^0 π^+, Σ^0 K^+ , Σ^0 $K^+\pi^+\pi^-$modes, as shown in tables[5.8 , 5.10]. We also include the summary table 5.9 for the two Cabibbo-favored decay modes: $\Lambda_c^+ \to \Xi^- K^+ \pi^+$, $\Lambda_c^+ \to \Lambda \overline{K^0} K^+$, which presents resonant Cabibbo-favored backgrounds to our Cabibbo-suppressed mode $\Lambda_c^+ \to \Lambda K^+ \pi^+ \pi^-$

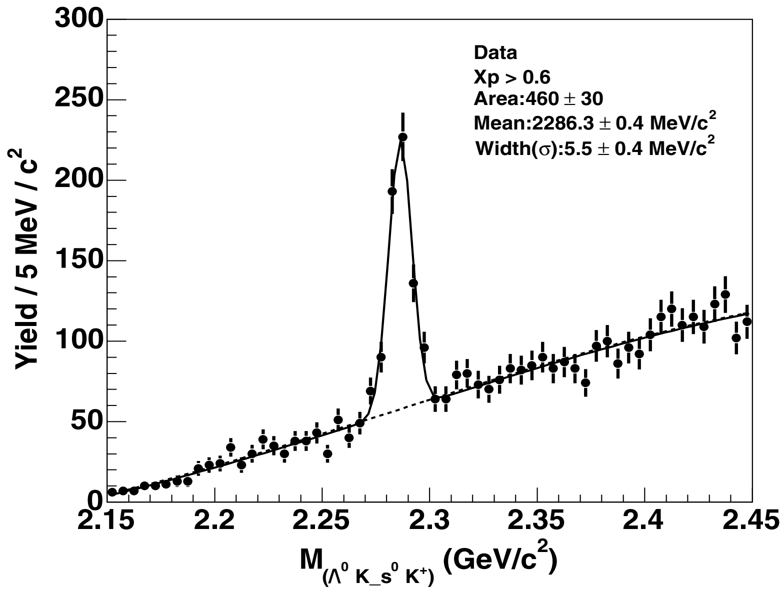

Figure 5.33: Invariant mass distribution for $\Lambda_c^+ \to \Lambda \overline{K^0} K^+$, which is contributing to our Cabibbo-suppressed decay mode $\Lambda_c^+ \to \Lambda K^+ \pi^+ \pi^-$ from data.

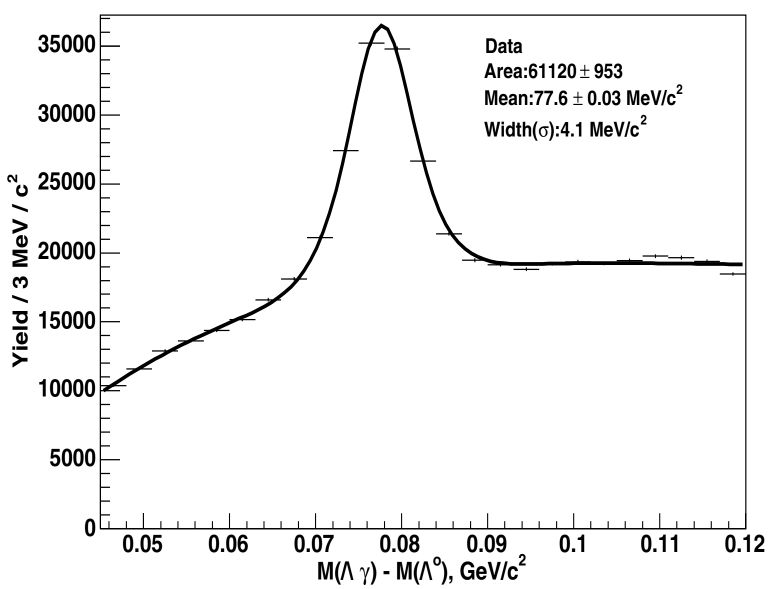

Figure 5.34: Mass plot for M($\Lambda\gamma$) - M(Λ) distribution from data.

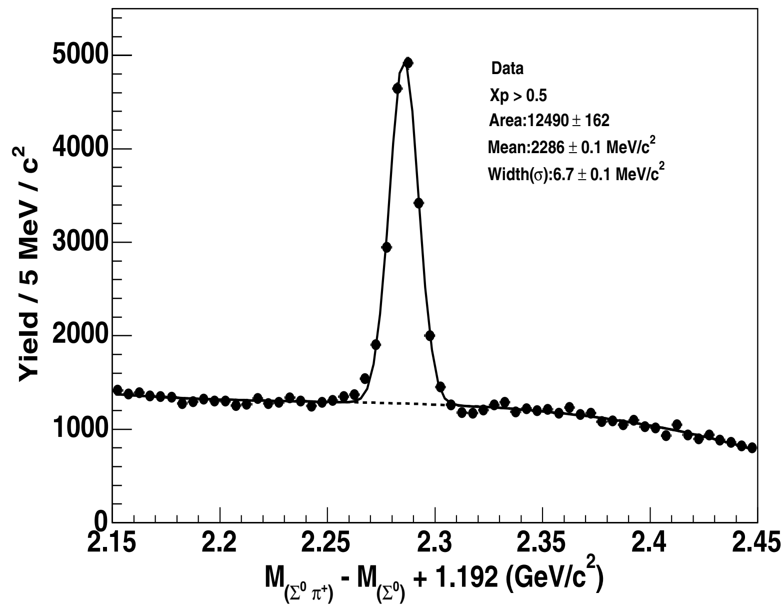

Figure 5.35: Invariant mass distribution for $\Lambda_c^+ \rightarrow \Sigma\ \pi^+$ from data.

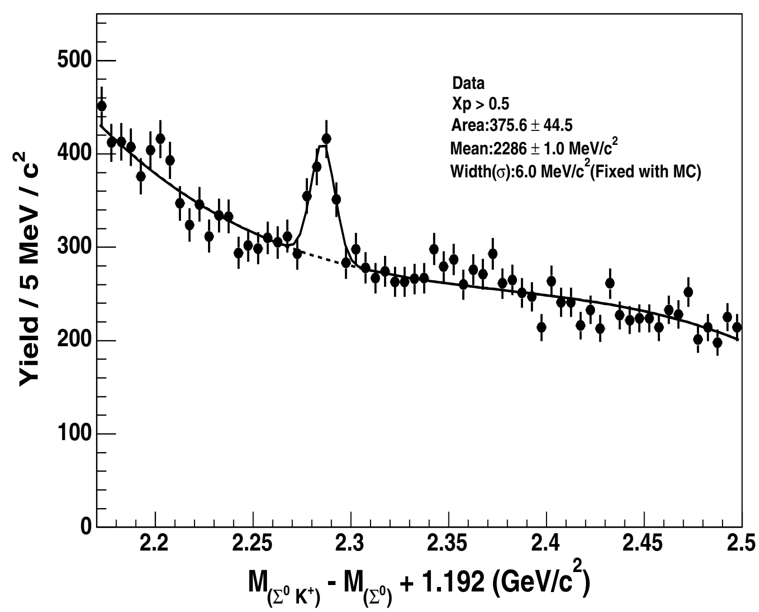

Figure 5.36: Invariant mass distribution for $\Lambda_c^+ \rightarrow \Sigma^0\ K^+$ from data.

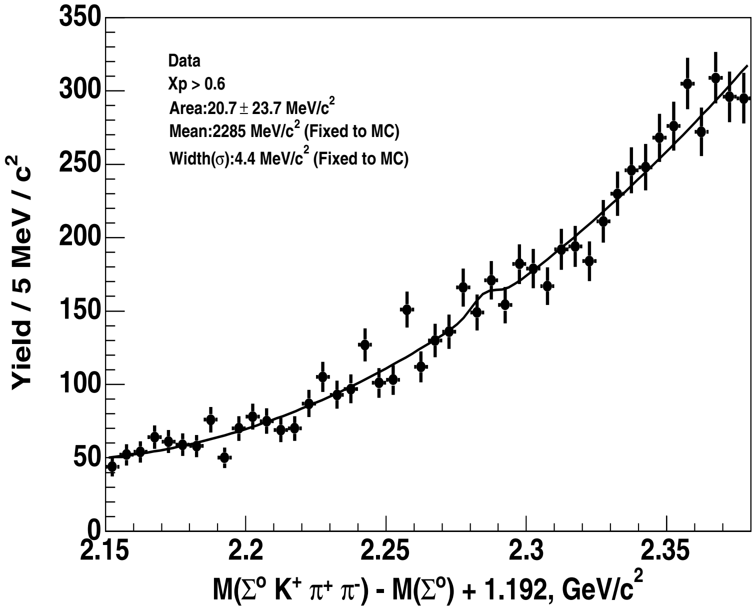

Figure 5.37: Invariant mass distribution for $\Lambda_c^+ \to \Sigma^0\ K^+\pi^+\pi^-$ from data. A signal in not recognizable and a fitted yield is consistent with zero.

Table 5.8: Summary table of selection criteria used in our selection criteria for the decay modes involving Λ as one of the final state.

	Cuts used	$\Lambda_c^+ \to \Lambda\pi^+$	$\Lambda_c^+ \to \Lambda K^+$	$\Lambda_c^+ \to \Lambda K^+\pi^+\pi^-$
1	M_Λ Window	$\pm 2\sigma$	$\pm 2\sigma$	$\pm 2\sigma$
2	$P_{\chi^2_{\Lambda_{vertex}}}$	$> 0.1\%$	$> 0.1\%$	$> 0.1\%$
3	Λ flight cut(r) 3-D	0.2 cm	0.2 cm	0.2 cm
4	M_{Ξ^-} window	-	-	$\pm$15MeV/c^2
5	$M_{K_S^0}$ window	-	-	$\pm$10MeV/c^2
6	$\epsilon(\%)$	31.2 ± 0.2(stat)	25.0 ± 0.2(stat)	11.1 ± 0.1(stat)
7	Yield	33543 ± 334	1162 ± 100.6	201 ± 64
8	Fitted Mean Value	2286.6 ± 0.1 MeV/c^2	2287.0 ± 1.0 MeV/c^2	2285.0 MeV/c^2(Fixed)

Table 5.9: Summary table of selection criteria for the Cabibbo-favored decay modes of Λ_c^+ to $\Xi^- K^+ \pi^+$ and $\Lambda_c^+ \to \Lambda \overline{K^0} K^+$ as described in Section 6.3.

	Cuts used	$\Lambda_c^+ \to \Xi^- K^+ \pi^+$	$\Lambda_c^+ \to \Lambda \overline{K^0} K^+$
1	M_Λ Window	$\pm 2\sigma$	$\pm 2\sigma$
2	$P_{\chi^2_{\Lambda_{vertex}}}$	$> 0.1\%$	$> 0.1\%$
3	Λ flight cut(r) 3-D	0.2 cm	0.2 cm
4	M_{Ξ^-} window	$\pm$15MeV/c^2	$\pm$15MeV/c^2
5	$M_{K_S^0}$ window	$\pm$10MeV/c^2	$\pm$10MeV/c^2
6	$\epsilon(\%)$	8.8 ± 0.1(stat)	5.4 ± 0.2(stat)
7	Yield	2665 ± 84	460 ± 30
8	Fitted Mean Value	2286.1 ± 0.2 MeV/c^2	2286.3 ± 0.4 MeV/c^2

Table 5.10: Summary table for cuts used in our selection criteria for the decay modes involving Σ^0 as one of the final state.

	Cuts used	$\Lambda_c^+ \to \Sigma^0\ \pi^+$	$\Lambda_c^+ \to \Sigma^0\ K^+$	$\Lambda_c^+ \to \Sigma^0\ K^+ \pi^+ \pi^-$
1	$M_{(\Sigma^0 - \Lambda)}$ Window	$\pm 2.5\sigma$	$\pm 2.5\sigma$	$\pm 2.5\sigma$
2	E_γ(MeV)	> 100	> 100	> 100
3	$\epsilon(\%)$	11.9 ± 0.1(stat)	9.5 ± 0.1(stat)	5.4 ± 0.1(stat)
4	Yield	12490 ± 162	375.6 ± 44.5	20.7 ± 23.7
5	Fitted Mean Value	2286.0 ± 0.1MeV/c^2	2286.0 ± 1.0MeV/c^2	2285.0MeV/c^2 (Fixed)

5.6 Systematic uncertainties

The systematic uncertainties for this analysis are categorized as follows:

1. Monte Carlo Statistics.
2. Λmass cut.
3. Probability of $\chi^2_{\Lambda vertex}$ cut.
4. Λ flight cut(r) 3-D.
5. x_p cut.
6. E_γ cut.
7. Ξ^-mass window cut for $\Lambda_c^+ \to \Xi^- K^+ \pi^+$ rejection from $\Lambda_c^+ \to \Lambda K^+ \pi^+ \pi^-$.
8. K_S^0mass window cut for $\Lambda_c^+ \to \Lambda \overline{K^0} K^+$ rejection from $\Lambda_c^+ \to \Lambda K^+ \pi^+ \pi^-$.
9. Ξ^- and K_S^0 vertexing.
10. Ξ^- and K_S^0 branching ratio
11. Fitting.
12. MC Modeling for $\Lambda_c^+ \to \Lambda K^+ \pi^+ \pi^-$, $\Lambda_c^+ \to \Sigma^0 \; K^+ \pi^+ \pi^-$
13. PID efficiency.
14. Tracking resolution.
15. Adding On and Off Resonance data

Values for these uncertainties are summarized in tables 5.12, 5.13 & 5.15.

5.6.1 MC Statistics

Due to the MC statistics, the uncertainty in the detection efficiency has been considered.

5.6.2 Λ Mass Cut

The uncertainty due to the Λ mass cut has been considered. All of our decay modes involve Λ in the final state either directly(the decay modes having Λ in the final state) or indirectly (decay modes involving Σ^0 in the final state, where $\Sigma^0 \rightarrow \Lambda\gamma$). Here We change the Λ mass window from $\pm 2\sigma$, where $\sigma = 1.5$MeV/c^2, to $\pm 3\sigma$ and take into account the uncertainty due to this change. This uncertainty has been presented in tables 5.12,5.13 for each decay mode.

5.6.3 Probability of $\chi^2_{\Lambda\ vertex}$ cut

Throughout this analysis we have used the probability of $\chi^2_{\Lambda\ vertex}$ cut, being part of the Λ selection. Although all our decay modes use the same cut (probability of $\chi^2_{\Lambda\ vertex}$ to be greater than 0.1%), But the uncertainty due to the different decay modes, which might have different Λ momentum, have been considered by tightening the value of probability of $\chi^2_{\Lambda\ vertex}$ and also by relaxing it. The uncertainty due to this variation is summarized in tables 5.12,5.13 for each decay mode.

5.6.4 Λ flight cut (r) 3-D

This cut is also part of our Λ selection. We are using the same Λ selection through out this analysis. It can be expected that the Λ momentum spectra might be different for different decay modes, therefore we also take into account the uncertainty due to this cut. We have tightened the value of the Λ flight cut(r) from 0.2cm (which is our chosen value) to 0.4cm and also by removing this cut and then calculated this uncertainty, which is listed in tables 5.12, 5.13 for each decay mode.

5.6.5 x_p cut

The background coming from combinatorial and $B\overline{B}$ was suppressed using this cut. We use the same value of the cut for all of the two body decay modes involved in this analysis (which is $x_p > 0.5$). While for the decay modes $\Lambda_c^+ \to \Lambda K^+\pi^+\pi^-$ and for $\Lambda_c^+ \to \Sigma^0\ K^+\pi^+\pi^-$, where we have used $x_p > 0.6$, even the normalization modes corrsponding to these decays also use the same cut of $x_p > 0.6$. By considering the fact that momentum spectrum for the decay products depend on the decay mode, we consider this effect by varying x_p cut slightly from the chosen value, for all the decay modes and the effect of this variation has been taken into account as a systematic uncertainty, which is summarized in tables 5.12,5.13.

5.6.6 E_γ cut

Although all the decay modes involving Σ^0 in the final state uses the same value of E_γ cut, as our selection for $\Sigma^0 \to \Lambda\gamma$ is same for all the decay modes, but we consider the fact that the Σ^0 momentum and so do the γ energy spectrum might differ for different decay modes. Therefore we assign the uncertainty due to this cut as mentioned in tables 5.12,5.13, by varying the γ energy cut around the chosen value (which is 100 MeV).

5.6.7 Ξ^- mass window cut for $\Lambda_c^+ \to \Xi^- K^+ \pi^+$ rejection from $\Lambda_c^+ \to \Lambda K^+ \pi^+ \pi^-$

Since the final state of our Cabibbo-suppressed decay mode can also appear in the decay chain of Cabibbo-favored mode $\Lambda_c^+ \to \Xi^- K^+ \pi^+$ as discussed in detail in Section 5.4. We reject this contribution from $\Lambda_c^+ \to \Lambda K^+ \pi^+ \pi^-$ by choosing a Ξ^- mass rejection window, which is $\pm$ 15 MeV around the nominal Ξ^-mass. We vary this value by opening up the mass window to a wider range and any change in the $\Lambda_c^+ \to \Lambda K^+ \pi^+ \pi^-$ fitting yield has been taken into account as a systematic uncertainty, which is presented in the table 5.12.

5.6.8 K_S^0 mass window cut for $\Lambda_c^+ \to \Lambda \overline{K^0} K^+$ rejection from $\Lambda_c^+ \to \Lambda K^+ \pi^+ \pi^-$.

As discussed earlier in section 5.4, in detail, and shown in Figures 5.28 and 5.29, that the Cabibbo-suppressed decay mode $\Lambda_c^+ \to \Lambda K^+ \pi^+ \pi^-$ has also a reasonable contribution from the Cabibbo-favored decay mode $\Lambda_c^+ \to \Lambda \overline{K^0} K^+$. We remove this contribution from $\Lambda_c^+ \to \Lambda K^+ \pi^+ \pi^-$ by choosing $\pm$ 10 MeV $\overline{K^0}$ mass window around its nominal value and rejecting Λ_c's this way coming from $\Lambda_c^+ \to \Lambda \overline{K^0} K^+$ mode.

We vary this value by opening up the $\overline{K^0}$ mass window to a wider range and any change in the $\Lambda_c^+ \to \Lambda K^+ \pi^+ \pi^-$ fitting area (Yield) has been considered as a systematic uncertainty for this mode. This value is shown in the table 5.12.

5.6.9 Ξ^- and K^0_S vertexing

Since our Cabibbo-suppressed decay mode $\Lambda_c^+ \to \Lambda K^+ \pi^+ \pi^-$ has major contributions from the two cabibbo-favored modes: $\Lambda_c^+ \to \Xi^- K^+ \pi^+$ and $\Lambda_c^+ \to \Lambda K^0_S$. Figures 5.32 and 5.33 show significant contributions from these 2 decay modes. This also gives us a motivation to calculate the relative branching ratios for these modes relative to that of the cabibbo-favord modes $\Lambda_c^+ \to \Lambda \pi^+$. Since vertexing was not used for the reconstruction of Ξ^- and K^0_S, we assign a systematic uncertainty due to vertexing for Ξ^- and K^0_S reconstruction.

We used our signal MC for the $\Lambda_c^+ \to \Xi^- K^+ \pi^+$ inorder to study this effect for Ξ^-. Any change in the detection efficiency for this mode with and with out vertexing the Ξ^- is taken into account as a source of systematic uncertainty. Similar procedure is applied for the K^0_S, where we used our signal MC for the $\Lambda_c^+ \to \Lambda K^0_S \pi^+$ decay to study this effect.

In order to cross-check for the vertexing effect, we also used our normalization mode $\Lambda_c^+ \to \Lambda \pi^+$, where we study this effect for the Λ with and without vertexing. Here we also studied the effect for tracking by changing the tracks from `GoodTrackVeryLoose` to `ChargedTracks` for the Λ. This was done using 90fb^{-1} of data for this decay mode. We assign a systematic uncertainty of 2% due to this effect and a systematic uncertainty of 4.5% was assigned due to vertexing effect. The over all uncertainty of 5.0% is assigned due to vertexing as well as the tracking effects for the Ξ^- and K^0_S reconstructions. These values are tabulated in the table 5.7.

5.6.10 Ξ^- and K_S^0 branching ratios

For our relative branching ratio measurements $\Lambda_c^+ \to \Xi^- K^+ \pi^+$ and $\Lambda_c^+ \to \Lambda K_S^0 K^+$ relative to that of $\Lambda_c^+ \to \Lambda \pi^+$, we take into account for the branching ratios due to $\Xi^- \to \Lambda \pi^-$ and $K_S^0 \to \pi^+ \pi^-$. Systematic uncertainty of 3.5% and 1.0% comes due to the branching ratios [35] of $\Xi^- \to \Lambda \pi^-$ and $K_S^0 \to \pi^+ \pi^-$ respectively, as shown in table 5.7.

5.6.11 Fitting

Possible biases due to fitting procedure have been studied. In each fit, the shape of the background function has been varied by changing the order of the polynomial function as well as varying the widths and Mean within the error obtained from the MC and also fixing these according to the Monte Carlo predictions for the corresponding decay modes, with any change in the signal yield being taken as a systematic uncertainty. We also study the fitting procedure for $\Lambda_c^+ \to \Lambda \pi^+$, which is one of our normalization mode and has a complicated fit. This fit uses 19 parameters, so we vary all these parameters arround the central values with in the error, which were taken from our continuum MC fit (which was used to study the backgraound shape as well as for the optimization of our cuts for this decay mode and all the others involved in this analysis). The fit for $\Lambda_c^+ \to \Lambda \pi^+$ takes two Gaussian with the same mean for the signal and two square wave functions smeared with the Λ_c^+ resolution function, for the two reflection around the Λ_c^+ signal region and a 7th order polynomial for the backgound. This fit has already been explained in detail in sections 5.3.6 and 5.4. We are considering the uncertainty due to all the parameters involved in this fit. Of course the uncertainty due to the fitting parameter in all other decay modes is also being considered. For the fit where the width of the signal Gaussian was fixed to the MC prediction (e.g; $\Lambda_c^+ \to \Sigma^0 K^+$, $\Lambda_c^+ \to \Lambda K^+\pi^+\pi^-$ and $\Lambda_c^+ \to \Sigma^0 K^+\pi^+\pi^-$), we have redone the fit with a floating width, and taken the resulting change in the yield as a systematic uncertainty. This uncertainty for different modes is listed in tables 5.12, 5.13.

5.6.12 MC Modeling for $\Lambda_c^+ \to \Lambda K^+\pi^+\pi^-$, $\Lambda_c^+ \to \Sigma^0\ K^+\pi^+\pi^-$

We have also investigated the uncertainties due to MC Modeling for the decay modes $\Lambda_c^+ \to \Lambda K^+\pi^+\pi^-$ and $\Lambda_c^+ \to \Sigma^0\ K^+\pi^+\pi^-$. Here we check Λ_c efficiency as a function of M($K^+\pi^+\pi^-$) , M($\pi^+\pi^-$) and M($K^+\pi^-$). We assign the systematic unsertainty due to this effect to be: 5.4%, as shown tables 5.12, 5.15.

5.6.13 PID efficiency

We use the available PID tables to incorporate efficiency and misidentification rate for various particle identification selector lists used in this analysis. These are measured using control data samples and are tabulated in bins of momentum, polar and azimuthal angles [39]. These tables are provided by the PID group in *BABAR*. These PID tables also provides the efficiency uncertainty for each bin due to limited statistics of control data samples. Using these tables and assuming the errors in different bins are uncorrelated, we smear the efficiency and misidentification and re-evaluate our signal efficiencies as shown in tables 5.12, 5.13, 5.15 and the table 5.11 describes the PID efficiencies for the pion and kaon.

Table 5.11: Summary table for PID efficiencies.

Particle	Loose	Tight
Pion	99.5%	96.0%
Kaon	97.0%	97.3%

5.6.14 Tracking

We also consider the possible tracking resolution differences between the MC and data. We expect this uncertainty to be cancelled out in the case of $\Lambda_c^+ \to \Lambda K^+$ to $\Lambda_c^+ \to \Lambda \pi^+$, where we have assigned track in-efficiency as 1.4% per track. Whereas for $\Lambda_c^+ \to \Lambda K^+ \pi^+ \pi^-$ and $\Lambda_c^+ \to \Sigma^0\ K^+ \pi^+ \pi^-$, this in-efficiency has been assigned to be 1.4% per track [40]. So the systematic uncertainty for these decay modes have been taken into account and are mentioned in tables 5.12, 5.13 & 5.15.

5.6.15 Adding On- and Off-Resonance data

To the on-resonance data we added the off-resonance data, which has been recorded from collisions in the center of mass $\sim 40\,\mathrm{MeV}$ below the $\Upsilon(4S)$. So the cross-section difference due to the difference in energy is less than 1.0%.

The off- and the on-resonance data was added for the measured as well as to the normalization mode. This effect for the uncertainty is negligible.

5.7 Summary tables for the sources of systematic uncertainty

We summarize all of the above mentioned sources of systematic uncertainties in the following tables:

Table 5.12: Summary table and source of systematic uncertainties for the decay modes involving Λ in the final state.

Sources of Syst. error	$\frac{\mathcal{B}(\Lambda_c^+ \to \Lambda K^+)}{\mathcal{B}(\Lambda_c^+ \to \Lambda \pi^+)}$	$\frac{\mathcal{B}(\Lambda_c^+ \to \Lambda K^+ \pi^+ \pi^-)}{\mathcal{B}(\Lambda_c^+ \to \Lambda \pi^+)}$
Monte Carlo Statistics	1.1%	1.9%
Λmass cut	0.6%	0.1%
$P_{\chi^2_{\Lambda\ vertex}}$ cut	3.8%	0.7%
Λ flight cut(r) 3-D	0.7%	2.8%
x_p cut	0.7%	1.8%
Ξ^-Mass window	-	1.5%
$\overline{K}^0$Mass window	-	0.8%
Fitting	5.9%	4.7%
MC Modeling	-	5.4%
ϵ_{Ratio}	0.80	0.35
ϵ_{Ratio} (PID Corrected)	0.78	0.31
Tracking	-	2.8%
Total Systematic error	6.2%	9.5%

Table 5.13: Summary table and source of systematic uncertainties for the decay modes involving Σ^0 in the final state.

Sources of Syste. error	$\frac{\mathcal{B}(\Lambda_c^+ \to \Sigma^0 K^+)}{\mathcal{B}(\Lambda_c^+ \to \Sigma^0 \pi^+)}$
Monte Carlo Statistics	1.6%
Λmass cut	1.2%
$P_{\chi^2_{\Lambda\ vertex}}$ cut	0.9%
Λ flight cut(r) 3-D	1.9%
$M_{\Sigma^0 - \Lambda}$ mass cut	1.3%
x_p cut	2.1%
E_γ cut	0.9%
Fitting	8.0%
ϵ_{Ratio}	0.80
ϵ_{Ratio} (PID Corrected)	0.78
Tracking	-
Total Systematic error	8.9%

Table 5.14: Summary table and source of systematic uncertainties for the decay modes of Λ_c^+ to $\Xi^- K^+\pi^+$ and $\Lambda\overline{K^0}K^+$ in the final state.

Sources of Syste. error	$\frac{\mathcal{B}(\Lambda_c^+\to\Xi^- K^+\pi^+)}{\mathcal{B}(\Lambda_c^+\to\Lambda\pi^+)}$	$\frac{\mathcal{B}(\Lambda_c^+\to\Lambda\overline{K^0}K^+)}{\mathcal{B}(\Lambda_c^+\to\Lambda\pi^+)}$
Monte Carlo Statistics	2.0%	2.1%
Λmass cut	1.1%	0.1%
$P_{\chi^2_{\Lambda\ vertex}}$ cut	0.7%	0.7%
Λ flight cut(r) 3-D	2.4%	3.4%
x_p cut	2.2%	1.8%
Ξ^-Mass window	1.2%	2.6%
$\overline{K^0}$Mass window	1.0%	1.9%
vertexing	5.0%	5.0%
$\mathcal{B}(\Xi^-\to\Lambda\pi^+)$	3.5%	-
$\mathcal{B}(K^0_S\to\pi^+\pi^-)$	-	1.0%
Fitting	1.4%	4.1%
ϵ_{Ratio}	0.274	0.168
ϵ_{Ratio} (PID Corrected)	0.250	0.152
Tracking	2.8%	2.8%
Total Systematic error	8.0%	9.0%

Table 5.15: Summary table and source major of systematic uncertainties for the decay mode $\Lambda_c^+\to\Sigma^0\ K^+\pi^+\pi^-$.

Sources of Syste. error	$\frac{\mathcal{B}(\Lambda_c^+\to\Sigma^0 K^+\pi^+\pi^-)}{\mathcal{B}(\Lambda_c^+\to\Sigma^0\pi^+)}$
Monte Carlo Statistics	2.4%
MC Modeling	5.4%
ϵ_{Ratio}	0.42
ϵ_{Ratio} (PID Corrected)	0.39
Tracking	2.8%
Total Systematic error	6.5%

5.8 Results and Conclusions

5.8.1 The Decay mode $\Lambda_c^+ \to \Lambda K^+$

In order to determine out the relative B.F. for this decay mode we use $\Lambda_c^+ \to \Lambda\pi^+$ as a normalization mode. We obtain a fitted yield for $\Lambda_c^+ \to \Lambda K^+$ to be: 1162 ± 100.6 (stat.), whereas for the normalization mode we get yield: 33543 ± 334 (stat.), both at $x_p > 0.5$. The relative efficiency ratio is:

$$\frac{\epsilon(\Lambda_c^+ \to \Lambda K^+)}{\epsilon(\Lambda_c^+ \to \Lambda\pi^+)} = 0.781 \pm 0.010 \text{ (stat.)}.$$

using this value we extract:

$$\frac{\mathcal{B}(\Lambda_c^+ \to \Lambda K^+)}{\mathcal{B}(\Lambda_c^+ \to \Lambda\pi^+)} = \ 0.044 \ \pm \ 0.004 \text{ (stat.) } \pm \ 0.003 \text{ (syst.) }.$$

whereas the BELLE found [33] a value of 0.074 ± 0.010 (stat.) ± 0.012 (syst.) for this ratio.

5.8.2 Branching fraction $\Lambda_c^+ \to \Sigma^0\pi^+$relative to $\Lambda_c^+ \to \Lambda\pi^+$

The fit for the $\Lambda_c^+ \to \Lambda\pi^+$ decay mode suggests another way to measure the relative B.F., for the decay mode $\Lambda_c^+ \to \Sigma^0\pi^+$ relative to that of $\Lambda_c^+ \to \Lambda\pi^+$ (both are Cabibbo-favored decay modes), Figure 5.23. The fit yields: 33543 ± 334 (stat.) and 32693.0 ± 324 (stat.) Λ_c^+ decayed to $\Lambda\pi^+$ and to $\Sigma^0\pi^+$, respectively at $x_p > 0.5$. We calculate the relative efficiency ratio to be:

$$\frac{\epsilon(\Lambda_c^+ \to \Sigma^0\pi^+)}{\epsilon(\Lambda_c^+ \to \Lambda\pi^+)} = 1.013 \pm 0.010 \text{ (stat.)}$$

Using this value we extract the relative B.F. from the fit to be:

$$\frac{\mathcal{B}(\Lambda_c^+ \to \Sigma^0\pi^+)}{\mathcal{B}(\Lambda_c^+ \to \Lambda\pi^+)} = \ 0.977 \ \pm \ 0.015 \text{ (stat.) } \pm \ 0.051 \text{ (syst.) }.$$

This value is found to be consistent, if measured from the two, reconstructed separately.

$$\frac{\mathcal{B}(\Lambda_c^+ \to \Sigma^0 \pi^+)}{\mathcal{B}(\Lambda_c^+ \to \Lambda \pi^+)} = 0.980 \pm 0.018 \text{ (stat.) }.$$

5.8.3 The Decay mode $\Lambda_c^+ \to \Lambda K^+ \pi^+ \pi^-$

The decay mode $\Lambda_c^+ \to \Lambda K^+ \pi^+ \pi^-$ is a first time search. For this decay mode the fit gives a yield: 201.0 ± 64.0 (stat.) at $x_p > 0.6$. In order to find out the relative B.F. for this decay mode we use $\Lambda_c^+ \to \Lambda \pi^+$ as normalization mode, which yields: 22204.4 ± 256.7 (stat.) at $x_p > 0.6$.

We find the relative efficiency ratio to be:

$$\frac{\epsilon(\Lambda_c^+ \to \Lambda K^+ \pi^+ \pi^-)}{\epsilon(\Lambda_c^+ \to \Lambda \pi^+)} = 0.310 \pm 0.010 \text{ (stat.)}$$

using this value we extract:

$$\frac{\mathcal{B}(\Lambda_c^+ \to \Lambda K^+ \pi^+ \pi^-)}{\mathcal{B}(\Lambda_c^+ \to \Lambda \pi^+)} = 0.029 \pm 0.009 \text{ (stat.) } \pm 0.003 \text{ (syst.)}$$

Since our signal for Λ_c^+ decaying to $\Lambda K^+ \pi^+ \pi^-$ has a strength of 3.1σ, which is marginal, so we also set an upper limit at 90% C.L. for this measurement using Feldmans and Cousins method [41].

$$\frac{\mathcal{B}(\Lambda_c^+ \to \Lambda K^+ \pi^+ \pi^-)}{\mathcal{B}(\Lambda_c^+ \to \Lambda \pi^+)} < 4.8 \times 10^{-2} @ 90\% \text{ CL}$$

5.8.4 The Decay mode $\Lambda_c^+ \to \Xi^- K^+ \pi^+$

Since we see a very nice peak for this Cabibbo-favored decay mode having a major contribution to our Cabibbo-suppressed decay $\Lambda_c^+ \to \Lambda K^+ \pi^+ \pi^-$. So We also measure the B.F. for this Cabibbo-favored modes relative to $\Lambda_c^+ \to \Lambda \pi^+$.

We get a yield for the $\Lambda_c^+ \to \Xi^- K^+ \pi^+$ to be 2665 ± 84 (stat.), where as for the normalization mode we get a yield: 22204.4 ± 258.7 (stat.) at $x_p > 0.6$. We find the relative efficiency ratio to be:

$$\frac{\epsilon(\Lambda_c^+ \to \Xi^- K^+ \pi^+)}{\epsilon(\Lambda_c^+ \to \Lambda \pi^+)} = 0.250 \pm 0.003 \text{ (stat.)}$$

Using this value we extract the relative B.F. from the fit to be:

$$\frac{\epsilon(\Lambda_c^+ \to \Xi^- K^+ \pi^+)}{\epsilon(\Lambda_c^+ \to \Lambda \pi^+)} = 0.481 \pm 0.016 \text{ (stat.)} \pm 0.038 \text{ (syst.)}$$

This measurement clearly shows an improvement the error from the previous measurement [35] of $(0.544 \pm 0.253)\%$

5.8.5 The Decay mode $\Lambda_c^+ \to \Lambda \overline{K^0} K^+$

We also measure relative B.F. for this Cabibo-favored decay mode relative to that of $\Lambda_c^+ \to \Lambda \pi^+$. This decay mode also has contribution to our Cabibbo-suppressed mode for $\Lambda_c^+ \to \Lambda K^+ \pi^+ \pi^-$.

We get a yield: 460 ± 30 (stat.) for $\Lambda_c^+ \to \Lambda \overline{K^0} K^+$, where as for our normalization mode, we get a yield: 22204.4 ± 258.7 (stat.) at $x_p > 0.6$. Here we also take into account for the $K_S^0 \to \pi^+ \pi^-$ branching ratio [PDG value: $(68.6 \pm 0.27)\%$] in our calculations for this B.F. The relative efficiency is:

$$\frac{\epsilon(\Lambda_c^+ \to \Lambda \overline{K^0} K^+)}{\epsilon(\Lambda_c^+ \to \Lambda \pi^+)} = 0.152 \pm 0.020 \text{(stat.)}$$

Using this value we extract the relative B.F. from the fit to be:

$$\frac{\mathcal{B}(\Lambda_c^+ \to \Lambda \overline{K^0} K^+)}{\mathcal{B}(\Lambda_c^+ \to \Lambda \pi^+)} = 0.397 \pm 0.026 \text{ (} stat. \text{)} \pm 0.036 \text{ (} syst. \text{)}$$

This measurement shows an improvement the error from the previous measurement [35] of $(0.666 \pm 0.313)\%$

5.8.6 The Decay mode $\Lambda_c^+ \to \Sigma^0\ K^+$

In order to find out the relative B.F. for this decay mode we use $\Lambda_c^+ \to \Sigma^0\ \pi^+$as our normalization mode. The fitted yield for the $\Lambda_c^+ \to \Sigma^0\ K^+$ found to be: 375.6 ± 44.5 (stat.), where as for the normalization mode we get yield: 12490 ± 162 (stat.), both at $x_p > 0.5$. We find the relative efficiency ratio to be:

$$\frac{\epsilon(\Lambda_c^+ \to\ \Sigma^0 K^+)}{\epsilon(\Lambda_c^+ \to \Sigma^0 \pi^+)} = 0.780 \pm 0.010 \text{ (stat.)}.$$

using this value we extract:

$$\frac{\mathcal{B}(\Lambda_c^+ \to \Sigma^0 K^+)}{\mathcal{B}(\Lambda_c^+ \to \Sigma^0 \pi^+)} = \ 0.038\ \pm\ 0.005 \text{ (stat.) } \pm\ 0.003 \text{ (syst.) }.$$

where as BELLE found in 2001 [33] to be 0.056 ± 0.014 ($stat.$) $\pm\, 0.008$ (syst.) for this ratio at $x_p > 0.6$.

Our result is in agreement with the theoretical prediction [36] for this measurement, which is in the range [0.033-0.036].

5.8.7 The Decay mode $\Lambda_c^+ \to \Sigma^0\ K^+\pi^+\pi^-$

The decay mode $\Lambda_c^+ \to \Sigma^0\ K^+\pi^+\pi^-$ is a first time search. For this decay mode we did not see any statistically significant signal in the Λ_c mass region even at $x_p > 0.6$, Fit gives the yield: 20.7 ± 23.7 (stat.). So we set the 90% CL, based on Feldmans and Cousins method [41]. The normalization mode yields: 8848 ± 125.6 (stat.) at $x_p > 0.6$.

$$\frac{\mathcal{B}(\Lambda_c^+ \to \Sigma^0 K^+\pi^+\pi^-)}{\mathcal{B}(\Lambda_c^+ \to \Sigma^0 \pi^+)} < 2.0 \times\ 10^{-2} @\ 90\%\ \text{CL}$$

We find the relative efficiency ratio with the normalization mode($\Lambda_c^+ \to \Sigma^0\ \pi^+$) to be:

$$\frac{\epsilon(\Lambda_c^+ \to \Sigma^0 K^+ \pi^+ \pi^-)}{\epsilon(\Lambda_c^+ \to \Sigma^0 \pi^+)} = 0.390 \pm 0.010(\text{stat}).$$

5.9 SUMMARY

We report on a measurement of the branching ratio of the Cabibbo-suppressed decays $\Lambda_c^+ \to \Lambda^0 K^+$ and $\Lambda_c^+ \to \Sigma^0 K^+$ with improved accuracy and we also measure the relative branching fraction for the $\Lambda_c^+ \to \Sigma^0 \pi^+$ relative to $\Lambda_c^+ \to \Lambda^0 \pi^+$. We set an upper limit for the Cabibbo-suppressed decay $\Lambda_c^+ \to \Lambda^0 K^+ \pi^+ \pi^-$ and also set an upper limit on $\Lambda_c^+ \to \Sigma^0 K^+ \pi^+ \pi^-$ decay. The results for these decay modes are summarized in table **??**. We also measure the relative branching fraction for the Cabibbo-favored decays $\Lambda_c^+ \to \Xi^- K^+ \pi^+$ relative to that of $\Lambda_c^+ \to \Lambda^0 \pi^+$, and $\Lambda_c^+ \to \Lambda^0 \overline{K^0} K^+$ relative to that of $\Lambda_c^+ \to \Lambda^0 \pi^+$, respectively.

The expectations from Quark model [36] are $\mathcal{B}(\Lambda_c^+ \to \Lambda K^+)/\mathcal{B}(\Lambda_c^+ \to \Lambda \pi^+)$ = [0.039-0.056] and $\mathcal{B}(\Lambda_c^+ \to \Sigma^0 K^+)/\mathcal{B}(\Lambda_c^+ \to \Sigma^0 \pi^+)$ = [0.033-0.036]. The results are in agreement with these predictions.

References

[1] S. Okubo, Phys. Lett. **5**, 165 (1963); G. Zweig, CERN Reps. TH-401, 412 (1964); J. Iizuka, Suppl. Prog. Theor. Phys. **37-38**, 21 (1966).

[2] N. Cabibbo, Phys. Rev. Lett. **10**, 531 (1963); M. Kobayashi and K. Maskawa, Prog. Theor. Phys. **49**, 652 (1973).

[3] J. J. Aubert *et al.*, Phys. Rev. Lett. **33**, 1404 (1974).

[4] J. E. Augustin *et al.*, Rev. Lett. **33**, 1406 (1974).

[5] E. G. Cazzoli *et al.*, Phys. Rev. Lett. 34, 1125 (1975).

[6] S. W. Herb *et al.*, Phys. Rev. Lett. 39, 252 (1977).

[7] J. G. Körner, H. W. Siebert, "Heavy Baryons: Theory and Experiment", Annu. Rev. Nucl. Part. Sci., 41 511 (1991);

[8] Review of Particle Physics, The European Physical Journal C, Vol 15, (2000).

[9] W. Greiner and B. Müller, "Quantum Mechanics Symmetries", Springer-Verlag.

[10] Rob Kütschke, "Heavy Flavor Spectroscopy", and the citations therein.

[11] CLEO Collaboration (M. Artuso et al.). CLNS-00-1698, CLEO-00-22, Oct 2000. 11pp. hep-ex/0010080.

[12] CLEO Collaboration (S. E. Csorna et al.). CLNS-00-1702, CLEO-00-25, Oct 2000. 10pp. hep-ex/0012020.

[13] CLEO collaboration (R. Ammar *et al.*.). **hep-ex**/0007041.

[14] C. P. Jessop *et al.*, Phys. Rev. Lett. 82, 281 (1991).

[15] F. Hussain *et al.*, Phys. Lett. B**249** 295 (1990); N. Isgur, M. B. Wise, Phys. Lett. B**237** 527 (1990); E. Eichten, B. Hill; Phys. Lett. B**234** 511 (1990).

[16] J. H Christenson, J. W. Cronin, V. L. Fitch and R. Turlay, Phys. Rev. Lett. **13** 138 (1964).

[17] A. B. Carter and A. I. Sanda, Phys. Rev. D **23** 1567 (1981).

[18] K. Abe *et al.*, "Observation of Large CP Violation in the Neutral B Meson System", Phys. Rev. Lett. **87**, 091802 (2001).

[19] CDF Collaboration, F. Abe *et al.*, Phys. Rev. Lett. **79**, 572 (1997);
CDF Collaboration, F. Abe it et al. , Phys. Rev. Lett. **79**, 578 (1997).

[20] R. Baier and R. Ruckl, Z. Phys. C. **19**, 251 (1983); W.W.N. Glover, A.D. Martin and W.J. Stirling, Z. Phys. C **38**, 473 (1988).

[21] E. Braaten and S. Fleming, Phys. Rev. Lett. **74**, 3327 (1995)
P. Cho and M. Wise, Phys. Lett. B. **346**, 129 (1995);
M. Cacciari, M. Greco, M. L. Mangano and A. Petrelli, Phys. Lett. B **356**, 553 (1995);
P. Cho and A.K. Leibovich, Phys. Rev. D. **53**, 150 (1996); P. Cho and A.K. Leibovich, Phys. Rev. D. **53**, 6203 (1996).

[22] S. Baek, P. Ko, J. Lee, and H.S. Song, J. Kor. Phys. Soc. **33**, 97 (1998); hep-ph/9804455..

[23] M. Krämer, hep-ph/0106120, 12 Jun 2001 Prog.Part.Nucl.Phys. **47**, (2001) 141-201).

[24] Caswell WE, Lepage GP. Phys. Lett. B **167**:437 (1986).

[25] P. F. Harrison and K. R. Quin [*BABAR* Collaboration], The *BABAR* Physics Book at the asymmetric B factory.

[26] B. Aubert *et al.*, Nucl. Instrum. Methods A **479**, 1 (2002).

[27] "http://www.slac.stanford.edu/BFROOT/www/Physics/Tools/PepBeam".

[28] Geant4 Collaboration, "Geant4 - A Simulation ToolKit" , Nucl. Instrum. Methods A **506**, (2003).

[29] D. H. Perkins, *Introduction to High Energy Physics*, Addison-Wesley (1987).

[30] P. Billior, "Track fitting with Multiple Scattering; A New Method" Nucl. Instrum. Methods A **225**, 352 (1984).

[31] S. Sewerynek, "A Monte Carlo Study of the Momentum dependence on the Results of Tracking Unknown Particle Species in the *BABAR* Detector." M.Sc. Thesis UBC, 1999.

[32] C. Roat, "Identification of Hadrons for Λ_c Reconstruction in *BABAR*." BAD402 (*BABAR* Internal Document).

[33] BELLE Collaboration, K. Abe. *et al.*, Phys. Lett. B **524**, 33 (2002).

[34] FNAL Focus Collaboration, J. M. Link. *et al.* , 8, Phys. Rev. Lett. **8**, 1 (6)1801 2002

[35] S. Eidelman *et al.* Phys. Lett. B **592**, 1 (2004).

[36] T. Utpal, R. C. Verma and M. P. Khana, 4, Phys. Rev. D **9**, 3 (4)17 (1994) .

[37] J. G. Körner and M. Krämer, Z. Phys. **C55**, 659 (1992).

[38] J. G. Körner, M. Krämer and J. Willrodt, Z. Phys. **C2**, 117(1979).

[39] URL=http://www.slac.stanford.edu/ tbrandt/pid/tables/pidtable/

[40] URL=http://www.slac.stanford.edu/BFROOT/www/Physics/TrackEfficTaskForce /TrackingTaskForce-2004.html#Recipes.

[41] G. J. Feldman and R. D. Cousins, 5, Phys. Rev. D **7**, 3 (8)73 1998